Biomass-derived Hard Carbons as anode materials for Li-ion and Na-ion batteries

Luca Bottoni

Dissertação para obtenção do Grau de
Mestre em

Química

Luca Bottoni

Orientadores: Prof. João Carlos Salvador Santos Fernandes
Prof. Francesco Nobili

Jùri

Presidente: Profª. Isabel Maria Delgado Jana Marrucho Ferreira

Orientadores: Prof. João Carlos Salvador Santos Fernandes

Vogais: Profª. Alda Maria Pereira Simões

Juhno de 2019

“Insanity is doing the same thing over and over again and expecting different results”

Albert Einstein

ABSTRACT

Electrochemical energy storage devices, such as batteries, have been proven to be the most effective energy conversion and storage technologies for practical application. Among them, Li-ion batteries play a key role for portable devices and electrified vehicles, while a possible substitution is represented by the Na-ion batteries, with advantages in terms of resources availability and a drawback in terms of performances. Both kind of batteries commonly rely on carbonaceous anodes. Carbon-based materials used in batteries are usually derived from non-renewable sources as the fossil ones. Therefore, biomass is a natural green alternative carbon source with many desired properties, including the fundamental goal of the global energy sustainability. In my thesis I report the results of a research work focused on the synthesis and characterization of biomass-derived Hard Carbons as anode materials for Li-ion and Na-ion batteries. The biomasses used as raw materials have been cherry stones, orange peel, olive leaves and olive pits. They have been chosen since they are common agricultural by-products in Italy. The first part of the work has been focused on the synthesis of Hard Carbons (HCs), driven in order to compare different types of synthesis, which basically differ in the activation process applied before the pyrolysis of the raw material at high temperatures (around 900 °C). Three different procedures of activation have been developed for orange peels and olive pits (no activation, acid and alkali activation), one for olive leaves (acid activation) and one for cherry stones ($ZnCl_2$ activation), respectively. The second part regards the structural and morphological characterization of the synthesized Hard Carbons. First of all, Thermogravimetric Analysis has been used to examine the physicochemical processes occurring in the HC's precursors, in order to understand the kinetics of the decomposition process of the samples, and exploit it to tailor the annealing of the sample precursors. Then, Raman Spectroscopy and X-Ray Diffraction have been used to examine and compare the structural characteristics of the HCs, since they produce typical spectral features and peaks. Finally, Scanning Electron Microscopy analysis has been performed in order to try to correlate the electrochemical behaviour with the different morphologies of the HCs. In the third part, the electrochemical performances of the HCs have been tested. All of the HCs have been tested in Li-ion and Na-ion batteries, in different experimental conditions. Particular attention has been devoted to the choice of suitable binders (Na-CMC and PVdF) and to the definition of the optimal working potential range. Cyclic Voltammetry and Galvanostatic Cycling with Potential Limitation have been performed to evaluate and compare the electrochemical features of the HCs. Among them, olive stones, orange peel and olive leaves acid-activated hard carbons appear the most promising anode materials due to their relatively high specific capacity (at currents of the order of 300 mA/g) and electrochemical stability (in the range $0.02 < Ewe < 3.00$) both in Li-ion and Na-ion batteries. This probably reflects the ability of the acid to promote the hydrolysis of the carbon sources, such as lignocellulose, cellulose and sugars, which aids in obtaining optimal structure and morphology of the active materials.

Key words: Lithium-Ion Batteries, Sodium-Ion Batteries, Anodes, Hard Carbon, Biomass

RESUMO

Os dispositivos de armazenamento de energia eletroquímica, como as baterias, provaram ser as tecnologias mais eficientes de conversão e armazenamento de energia para aplicação prática. No entanto, o baixo desempenho do eletrodo limita o desenvolvimento desses dispositivos de armazenamento de energia. Os materiais de carbono usados em baterias geralmente são derivados de fontes não renováveis. Portanto, as biomassas são uma fonte de carbono alternativa verde natural com muitas propriedades desejáveis, incluindo o objetivo fundamental da sustentabilidade energética global. Nesta tese é relatado um trabalho focado na síntese e caracterização de Carbonos Rígidos derivados da Biomassa como materiais anódicos para baterias de íons de Lítio e Na-íon. As biomassas utilizadas como matéria-prima são as pedras de cereja, casca de laranja, folhas de oliveira e azeitonas. Eles foram escolhidos porque são subprodutos agrícolas comuns da Itália. A primeira parte do trabalho foi focada na síntese de Hard Carbons (HCs), que tem sido direcionada para fazer uma comparação entre diferentes tipos de syntheys, que diferem basicamente no processo de ativação antes da carbonização da matéria-prima temperaturas em torno de 900 e 1000 ° C. Três diferentes procedimentos de ativação foram desenvolvidos para cascas de laranja e olivas (sem ativação, ativação ácida e alcalina), uma para folhas de oliveira (ativação ácida) e uma para cálculos de cereja (ativação de ZnCl2), respectivamente. A segunda parte diz respeito à caracterização morfológica dos Hard Carbons sintetizados. Primeiramente, a Análise Termogravimétrica tem sido utilizada para examinar os processos físico-químicos ocorridos nos precursores do HC, a fim de compreender a cinética do processo de decomposição das amostras e explorá-lo para estabelecer os parâmetros experimentais mais apropriados para o recozimento dos precursores da amostra. . Em seguida, Espectroscopia Raman e Difração de Raios-X têm sido utilizados para examinar e comparar as características estruturais dos HCs, uma vez que os HCs produzem espectros que podem ser considerados como uma “impressão digital”. Finalmente, a análise por Microscopia Eletrônica de Varredura foi realizada somente nos materiais mais promissores, a fim de compreender se os melhores resultados podem ser correlacionados com uma morfologia particular dos HCs. Na terceira parte, os desempenhos eletroquímicos dos HCs foram testados. Todos os HCs foram testados em baterias de Li-ion e Na-ion, em diferentes condições experimentais: ligantes (Na-CMC e PVdF) e faixa de potencial de trabalho. Voltametria Cíclica e Ciclagem Galvanostática com Limitação Potencial foram realizadas para avaliar e comparar as características eletroquímicas dos HCs. Dentre eles, os carvões duros ativados por casca de laranja e ácido de folhas de oliveira são os materiais anódicos mais promissores devido à sua boa capacidade específica (cerca de 150 mAh / ge 200 mAh / g em baterias Li-ion, respectivamente e cerca de 80 mAh / g para ambos os materiais em baterias de íons de Na) e estabilidade eletroquímica (entre 0,02-Ewe-3,00) tanto em baterias de íons de lítio quanto de íon Na. Isso provavelmente reflete a capacidade do ácido de promover a hidrólise das fontes de carbono, como a lignocelulose, a celulose e os açúcares.

Palavras-chave: Baterias de íons de litio, Baterias de íons de sodio**,** ânodos**,** Carbonos Rigidos**,** Biomassa

TABLE OF CONTENTS

INDEX OF FIGURES

INDEX OF SCHEMES

ABBREVIATION LIST

In this thesis has been used the following abbreviation:

- **GHG:** Global Greenhouse Gases;
- **BRIICS:** Brazil, Russia, India, Indonesia, China and South Africa;
- **IEO2016:** International Energy Outlook 2016;
- **LIB:** Li-Ion Battery;
- **NIB:** Na-Ion Battery;
- **HC:** Hard Carbon;
- **SEI:** Solid Electrolyte Interphase;
- **E_{pa}:** Anodic peak potential;
- **E_{pc}:** Cathodic peak potential;
- **I_{pa}:** Anodic peak intensity;
- **I_{pc}:** Cathodic peak intensity;
- **Sample names abbreviations:**
    - **HCL4:** Acid activated olive leaves derived Hard Carbon;
    - **HCC:** $ZnCl_2$ activated cherry stones derived Hard Carbon;
    - **HCO1:** No activated orange peels derived Hard Carbon;
    - **HCO2:** Alkali activated orange peels derived Hard Carbon;
    - **HCO3:** Acid activated orange peels derived Hard Carbon;
    - **HCJ1:** No activated olive stones derived Hard Carbon;
    - **HCJ2:** Alkali activated olive stones derived Hard Carbon;
    - **HCJ3:** Acid activated olive stones derived Hard Carbon;

1.INTRODUCTION

1.1 Overview

Climate change is a serious global systemic risk to society. Global greenhouse gas (GHG) emissions continue to increase, and this could result in a wide range of adverse impacts and potentially large-scale, irreversible and catastrophic changes that will exceed the adaptive capacity of natural and social systems.

Even if the Kyoto Protocol intends to limit emissions of the main gases responsible for the bulk of global warming, the *OECD Environmental Outlook Baseline* scenario ***(Figure 1a-b)*** suggests that GHG emissions will continue to grow to 2050, reaching an historic high of around 80 gigatons carbon dioxide equivalent ($GtCO_2e$). Carbon dioxide (CO_2) emissions are projected to remain the largest contributor to global GHG emissions, while the total emissions of methane (CH_4), nitrous oxide (N_20), hydrofluorocarbons (HFCs), perfluorocarbons (PFCs) and sulphur hexafluoride (SF_6) are growing as well. These gases differ in terms of their warming effect and their longevity in the atmosphere. In terms of emissions by regions, BRIICS (Brazil, Russia, India, Indonesia, China and South Africa) countries are projected to account for most of the increase, driven by both economic and population growths. Instead the OECD (Organisation for Economic Co-operation and Development) countries emissions are projected to grow at a slower pace, partly reflecting demographic decline and slower economic growth, as well as existing climate policies [1].

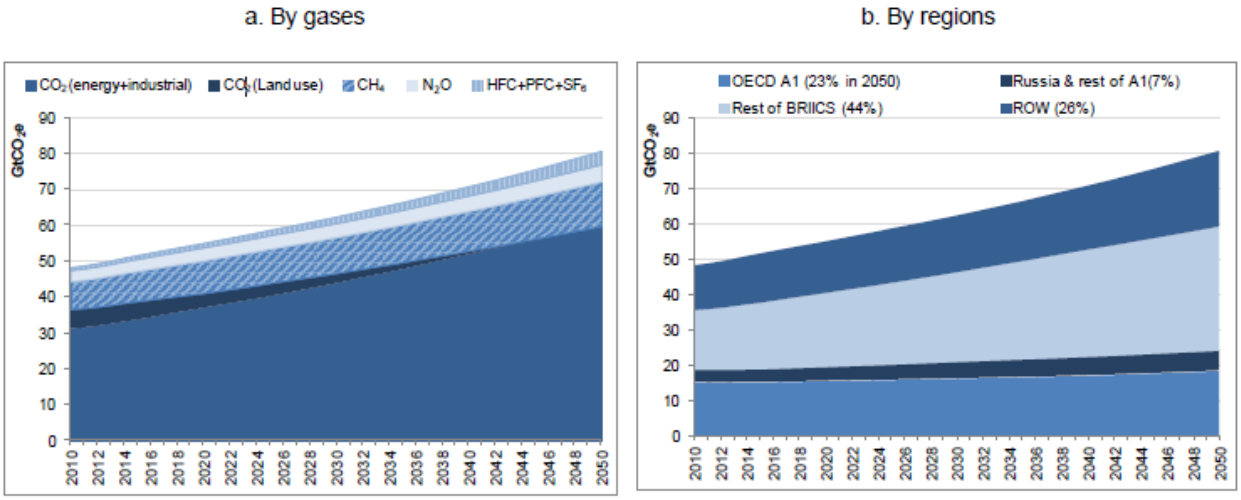

Figure 1: (a) GHG emissions projection by gases (left); (b) GHG emissions projection by regions (right);

Carbon dioxide CO_2 emissions account for around 75% of global GHG emissions and most of them come from energy production (***Figure 2a***), primarily by fossil fuel combustion. Thus, energy is one of the most important topics in modern society due also to the ever-increasing energy demand. Unfortunately, the current power supplies are mainly based on limited and non-renewable fossil fuels (oil, coal, natural gas) [2]. Therefore, the goal of global energy sustainability implies the replacement of all fossil fuels by nonfossil-based, reliable, affordable and limitless energy sources. However, as shown in ***Figure 2b***, fossil fuels continue to provide most of the world's energy in the IEO2016

(International Energy Outlook) projection: in 2040, liquid fuels, natural gas and coal account for 78% of total energy consumption; nevertheless, the highest growth of renewable energy sources is encouraging, also thanks to the greener government policies.

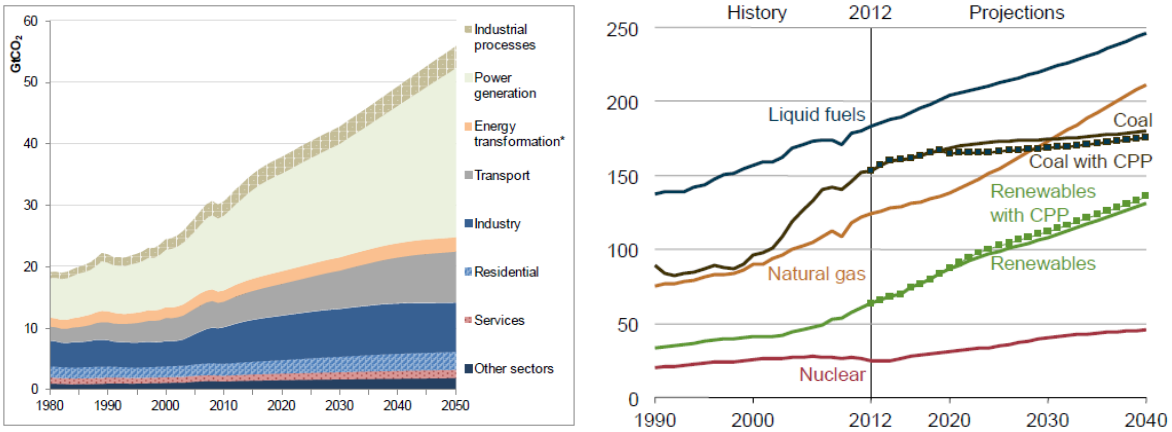

Figure 2: (a) Global CO_2 emissions projection divided by sectors (left); (b) Total world energy consumption by source, 1990-2040 (right);

Under the Outlook Baseline scenario, the global concentration of GHGs is expected to reach approximately 685 ppm CO_2 equivalent (CO_2e) by mid-century and more than 1000 ppm CO_2e by 2100, values well above the threshold fixed in the Kyoto Protocol (450 ppm), the level associated with a 50% chance of exceeding of the 2°C global average temperature change goal. As a result (***Figure 3***), global mean temperature is expected to increase at the middle of century of 2.0°C-2.8°C, and 3.7°C-5.6°C at the end of the century (compared to the pre-industrial times) [1]. Given the expected increase in temperature, the key and catastrophic impacts are summarized in ***Figure 4***:

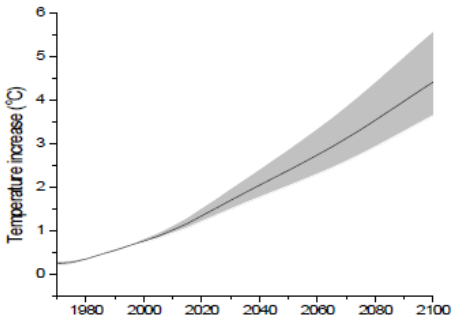

Figure 3: Temperature increase 1980-2100. The grey area represents the uncertainty of the calculations;

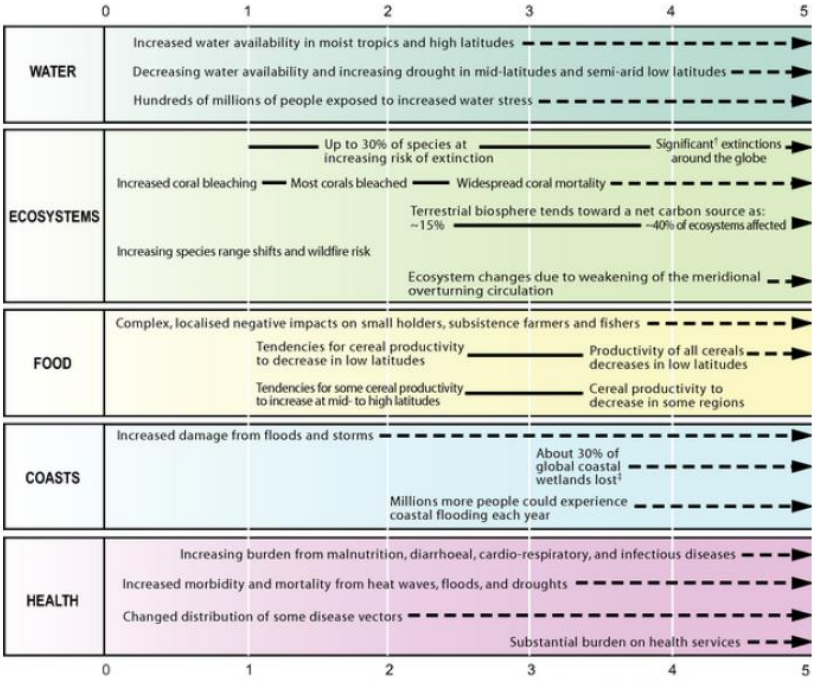

Figure 4: Key impacts of increasing global temperature;

Thus, the present and future production and use of energy pose a serious threat to the global environment in relation to emissions of greenhouse gases (principally, carbon dioxide, CO_2) and consequent climate change.

We must act now to reverse emission trends in order to stabilize GHG concentrations at 450 ppm CO_2e and increase the chance of limiting the global average temperature increase to 2°C.

We must do it now to lower the risk of catastrophic climate change that it will have rough impact on humans and ecosystems.

1.2 Electricity generation and storage

Energy conversion and storage plays the key role in achieving global energy sustainability. To date, numerous energy conversion and storage technologies, such as solar cell, flywheel, compressed air, fuel cell, supercapacitor and battery have been developed with the goal of utilizing sustainable energy sources, such as solar, wind, geothermal, tidal or biomass energy [2].

Electricity is the world's fastest-growing form of end-use energy consumption thanks to its versatility for many applications: the world net electricity generation increases 69% by 2040, from 21.6 trillion kilowatthours (kWh) in 2012 to 36.5 kWh in 2040 [3]. The worldwide mix of primary fuels used to generate electricity has changed a great deal over the past several decades. Coal continues to be the fuel most widely used in electricity generation [4], but there have been significant shifts to other generation fuels, such as nuclear power, natural gas and renewable energy sources. In particular, renewables are the fastest-growing source of energy for electricity generation, with annual increases averaging 2.9% from 2012 to 2040 (***Figure 5a***) [3]. Among the renewable sources (***Figure 5b***), generation from non-hydropower renewables is the predominant source of the increase, with the solar

undergoing the world's fastest-growing form of renewable energy. However, hydropower still remains the most important source.

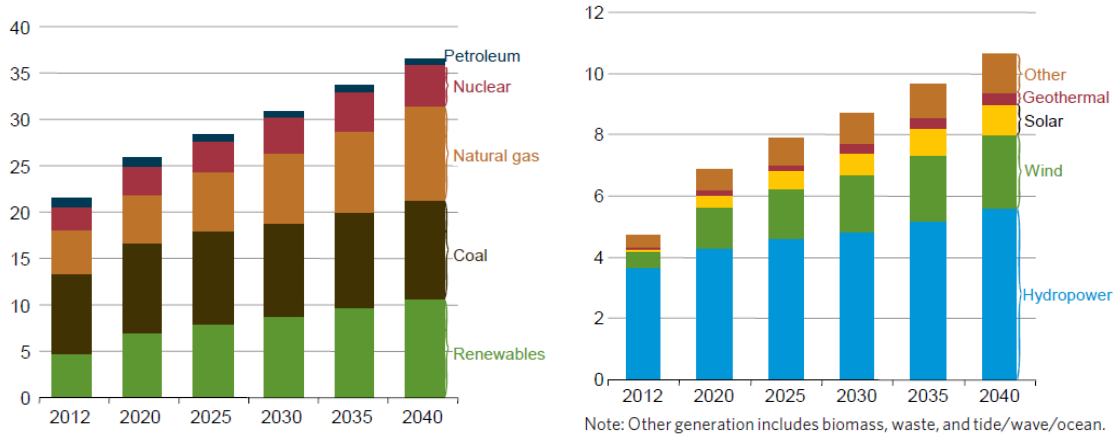

Figure 5: (a) World net electricity generation by energy source (right) and (b) from renewable power by fuel (left), 2012-40 (trillions kWh);

Due to the ever-increasing demand of electricity, in addition to the overcoming of non-renewable energy sources, the development and application of systems for the efficient storage of electricity are fundamental. Electricity cannot be stored directly, except in very small amounts in various types of capacitor or in electromagnetic coils – both of these technologies are costly, and the latter is still at the development stage. Rather, the electricity has first to be converted to an alternative energy form for the storage. There are four possibilities:

I) potential energy (pumped-hydro, compressed-air);
II) kinetic energy (flywheels);
III) thermal energy (hot water, fused salts);
IV) chemical energy (batteries, fuel cells);

Among them, realistic options to store electricity generated by renewable forms of energy are pumped-hydro, flywheels and batteries. In particular, pumped-hydro is the way to store large quantities of electricity; instead, batteries are the best option available for storing small-medium quantities of electricity [5].

2.BATTERIES

Batteries has been proven to be the most effective electrochemical energy conversion and storage devices for practical application [2]. Battery is a device that converts the chemical energy stored in its active materials into electric energy by an electrochemical oxidation-reduction reaction. The redox reaction involves the transfer of electrons from one material to another through an electric circuit and the restoring of charge neutrality through electrolyte migration. Each battery is composed by one or more cells, that are the basic electrochemical unit, connected in series or parallel, to achieve the desired working voltage and capacity.

The cell is composed of three main components:

- ***Anode*** *or negative electrode:* is the reducing electrode which delivers electrons to the external circuit and is oxidized during the electrochemical reaction. Ideally, the anode should be an efficient reducing agent, have high coulombic output (Ah/g), good stability and low cost;
- ***Cathode*** *or positive electrode*: is the oxidizing electrode that accepts electrons from the external circuit and is reduced during the electrochemical reaction. It should be an efficient oxidizing agent, stable, cheap and have a useful working voltage;
- ***Electrolyte***: is the ionic conductor that transfers the charge as ions between the anode and cathode. It must have high ionic conductivity but not be electronically conductive in order to avoid short-circuit. Moreover, a good electrolyte is not reactive toward the electrode materials, cheap and environmentally friendly;

The anode and cathode are electronically insulated and separated to prevent short-circuiting. The separator must be permeable to the electrolyte to provides the desired ionic conductivity.

The main parameters that describes the electrochemical features of a battery are:

- ***Capacity (Q)***: is the charge stored in a battery. It is expressed in Coulomb (C) or Ampere hour (Ah) and calculated as:

$$Q = I * t = x * n * F \qquad (eq.1)$$

  where I is the current, t is the time, x is the number of moles, n is the number of electrons that are involved in the reaction and F is the Faraday constant (96494 C/mol).

- ***Energy (E)***: is expressed in joule (J) or Watt hour (Wh) but often referred to the weight as specific energy (Wh/kg) or to the volume as energy density (Wh/l). It is calculated as:

$$E = Q * V \qquad (eq.2)$$

  where Q is the capacity and V is the voltage of the cell.

- ***Power (P)***: is expressed in Watt (W) but as well as energy, it is often expressed as specific power (W/Kg) or power density (W/l). It is calculated as:

$$P = I * V = (Q * V)/t = E/t \qquad (eq.3)$$

  Where I is the current, V the voltage, Q the charge and E the energy.

Batteries can be divided in two categories: primary batteries and secondary batteries. The main difference between them is related upon the rechargeability.

Primary batteries are single-use batteries because they cannot be recharged effectively. The general advantages of these batteries are high energy density at low to moderate discharge rates, good shelf

life and long storage times. These characteristics allow to exploit them in several common applications, such as watches, clocks, toys and also in special uses like medical devices, missiles and weapons systems. ***Table 1*** shows some example of common commercial primary battery systems:

Table 1: Main commercial primary batteries

Battery	Structure of battery	Reaction	Energy Density (Wh/kg)	Voltage (V)
Zn-C	$Zn_{(s)}/ZnCl_{2(aq)}$, $NH_4Cl_{(aq)}/MnO_2(s)$, $C_{(s)}$	$Zn+2MnO_2+2NH_4Cl \rightarrow Zn(NH_3)_2Cl_2+2MnOOH$	65	1.2
Zn-Cl	$Zn_{(s)}/ZnCl_{2(aq)}$, $/MnO_{2(s)}$, $C_{(s)}$	$Zn+2MnO_2 \rightarrow ZnO+Mn_2O_3$	75	1.2
Alkaline	$Zn_{(s)}/KOH_{(aq)}/MnO_{2(s)}$, $C_{(s)}$	$Zn+2MnO_2 \rightarrow ZnO+Mn_2O_3$	95	1.2
Li-$SOCl_2$	$Li/LiAlCl_4$ in $SOCl_2/C_{(s)}$	$4Li+2SOCl_2 \rightarrow 4LiCl+SO_2+S$	350-450	3.3
Li-MnO_2	$Li/LiClO_4$ in PC-DME/$MnO2_{(s)}$	$Li+MnO_2 \rightarrow LiMnO_2$	160-215	2.8

Secondary batteries can be recharged electrically by applying an opposite current flow to the electric circuit. They are characterized by high power density, high discharge rate, high efficiency and good low-temperature performances. The energy densities of secondary batteries are generally lower than those of primary batteries but they have the advantage of being more cost efficient over the long term and environmentally friendly [6]. Secondary batteries have a wide range of applications such as laptop, mobile phones, electric vehicles and power tools. In the market there are several types of secondary batteries and the most common are listed in ***Table 2***:

Table 2: Main commercial secondary batteries

Battery	Reaction	Energy Density (Wh/kg)	Voltage (V)	Cycle Life
Lead Acid	$Pb+PbO_2+2H_2SO_4 \rightarrow 2PbSO_4+2H_2O$	30-40	2.0	> 1000
Ni-Cd	$Cd+2NiOOH+2H_2O \rightarrow Cd(OH)_2+2Ni(OH)_2$	30-50	1.2	> 200
Li-ion	$LiM_aO_b+6C \rightarrow Li_{1-x}M_aO_b+Li_xC_6$	170 +/- 70	3.6-4	> 1200

In ***Figure 6***, the energy densities of various types of batteries are compared: Li/Na-air batteries show the best energy densities however they use lithium and sodium metal anode that tend to deposit in dendritic form, which is known to be the main safety issue. The Li/Na-sulphur batteries show lower

capacities compared to the previous ones, however in addition to the problem related to the use of metal anode, the major problem is the dissolution in the electrolyte of Li/Na polysulfide that results in a continuous loss of capacity during cycles. This means that Li/Na-ion batteries, with their energy density of ~ 170 Wh/kg and ~ 150 Wh/kg respectively (determined by the reaction cell itself, that is, the electrode materials being used) [7], combined with other advantages, currently are the most promising batteries for commercial use.

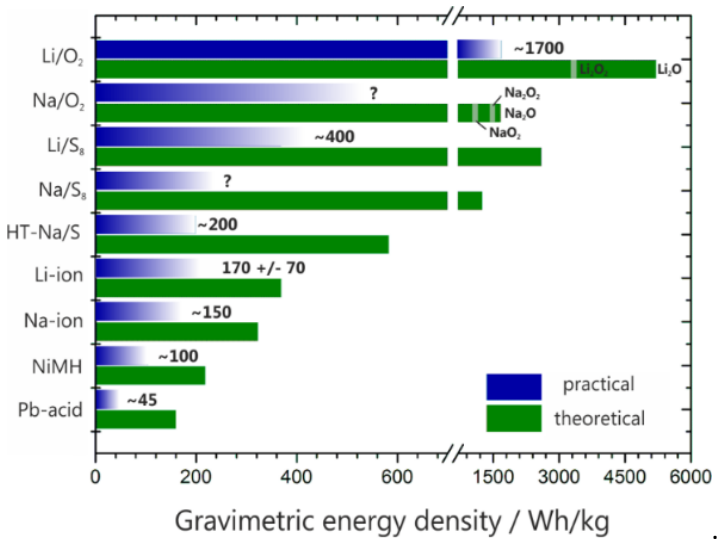

Figure 6: Comparison of theoretical and (estimated) practical energy densities of common batteries [7];

2.1 Li-ion Batteries

Lithium is the lighest of all metals, has the greatest electrochemical potential and provides the largest energy density per weight. For many years Nichel–Cadmium has been the most used battery. In fact, the first rechargeable lithium batteries had safety problems due to the instability of the lithium metal used as anode, that during charging, tended to react with the electrolyte forming dendritic deposition, known to be the main cause of thermal runaway and explosion hazards caused by internally shorting the cells [8]. Therefore, the research shifted to a non-metallic lithium battery using Li^+ ions. Although slightly lower in energy density than lithium metal (~ 170 Wh/kg respect to the ~ 440 Wh/Kg of lithium metal cell), Li-ion Batteries are safe. The main advantages can be summarized as follow:

- High energy density – potential for yet high capacities;
- Does not need prolonged priming when new: one regular charge is all that's needed;
- Relatively low self-discharge: it is less than half that of nickel-based batteries;
- Rapid charge capability;
- High rate and high-power discharge capability;
- High coulombic efficiency and energy efficiency;
- Low Maintenance: no periodic discharge is needed;
- Specialty cells can provide very high current to applications such as power tools;
- Long cycle life;

Instead, the main limitations are:

- Requires protection circuit to maintain voltage and current within safe limits;
- Subject to aging, even if not in use: storage in a cool place at 40% charge reduces the aging effect;
- Expensive to manufacture: about 40 percent higher in cost than nickel-cadmium because lithium is a very expensive material;
- Not fully mature: metals and chemicals are changing on a continuing basis;
- Capacity loss or thermal runaway when over-charged;
- Degrades at high temperatures;

The main feature of lithium-ion battery (LIB) is that the electrodes are made of materials that are able to react reversibly with lithium: this kind of materials are called ***intercalation materials*** because they are able to guest in their structure the lithium ions flowing through the electrolyte to balance the positive or negative charge created on the electrode during the redox reaction.
A schematic representation of the working mechanism of a Lithium-ion cell is shown in ***Figure 7***:

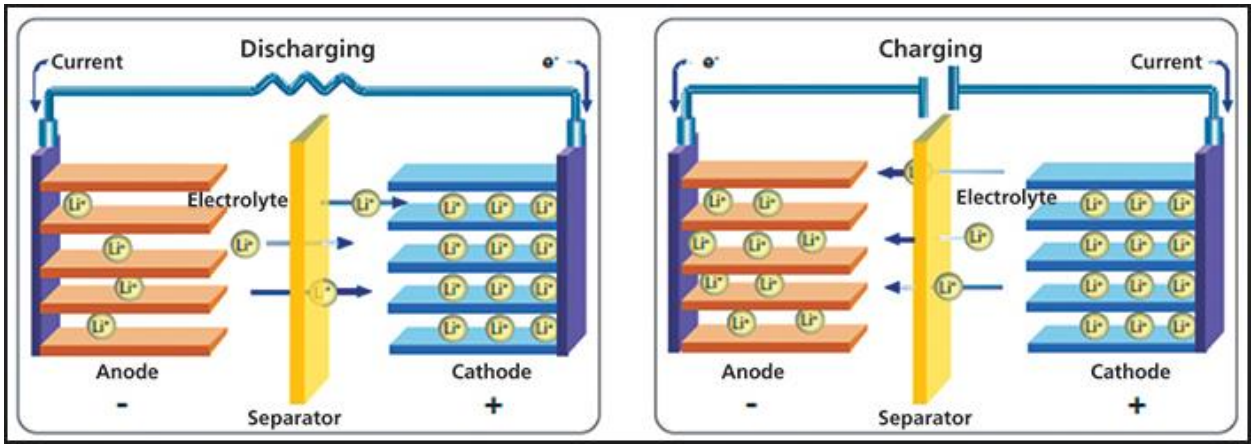

Figure 7: Mechanism of charge/discharge processes;

In details, during the discharge, the lithium atoms at the surface of the anode undergo an oxidation reaction, releasing positively charged Li^+ ions and negatively charged electrons. The Li^+ ions flow to the cathode through the electrolyte, allowing the reduction, instead the electrons flow to the positive electrode through the external circuit, resulting in an electric current that does useful work.

$$\text{Anode: } Li_xC \dashrightarrow xLi^+ + xe^- + C \quad \text{(oxidation)} \qquad \text{(Reaction 1)}$$

$$\text{Cathode: } Li_{(1-x)}MO_2 + xLi^+ + xe^- \dashrightarrow LiMO_2 \quad \text{(reduction)} \qquad \text{(Reaction 2)}$$

During charge, a current is forced to flow in the opposite direction by the external circuit, simultaneously electrons flow from cathode to anode through the external circuit and Li^+ ions are extracted from the cathode to go to be reduced at anode. The charge is exactly the reverse reaction of the previous one. The total reaction can be written as follows:

$$\text{Total reaction: } LiMO_2 + C \dashrightarrow Li_{(1-x)}MO2 + Li_xC \qquad \text{(Reaction 3)}$$

Generally, commercial batteries contain a graphite anode, a lithium metal oxide ($LiCoO_2$) as cathode and an electrolyte consisting of a solution of a lithium salt ($LiPF_6$) in a mixed organic solvent (ethylene carbonate-dimethyl carbonate, EC-DMC) embedded in a separator [9].

2.1.1 Cathode Materials

Cathode materials play an important role in the performances of Li-ion batteries because they affect the energy capacity, voltage, cycle life and safety. Good cathode materials must have the following features:

- Stable structure upon Li^+ ions intercalation/de-intercalation;
- High capacity to contain Li^+;
- High potential (vs Li/Li^+);
- High electronic conductivity;
- High Li^+ diffusion coefficient;
- Low cost and safety;

Currently, the three major structure of cathode materials are layered structure oxides, spinels and olivines (***Figure 8***):

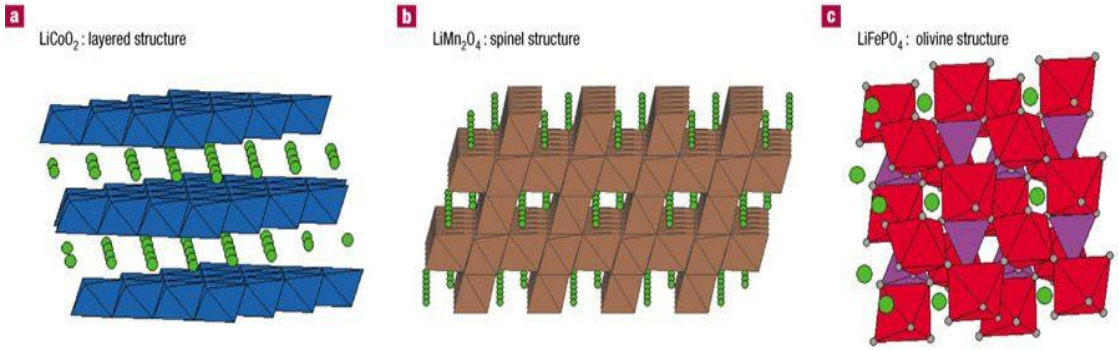

Figure 8: a) Layered; b) Spinel; c) Olivine structures;

The $LiCoO_2$ is the most used cathode material in commercial batteries due to its high energy density. However, its instability, high cost of raw material and toxicity pushed the use of alternative materials such as transition metal oxides (i.e. $LiMn_2O_4$) or lithium iron phosphate ($LiFePO_4$). ***Table 3*** shows a comparison of common cathode materials for Li-ion batteries.

Table 3: Comparison of various cathode materials

Cathode Material	Structure	Average Voltage	Gravimetric Capacity
$LiCoO_2$	Layer	3.7 V	140 mAh/g
$LiMn_2O_4$	Spinel	4.0 V	100 mAh/g
$LiNiO_2$	Layer	3.5 V	180 mAh/g
$LiFePO_4$	Olivine	3.3 V	150 mAh/g
$LiCo_{1/3}Ni_{1/3}Mn_{1/3}O_2$	Layer/Spinel	3.6 V	159 mAh/g

2.1.2 Electrolytes

Electrolyte provides the transport of the charge between the electrodes. Its properties affect stability, coulombic efficiency, rate capability and safety of battery. A good electrolyte must meet the following requirements:

- High ionic conductivity, in order to minimize the internal resistance of the cell;
- Good chemical stability to ensure limited decomposition on electrode surface and any reaction with the electrode active material;
- High electrochemical stability to bear the voltage between anode and cathode;
- High boiling point to ensure safety at high temperatures;
- Stability, low price, atoxicity and environmentally friendly;

Electrolytes can be liquid or solid. Liquid electrolytes are the most common and they are composed by two main components: the salt and the solvent.

The salt supplies the charge carriers needed to cycle lithium ions between anode and cathode. It has to dissolve in the solvent and should have a high ion mobility to increase its conductivity. Several salts such as $LiPF_6$, $LiClO_4$, $LiAsF_6$ and $LiBF_4$ have been investigated, showing that $LiPF_6$ is the best one for commercial systems due to its thermal stability and easy and cheap production.

The solvent needs to dissolve the salt and must be fluid over a wide range of temperatures to allow for rapid ion transfer, as well as safe, cheap and non-toxic. The large potential windows of battery prevent the use of any protic solvents, since protons would be readily reduced at negative electrode while corresponding anions would be oxidized at the positive electrode. The organic polar aprotic solvents relevant to the field of Li-ion batteries include three main families: ethers, esters and alkyl carbonates. Since ethers and esters are not suitable for Li-ion batteries due to the poor passivation of graphite electrodes in their solutions and due to the typical high-voltage working of cathode, the most common solvents are alkyl carbonates (***Figure 9***).

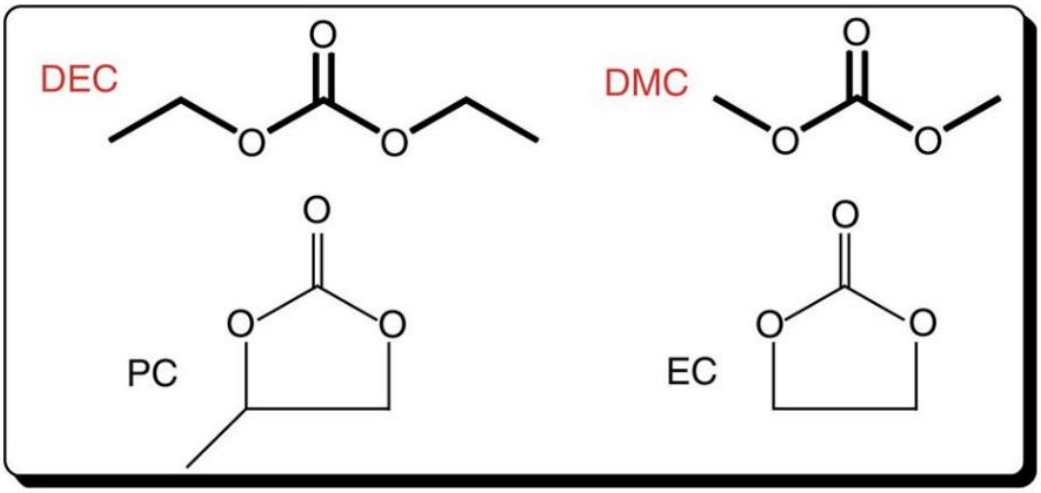

Figure 9: Common alkyl carbonates used in Li-ion batteries: Diethyl carbonate (DEC), dimethyl carbonate (DMC), propylene carbonate (PC), ethylene carbonate (EC);

Ethylene carbonate (EC), with its high dielectric constant, was found to form an effective protective layer (Solid Electrolyte Interphase) on a graphitic anode that prevented any sustained electrolyte decomposition on the anode, while this protection could not be realized with propylene carbonate (PC). However, ethylene carbonate is solid at room temperature and this means that it cannot be used as a single solvent. So, it is used in mixtures containing propylene carbonate or linear alkyl carbonates such as dimethyl-, diethyl- carbonates [10]. Some limitations of use of alkyl carbonates in LIBs arise from the safety of these compounds: they are flammable and at high temperatures they may be very reactive in thermal runaway reactions, which leads to fire and explosions.

2.1.3 Anode Materials

The anode intercalates Li^+ ions during charge and de-intercalates lithium during discharge. The basic characteristics of anode material are:

- The ability of intercalate lithium should be as high as possible in order to achieve a high specific capacity;
- Not undergo modification and structural damage during the intercalation/de-intercalation processes in order to offer a long cycle life;
- Have the working potential (vs Li/Li^+) as low as possible, to prevent dendrite formation;
- Low cost and good durability;

Carbonaceous materials are the most employed materials as negative electrodes in LIBs because they exhibit an excellent reversibility toward the intercalation of lithium ensured by crystallinity, morphology and microstructure of the carbonaceous material. Moreover, they provide high specific capacities, more negative redox potentials than metal oxides and better cycling performance thanks to their structural stability [11].

Some examples are shown below in ***Figure 10***:

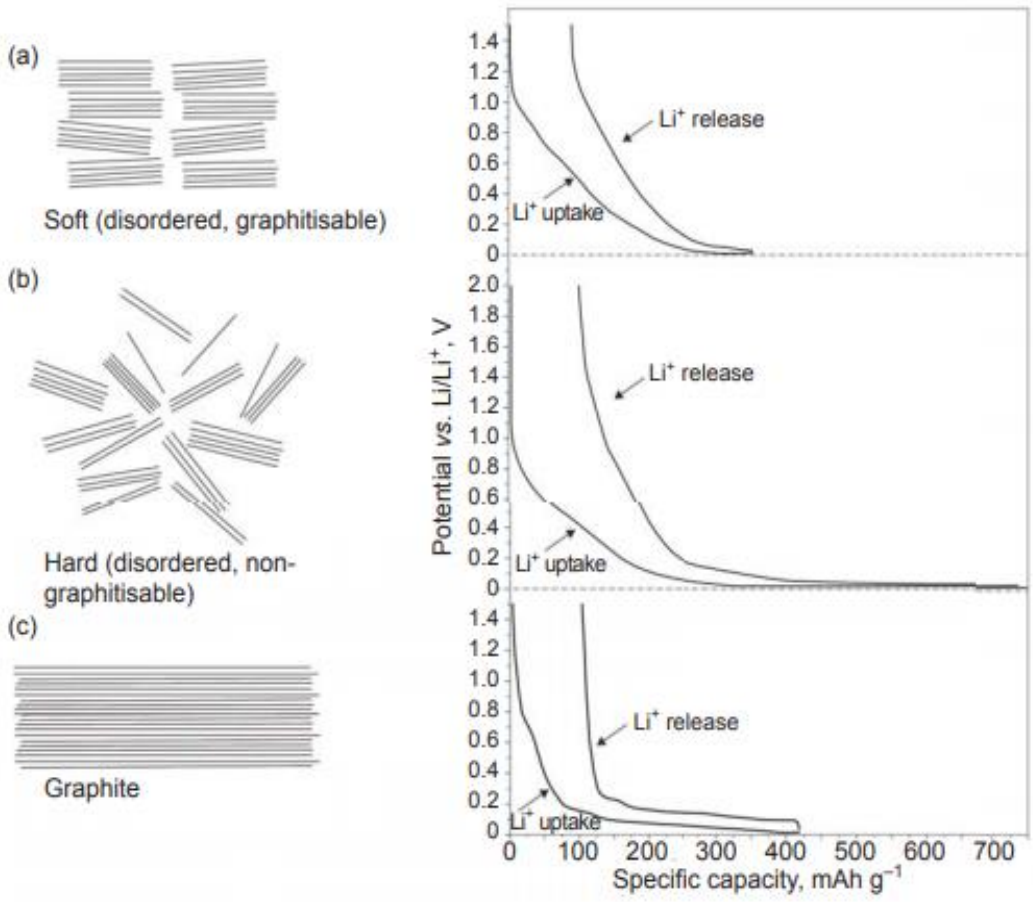

Figure 10: Schematic illustration (left side) of: (a) soft carbon; (b) hard carbon; and (c) graphite structures and (right side) their typical potential profiles;

The first commercial secondary LIB, released by Sony Corporation in 1991, comprised ***Soft Carbon*** (more precisely petroleum coke) as an anode. Its structure can best be described as a poorly crystalline graphite having small crystallite size and random shifts or rotations between adjacent graphitic layers [12] (***Figure 10a***). This type of disorder, called turbostratic disorder, tends to pin adjacent layers together creating a stable material into which Li can intercalate and de-intercalate. However, the disorder also reduces the amount of lithium that can be intercalated to about half the value that can be achieved by highly crystalline graphite [13]. This LIB provided an energy density of 80 Wh/kg, outperforming all other battery technologies present in the market at that time. Moreover, this battery showed a highly reversible and stable cycling behaviour and an extremely high cell voltage of about 4 V.

Hard Carbon have highly disordered structure with predominantly single layer graphene sheets arranged in a random orientation. This structure can be thought of as a "house of cards" [14] where single, double or triple layers of graphene sheets represent the cards. The space created in the voids between cards can be thought of as micropores [15]. Compared to graphitizable carbon (i.e. soft carbon), non-graphitizable carbon (i.e. Hard Carbon), generally has low density, porous surface, small crystallites and relatively random orientation of crystallites. Due to these properties, Hard carbon (***Figure 10b***) offers enhanced specific capacities, leading to an increase of the achievable gravimetric

energy density up to 120 Wh/kg and of the upper cut-off potential to 4.2 V, while presenting excellent cyclability [16]. The increased capacity, that in some cases exceeded the one of graphite (i.e. > 372 mAh/g or Li_xC_6 with x > 1), has been long debated and many attempts have been made to understand the large capacities. It is now accepted that Hard Carbons can deliver high capacity thanks to the random alignment of graphene layers that provides the micropores able to accommodate two layers of lithium atoms leading to a stoichiometry up to Li_2C_6 or 744 mAh/g [14].
However, this kind of material, besides to the low density and high potential hysteresis between charge and discharge, has a large irreversible capacity due to the very large reaction of lithium with electrolyte to form a passivating layer on the electrode surface, called Solid Electrolyte Interphase (See Chapter 2.1.4).

In summary, it can be stated that, despite hard and soft carbons enable efficient energy conversion and storage, the desired application of LIBs in cellular phones required the replacement of such anode materials, as the voltage drop in the potential profile of both amorphous carbons upon (dis-) charge (***Figure 10a-b***) results in a substantially varying overall cell voltage, while cellular phones need an operational voltage of at least 3V. In addition, the utilisation of these anode materials suffered a severe safety issue. In order to achieve the maximum specific capacity, the cathodic cut-off potential (i.e. the end-of-charge potential for the anode) must be set close to 0V vs. Li/ Li^+, thus, again posing the risk of metallic – in worst case dendritic – lithium plating on the carbon particles surface. For these reasons a new anode material was required. Graphite advantageously addresses all these issues rather satisfactorily and is thus still the most commonly employed anode material in today's commercial LIBs [16].

In contrast to soft and hard carbons, ***graphite*** shows a rather flat potential profile when reversibly hosting lithium-ions at potentials below 0.5V vs Li/Li^+ (***Figure 10c***). Additionally, it offers a significantly higher energy density of 165 Wh/kg with limited irreversible capacity.
There are different kinds of graphitic electrode materials, such as natural and artificial graphite, mesocarbon microbeads (MCMB), and highly disordered or amorphous carbons [17]. Basically, the ***graphitic carbon materials*** are composed by extended sheets of sp^2-hybridized carbon atoms arranged in hexagonal rings extended in two dimensions. Van Der Waals force stacks these sheets into ordered structures called crystallites. The two possible patterns for ordered stacking graphene layers, Bernal stacking (ABA sequence) and Rhombohedral stacking (ABC sequence) are shown in ***Figure 11***:

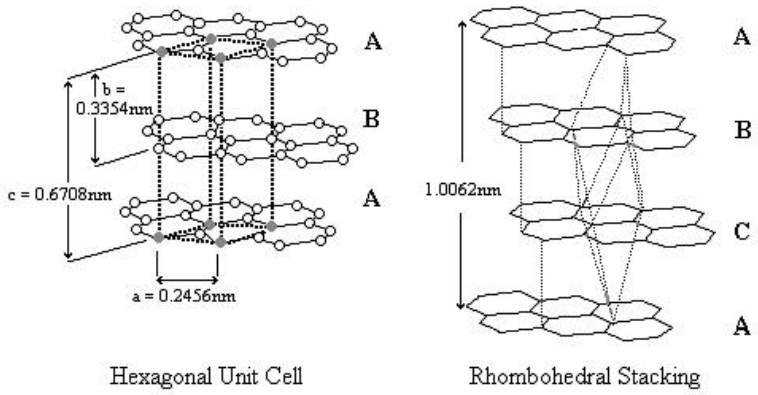

Figure 11: Stacking arrangements of graphite;

The former possesses a little more thermally stable hexagonal symmetry, while the latter has a rhombohedral symmetry. Graphite usually comprises both crystal structures, but the rhombohedral content seems always less than 30%. The Van Der Waals forces between graphene layers is so weak that the planes easily slide [6]. The ideal structure of graphite is never obtained in practice, due to the ever-present high density of stacking faults and structural defects.
The electrochemical insertion of lithium into graphite, called intercalation, occurs through the following reaction:

$$xLi^{+} + xe^{-} + 6C \dashrightarrow Li_xC_6 \qquad \text{(Reaction 4)}$$

This means that under ambient conditions, a maximum of one lithium per six carbons (LiC_6) is expected to be intercalated in the Van Der Waals gaps above and below a carbon hexagon. This corresponds to a specific theoretical capacity of 372 mAh/g. Upon intercalation, the graphite structure shifts to an AA stacking type as shown in ***Figure 12***. Due to the lithium intercalation, the interlayer distance between the graphene layers increased moderately: 10.3%, calculated for LiC_6 [18,19]. In LiC_6 the lithium is distributed in-plane in such a manner that it avoids the occupation of the nearest neighbouring sites.

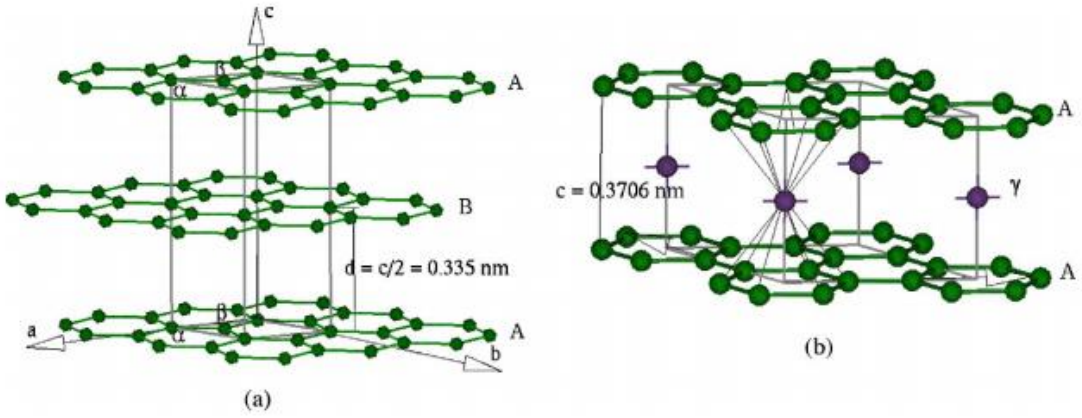

Figure 12: (a) Schematic drawing of the crystal structure of hexagonal graphite showing the AB layer stacking sequence and the unit cell. (b) Structure of Li-intercalated graphite compound LiC6 (stage 1);

Even if graphite is still the commercial anode material in LIBs, as with soft and hard carbons, it entails the inherent risk of metallic lithium plating, an intrinsically limited high rate capability upon charge and a very high reactivity towards the electrolyte in the lithiated state, which might result in thermal runaway [16].

Another interesting anode material is ***graphene***, that is a single sheet of graphite in which electrons can flow freely in the lattice at room temperature because of the very low electric resistance coming from its high order structure. Furthermore, it has a high specific capacity (744 mAh/g), twice as much as graphite, due to the fact that lithium is adsorbed on each side of the graphene sheet, on the edges and also in covalent sites during the Li intercalation. Therefore, the process affords the formation of fully lithiated graphene (Li_2C_6). Another important feature of graphene is its high surface area (492.5 m^2/g) compared to graphite (8.5 m^2/g). However, the graphene structure is quite unstable and tends to re-stack into amorphous carbon and graphite.

2.1.4 Solid Electrolyte Interphase (SEI)

One of the main obstacles restraining the improvement of lithium-based battery performance is the electrode/electrolyte interface, which is the key to understand battery electrochemistry. This interface is usually further complicated by a passivation layer on the electrode surface [20], called ***Solid Electrolyte Interphase***.

The Solid Electrolyte Interphase (SEI) is a passive layer composed by inorganic and organic electrolyte decomposition products, which arise from the reduction at the negatively polarized electrode surface during first charge of the Li-ion battery. The formation of the SEI is due to the high reactivity of the intercalated lithium that reacts immediately with the liquid electrolyte components, i.e. the solvents and the lithium salt. This occurs when the redox potential of the electrodes used in a battery lies outside the electrochemical window of the electrolyte, and it undergoes reduction. Unlike it can be imagine, the SEI is very important because it allows Li^+ transport and blocks electrons in order to prevent further electrolyte decomposition and ensure continued electrochemical reactions [20]. Moreover, the SEI film prevents further decomposition of the electrolyte in the successive cycles in order to ensure low irreversible capacity (constant and high reversible capacity) all along the charge/discharge cycles [21].

The onset potential of SEI formation is not a fixed value: it depends on factors like nature and composition of electrolyte, nature of additives used in the electrolytes [22], etc. It is desirable to have complete SEI formation before Li-ions intercalation begins. This make the graphite the ideal anode since the SEI formation starts at about 0.9V, while Li^+ intercalation mostly occurs below 0.3V.

From a compositional point of view, the SEI film can be viewed as a multi-layered structure, wherein each layer has a mosaic structure whose composition, structure, and properties evolve with time. Generally, SEI is composed by an inorganic inner layer near the electrode/SEI interface (Li_2CO_3, LiF, and Li_2O), that allows Li^+ transport, an organic (dilithium ethylene glycol carbonate (Li_2EDC) and ROLi, where R depends on the solvent) outer layer, which is heterogeneous, porous, and permeable to both Li^+ and electrolyte solvent molecules, near the SEI/electrolyte interface. ***Figure 13*** shows a representation of SEI on graphite surface:

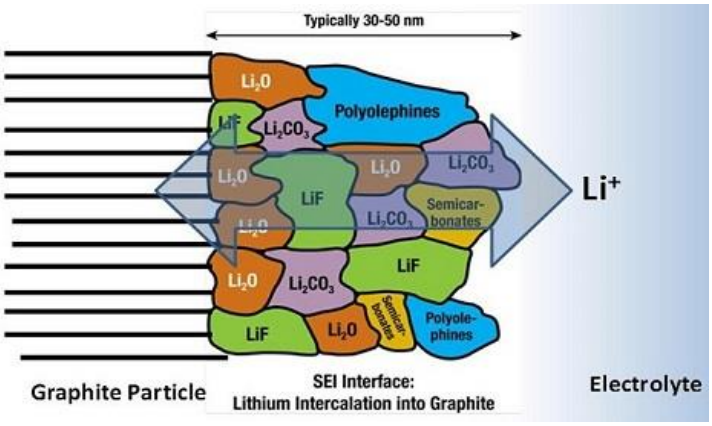

Figure 13: Peled model of SEI;

The battery performance is affected by many SEI parameters (thickness, morphology, compactness, chemical composition) as well as carbonaceous material properties, including bulk (crystallographic composition, particle morphology, specific surface area) and local surface properties [23]. It is worth to note that irreversible capacity loss in the first cycle is mainly due to the electrolyte reduction and SEI formation. However, the most important consequence of SEI is on the safety of the battery: the large volume change due to the SEI growth might induce the damage of the SEI itself and possible safety issues.

2.1.5 Binders

The binder is a fundamental component in the production of an electrode because it binds the active material together and with other conductive carbons and allow the particles to adhere to the current collector.

Generally, a good binder must meet the following requirements:

- Electrochemical stability over a wide potential range;
- Chemical stability upon oxidation and reduction;
- Excellent adhesion to metal electrodes;
- Good electron and Li^+ ion conductivity;
- Environmentally friendly;

The choice of the type and amount of binder in the electrode composition is also very important to optimize electrode cost, energy density, stability and production procedure [24].

Polyvinylidene fluoride (PVdF) is the most common binder in lithium-ion batteries. It is a pure thermoplastic fluoropolymer highly stable and its structure is shown in ***Figure 14***:

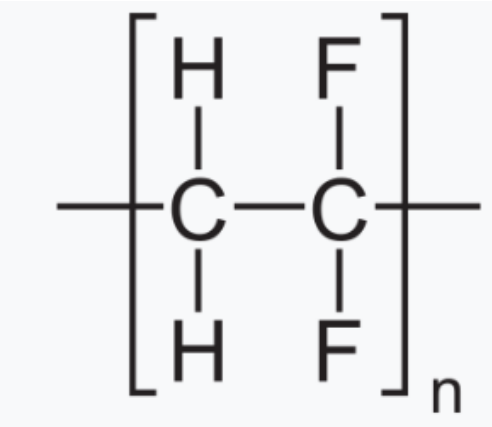

Figure 14: Polyvinylidene Fluoride (PVdF);

Its main features are the good mechanical resistance, high solubility in polar solvents, good resistance to strong acids, oxidizing agents, UV and extreme temperatures. Furthermore, it has a good electrochemical stability that allow to use it as binder for both anode and cathode electrodes. However, the main disadvantages of this binder are that it is expensive, toxic and has to be solubilized in an organic solvent, N-methyl pyrrolidone (NMP) that is expensive, volatile and toxic as well. Moreover, at elevated temperatures, all fluorinated polymers react with lithium metal and lithiated graphite to form more stable compounds such as LiF. For all these reasons, there is currently a trend to replace the PVdF with non-fluorinated binders and soluble in inexpensive and environmentally friendly solvent. Among them, one of the most interesting is certainly the sodium salt of carboxymethyl cellulose (Na-CMC).

Sodium salt of Carboxymethyl Cellulose (Na-CMC) is a linear polymeric derivative of cellulose, consisting of beta-linked glucopyranose residues with varying levels of carboxymethyl (-OCH2COO-Na^+) substitution. It is formed by the reaction of cellulose with NaOH and chloroacetic acid. The presence of carboxymethyl groups is responsible for the aqueous solubility of CMC relative to insoluble cellulose. It is therefore weak polyacid that dissociates to form carboxylate anionic functional groups. The other predominant functional group on CMC is the hydroxyl, which is partly replaced by the carboxymethyl group during derivatization [25]. The structure of CMC is shown in ***Figure 15***:

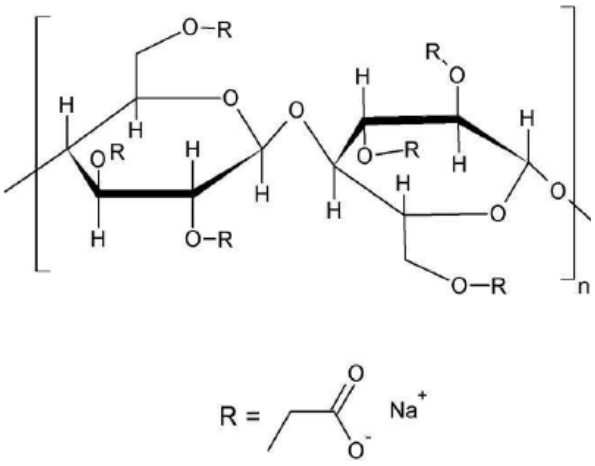

Figure 15: Structure of Na-CMC;

The various properties of CMC depend upon three factors: molecular weight of the polymer, average number of carboxyl content per anhydroglucose unit and the distribution of carboxyl substituents along the polymer chain. The greatest advantage of CMC is its solubility in water that avoids the use of hazardous, non-green and volatile organic solvents. A further advantage of CMC resides in its easy disposability at the end of the life of the battery: once the electrode is extracted, the active electrode material can be easily recovered by pyrolysis of the binder. Finally, the CMC industrial price of CMC is about 1 order of magnitude lower than PVdF.

2.2 Na-ion Batteries

In recent years the development of the sodium-ion batteries has become more active, which is supported by the sodium wide occurrence and relatively low price of the raw material. The sodium content in lithosphere is estimated as 2.5%, which exceeds that of lithium by almost three orders of magnitude. Besides, the sodium-ion batteries are expected to demonstrate higher stability and safety. The sodium-ion batteries operation mechanism and design are analogous to those of the more known lithium-ion batteries. However, the materials allowing lithium reversible incorporation are unsuitable for reversible incorporation of large quantity of sodium. This is due, first of all, to the difference in the size of lithium and sodium ions (0.076 and 0.102 nm, respectively), which refers to the materials of both negative and positive electrodes. This affects the phase stability, the transport properties and the interphase formation. This is precisely why the problem of development of effective sodium-ion batteries is mainly reduced to the creating of electrode materials [26].

Some general differences between lithium and sodium cells are immediately apparent:

- The lower melting point of sodium (Tm_{Na} = 98 °C) as compared to lithium (Tm_{Li} = 181 °C) and its generally higher chemical reactivity pose additional safety issues for cells using metal anodes. On the other hand, cell concepts with a molten anode might be easier to realize given the advantages of better kinetics and prevention of dendrite formation;
- Sodium is less reducing than lithium, meaning that more substances are stable in direct contact with the metal;
- The total number of known sodium compounds is larger compared to lithium, so cell reactions might require more intermediate steps or stop at a different stoichiometry. Two notable exceptions exist that might be of advantage for sodium cells. Aluminium forms binary alloys with lithium but not with sodium. Therefore, aluminium instead of the more expensive copper can be used as a current collector for the negative electrode in sodium batteries;
- The larger sizes of the sodium atom and ion compared to lithium lead to larger volume changes during cycling. Sodium-based electrodes might therefore degrade faster and the formation of stable interfaces might become more difficult. But the smaller size of the lithium ion corresponds to a larger charge density, and the lithium ion polarizes its environment stronger than the sodium ion. This causes severe differences in chemical bonding and ion mobility;

- The solubility of sodium and lithium compounds in solvents are different. The discharge products and/or interphases (SEI formation) can therefore dissolve to different degrees and electrolyte solutions might have different properties;

Overall, Sodium-Ion Batteries (NIBs) generally exhibit lower electrochemical performances and energy densities than LIBs (~ 150 Wh/kg against ~ 170 Wh/kg), mainly due to the reduced operation voltage (-2.7V vs SHE against -3.0 vs SHE of LIBs) and to the large size of Na^+ that results in significant differences in the host structure of the intercalated and deintercalated materials [27]. Moreover, the different surface passivation processes with respect to LIB technology can influence on electrochemical properties. Although all these differences are more significant when considering metallic lithium and sodium electrodes, the variances become smaller considering intercalation materials as electrode. Since the final technology will be based on intercalation materials, the energy loss is significantly reduced: for example, the theoretical capacity of $LiCoO_2$ and $NaCoO_2$ is reduced by only 14% in the Na compound compared to the Li one [28]. Anyway, the electrochemical performance, energy density and cost of NIBs have to be improved in order to become a competitive technology for stationary applications.

2.2.1 Cathodic Materials

Since the working mechanism of NIBs is the same of LIBs, cathode on sodium batteries must meet the same characteristics as well as lithium systems. Among variety of cathodic materials, the most popular groups of compounds are layered oxides and compounds with polyanions.

Layered oxide compounds that are of interest as cathodic materials have a common formula $NaxMO_2$, where M denotes one or several transition metals (Ti, V, Cr, Mn, Fe, Co, or Ni). Among the compounds $NaxMO_2$ (where M is a single metal) the most popular are the manganese-containing ones, with a theoretical capacity that does not exceed 200 mAh/g [27]. Depending on the sodium content, the layered oxides can be classified as types O3, O2, P2 and P3 (***Figure 16***) where the letters O and P denote the Na^+ ion Octahedral and trigonal Prismatic coordination, while the characters 2 and 3 correspond to the number of layers in elementary cells, respectively (according to the classification proposed by Delmas et al. [29]).

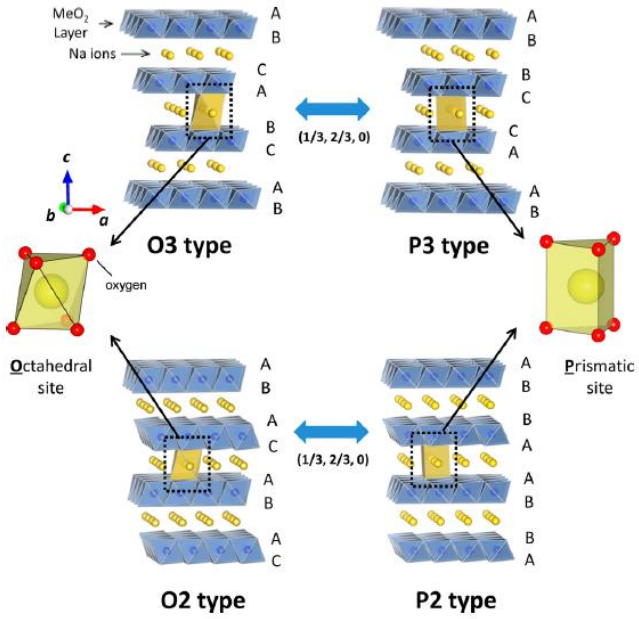

Figure 16: Classification of Na−M−O layered materials and phase transition processes induced by sodium extraction;

Most cathode materials studied so far crystallize in O3-type and P2-type. The P2-type compound shows higher capacities but also higher irreversibility in the first cycle (50 mAh/g) than the 03 [30,31]. Generally, sodium extraction from O3- and P2- type phases induces phase transitions to P3-type and O3-type respectively, since the new phase is energetically more stable after the extraction of sodium and the consequent formation of vacancies. Among them, manganese and iron based layered oxides are the most studied due to their abundance and therefore low cost. P2-$Na_{2/3}[Fe_{1/2}Mn_{1/2}]O_2$ is a promising layered oxide in terms of cost and energy density. This material delivers high reversible capacity (190 mAh/g) when cycled between 1.5-4.3V vs Na/Na^+ and has an energy density comparable to that of LFP, considering metallic anode.
Although the P2-type Na−Fe−Mn system is a promising candidate as a high-capacity positive electrode material for NIBs, three major drawbacks are known for electrode materials:
a large volume change (11.3% shrinkage after charge to 4.2V) during electrochemical cycles, its hygroscopic character, which restricts sample handling in moist air and the sodium deficiency in the as-prepared sample which limits the charge capacity in a full-cell configuration, unless an additional source of sodium ions is added [28].

Polyanionic compounds, such as phosphates, pyrophosphates, fluorophosphates, sulfates and their combinations have been reported as possible cathode materials. Although polyanions typically exhibit lower specific capacity than layered oxides, they provide good specific capacity at low and high current densities, good thermal stability and good cycle life due to their stable framework during Na^+ deintercalation/intercalation processes [32].
Among the polyanionic compounds used as cathode materials, $NaFePO_4$ (NFP) olivine type and pyrophosphates of general formula $NaT_mP_2O_7/Na_2T_mP_2O_7$ (where Tm is a transition metal such as V, Fe, Ti, Co, Mn, Cu) are good candidate for practical application, even if further optimization has to be carried out.

2.2.2 Electrolytes

The electrolyte nature affects the performance of sodium-ion batteries markedly. Currently different electrolytes (aqueous and non-aqueous solutions, ionic liquids, polymer and gel-polymer, ceramic and vitreous electrolytes) have been tested. In the choice of electrolyte, the important properties are not only ionic conductivity, electrochemical stability window, thermal and mechanical (for solid electrolytes) strength, safety, economical and ecology factors, but also the mechanism of their interaction with electrode materials and properties of the SEI formed. The most used electrolytes are liquid non-aqueous based ones, that is, sodium salt solutions in individual or mixed aprotic solvents [26].

Na-salts generally have advantages in terms of safety due to their higher melting point and thermal stability compared to Li-salts. Among the sodium salts, sodium perchlorate (***$NaClO_4$***), hexafluoroposphate (***$NaPF_6$***) followed by bis-trifluorosulfonylimide ($NaN(CF_3SO_2)_2$, NaTFSI) are the most used. All of them exhibit different drawbacks: $NaClO_4$ is toxic, hygroscopic being difficult to dry and its powder is shock sensitive; PF_6^- anion in $NaPF_6$ undergoes hydrolysis reaction forming PF_5, POF_3 and HF, instead, NaTFSI has lower limit voltages due to the anion $TFSI^-$ that starts to corrode aluminium collector at 3.3-3.5 V vs Na/Na^+ [33]. On the other hand, Sodium perchlorate or hexafluorophosphate allow an increase of the voltage window up to 5 V [34,35].

Analogously to LIBs, a mixture of organic compounds is used as solvent in order to obtain high dielectric constant for an easy salt dissociation, long liquid range, low viscosity and high ionic conductivity. Propylene carbonate (PC), ethylene carbonate (EC), dimethylcarbonate (DMC), diethylcarbonate (DEC), tetrahydrofuran are used in mixtures.

To improve the safety of the battery, electrolytes based on sodium salt solutions in ionic liquids are ever popular. The ***ionic liquids*** are incombustible, have low volatility and high thermal (up to 150°C) and electrochemical stability (between 0 and 5 V); moreover, the sodium salt concentration may be rather small [26]. However, ionic liquids usually require higher operating temperatures than liquid electrolytes because of their high viscosity and melting points which are often just barely above room temperature [33].

Finally, ***polymer electrolytes*** can, in principle, offer some advantages such as higher flexibility of the batteries and the ability to balance the electrodes volume changes during their cycling. At this point, polymer electrolytes on basis of polyethylene oxide (PEO), polyacrylonitrile, polyvinyl alcohol, Nafion with sodium-ion-conductivity have been studied. However, studies of particular electrodes performance contacting the polymer electrolytes are still very rare [26].

2.2.3 Anodic Materials

Research on negative electrode materials for NIBs has been developed on the four different categories, which are basically identical to those for LIB:

- Carbons and carbonaceous materials;

- Oxides and polyanionic compounds;
- p-block elements (metals, alloys, phosphorus/phosphide);
- oxides and sulphides with conversion reaction;

For LIBs, graphite is widely used as a negative electrode material in comparison with other carbon materials because of its high gravimetric and volumetric capacity. By electrochemical reduction, Li^+ ions are inserted between graphene layers and Li−graphite intercalation compounds (GIC) are formed with stage transformations [36]. However, graphite is electrochemically less active in Na cells. Although a small amount of Na atoms seems to be inserted into the graphite, the Na insertion amount is much smaller than that for Li and K insertion.

On the contrary, ***Hard Carbons (HCs)*** show better electrochemical performances and therefore are one of the most employed anode materials for NIBs. The structure of hard carbon depends on the synthesis conditions such as carbon sources and pyrolysis temperatures, resulting in the difficulty to construct a universal structural model of hard carbon. In all of the proposed models, hard carbon is composed of two domains: carbon layers (graphene-like) and micropores formed between disorderly stacked carbon layers [28] (See Chapter 2.1.3). Although the true nature of the reaction mechanism of Na^+ insertion/extraction is still controversial, S. Komaba et al. [37] data demonstrate the structural change of hard-carbon, indicating the reversible Na insertion into disordered stacked graphenes and nanopores of hard-carbon. Consequently, at least two different mechanisms of electrochemical sodium insertion exist for hard-carbon. One is the alkali insertion between the graphene sheets, demonstrated by the sloping region between 1.2 and 0.2V in the galvanostatic curves (***Figure 17***) of Li and Na cells; the other is the reversible alkali insertion into the nanopore, which is of significance for the Na system compared to the Li system, and should be attributed to the plateau between 0.2 and 0.0 V for Na system, and close to 0 V for Li system.

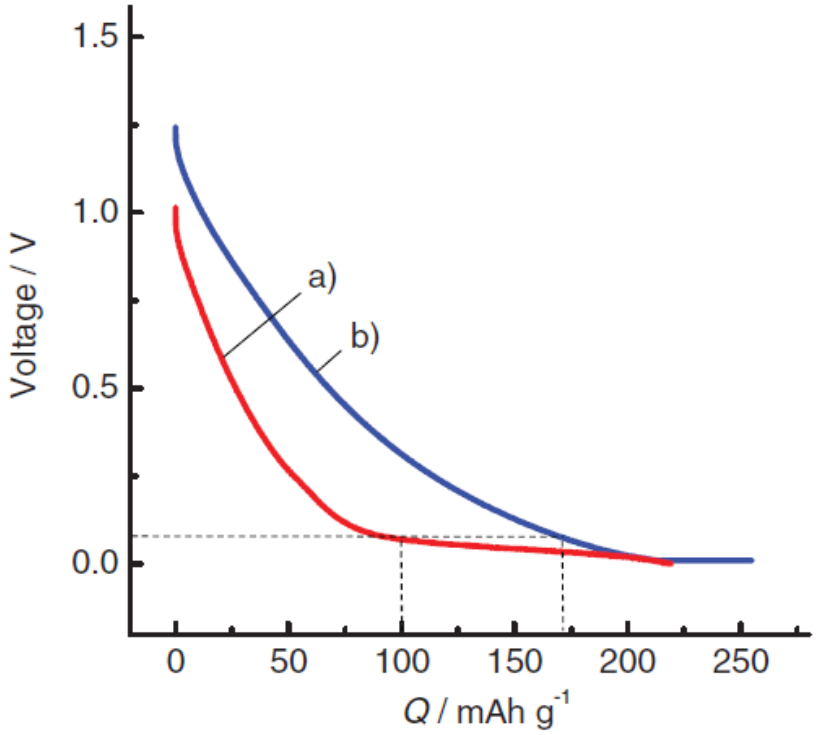

Figure 17: Chronopotentiograms of the second reduction for hard-carbon electrodes in a) Na cell and b) Li cell, respectively, at a rate of 25 mA/g [37];

Another promising family of anode material are ***Titanium-based oxides***, which are cheap, low toxic and safe also at high current densities [38]. There is a wide variety of reported compounds which can reversibly insert Na^+ such as binary oxides (many TiO_2 polymorphs), ternary oxides with general formula $A_xTi_nO_{2n+1}$ or $A_xTi_nO_{2n+2}$, such as $Na_2Ti_3O_7$, quaternary oxides and NASCION type structure.

2.2.4 Solid Electrolyte Interphase (SEI)

SEI play a key role also in cycle performance of NIBs and should meet the same requirements of LIBs (See Chapter 2.1.4). However, ***Figure 18*** shows the difference of surface layers forming by electrochemical cycling of sodium and lithium cells.

After the electrochemical tests done by S. Komaba et al. [37], the peak at 284.5 eV (assigned to the sp^2 carbon in C-C of graphene of HC) almost disappeared, indicating that hard-carbon in both cells is covered with the decomposition products of the electrolyte. The peaks were assigned to various compounds such as alkali carbonate of A_2CO_3 (A = Li or Na) and alkyl carbonate of $ROCO_2A$ at 290.0–290.5 eV, ester linkage (-CO-O-) at 286.8 eV, and $-CH_2-$ at 285.5 eV, that is originated from the alkyl and alkylene groups and polymer species [39]. The more marked difference is the peak intensity at 285.5 eV, that is stronger for the Li cell than that in the Na cell. This means a larger amount of hydrocarbon compounds in the surface film formed in the Li cell. Moreover, the surface film in the Li cell was mainly composed of the organic compounds while that in sodium was composed of the inorganic compounds [37].

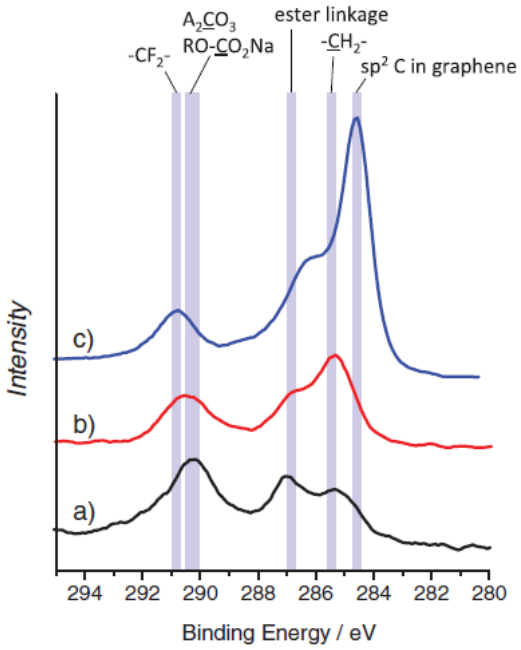

Figure 18: XPS carbon spectra for the hard-carbon electrodes tested in a) sodium and b) lithium cells after the first cycle, and c) pristine electrode;

Anyway, though the morphology and chemical composition of the SEI are different, it works as a passivation film in both cells, which similarly protects the sodium and lithium inserted hard-carbon from the chemical reactions with the electrolyte at interface.

2.2.5 Binders

Binders are the same as those used in lithium-ion batteries (see Section 2.1.5)

3. CHARACTERIZATION TECHNIQUES

3.1 Structural and Morphological Techniques

3.1.1 Thermogravimetric Analysis (TGA)

Thermogravimetric Analysis (TGA) is the branch of thermal analysis that examines the mass change of a sample as a function of the temperature in the scanning mode or as a function of time in the isothermal mode.

A schematic representation of the instrument is shown in ***Figure 19***, in which the main components are:

- Thermobalance;
- Sample Holder;
- Oven;
- Temperature Progammer;
- Record System;

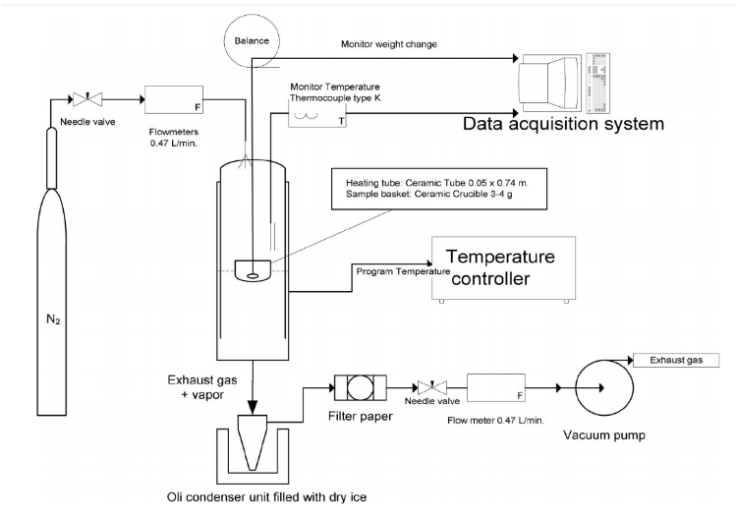

Figure 19: Schematic representation of TGA instrument;

The atmosphere must be controlled because it determines the nature of the processes and reactions involved: it can be oxidative (air, O_2) reductive (H_2) or inert (He, Ar, N_2). The result of TGA is a thermogram that shows the mass loss percentage as a function of the temperature (or time).

TGA is mainly used to determine:

- Temperature and weight change of decomposition reactions, which often allows quantitative composition analysis;
- Water content or the residual solvents in a material;
- Evaporation rates as a function of temperature;
- Plastics and organic materials by measuring the temperature of bond scissions in inert or oxidative atmospheres;
- The purity of a mineral, inorganic compound, or organic material;

3.1.2 X-Ray Diffraction (XRD)

X-Ray Diffraction (XRD) is a non-destructive technique that provides information about the structure in a crystalline material: unit cells parameters, bond length and angle, atomic position and occupancies, and other useful details. Since the interatomic distances are in the same order of magnitude of the x-ray's wavelength, the interaction between x-rays and unit cells gives rise to a characteristic diffraction pattern coming out as a consequence of coherent scattering. This diffraction pattern constitutes a fingerprint that can be compared with diffraction patterns collected in the database, making possible the identification of unknown material.

Figure 20 shows a schematic representation of a diffractometer and of the interaction between the samples and the incident electromagnetic radiation:

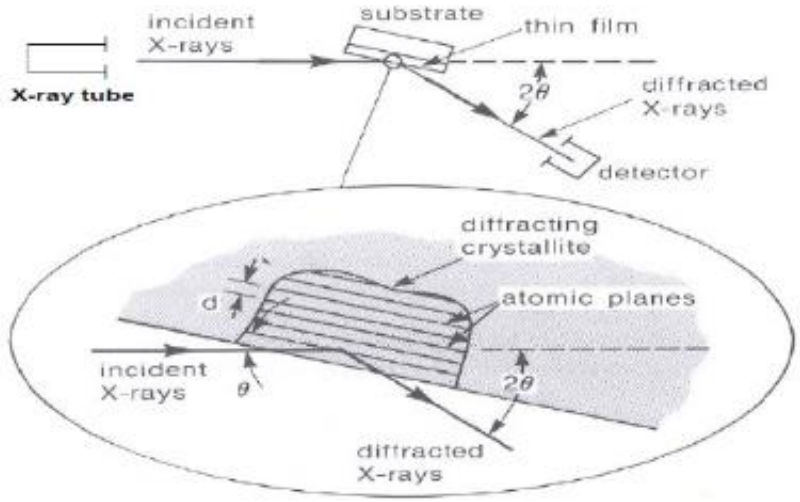

Figure 20: Schematic representation of how XRD works;

In this technique, an incoming X-ray interacts with the electrons of an atom that starts to oscillate at the same frequency of impinging wave. The oscillation produces secondary waves that add constructively in few specific directions and interact destructively in most directions. The constructive interference (and a diffracted ray) occurs when conditions satisfy ***Bragg's Law***: the scattered waves must remain in phase and this is possible if the difference in the path length of each wave is equal to an integer multiple of the wavelength.

$$n\lambda = 2dsin\theta \qquad (eq.4)$$

Where d is the interplanar distance, θ is the incident angle, n is any integer and λ is the wavelength of the beam.

As a result, these specific directions appear as spots on the diffraction pattern. Plotting the diffraction pattern as scattered intensity vs the scattering angle (2θ), peaks are obtained with the following characteristics:

- Position: it is determined by the wavelength of the incident beam and by the interplanar distance d. It is the "fingerprint" of the sample;
- Intensity: it is a function of atoms coordination in the unit cell;
- Shape: it is determined by sample crystallinity, crystallite size, strain etc.;

3.1.3 Raman Spectroscopy

Raman Spectroscopy is a non-destructive scattering technique that can be used for both qualitative and quantitative purpose. Qualitative analysis can be performed by measuring the frequency of scattered radiations while quantitative analysis can be performed by measuring the intensity of scattered radiations.

The technique is based on the Raman Effect that arises when a small fraction of scattered radiation is different from frequency of monochromatic radiation. The frequency of the scattered photons is usually lower than the incident photon, this means that an inelastic scattering occurs through the interaction between the incident radiation and vibrating molecules. Going into details, in Raman Spectroscopy the sample is illuminated with a monochromatic laser beam which interacts with the molecules of sample and originates a scattered light. Much of this scattered radiation has a frequency which is equal to frequency of incident radiation and constitutes Rayleigh Scattering (elastic scattering). Only a small fraction of scattered radiation has a frequency different from frequency of incident radiation and constitutes Raman scattering (inelastic scattering), that is used to construct a Raman spectrum, which is presented as an intensity vs wavelength shift. When the frequency of incident radiation is higher than frequency of scattered radiation, Stokes lines appear in Raman spectrum. But when the frequency of incident radiation is lower than frequency of scattered radiation, anti-Stokes lines appear in Raman spectrum [40]. In standard conditions, Stokes diffusion is more intense than anti-Stokes diffusion mostly due to the higher population of lower vibrational levels according to the Boltzmann distribution. Thus, Stokes bands are measured in conventional Raman Spectroscopy while anti-Stokes bands are measured with fluorescing samples because fluorescence causes interference with Stokes bands [41].

A schematic representation of Raman spectrometer is shown in ***Figure 21***:

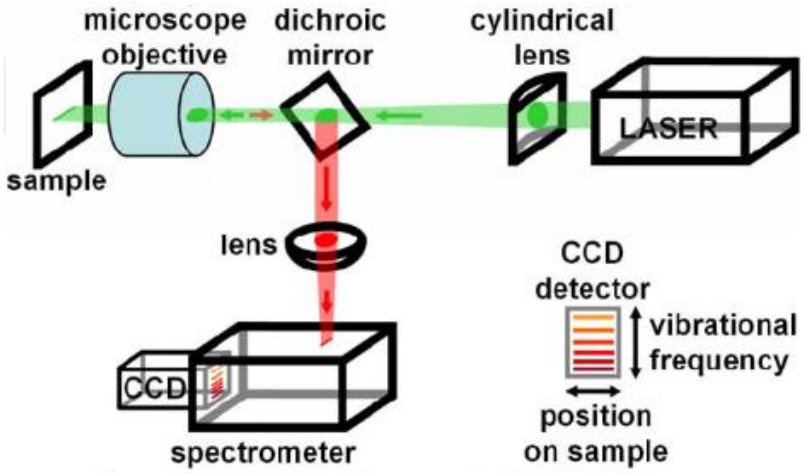

Figure 21: Layout Raman Spectrometer;

3.1.4 Scanning Electron Microscopy (SEM)

Scanning Electron Microscopy (SEM) is a technique in which a high energy very thin electron beam is finely focused over a sample and swept in a roster across the surface. The electron beam/sample interactions cause the emission of different signals, which are collected by a specific detector and converted into an image of the sampled area [42].

The main signals produced are:

- Secondary and backscattered electrons that give morphological and topographical information about the surface of the solid sample;
- Characteristic X-rays that permit both qualitative and quantitative analysis of the sample, since the characteristic X-rays are specific for each element;

SEM can be divided into 4 main parts (***Figure 22a***): the electron gun, the electron optics system, the sample holder and the electron detector and recording system, which provides the collection of the signals and the image formation. The electron gun (***Figure 22b***) must provide a stable source of electrons with high current density and brightness, small emission region at the crossover point and low energy spread in order to prevent interferences between the electrons. The electron optics system (***Figure 22c***) allow to de-magnify and focus the electron beam over the sample: it is composed by electron lenses and apertures that allow to increase the resolution and improve the quality of the image. Finally, in ***Figure 22d***, the interaction volume of the beam/sample in which the scattering events take place is shown.

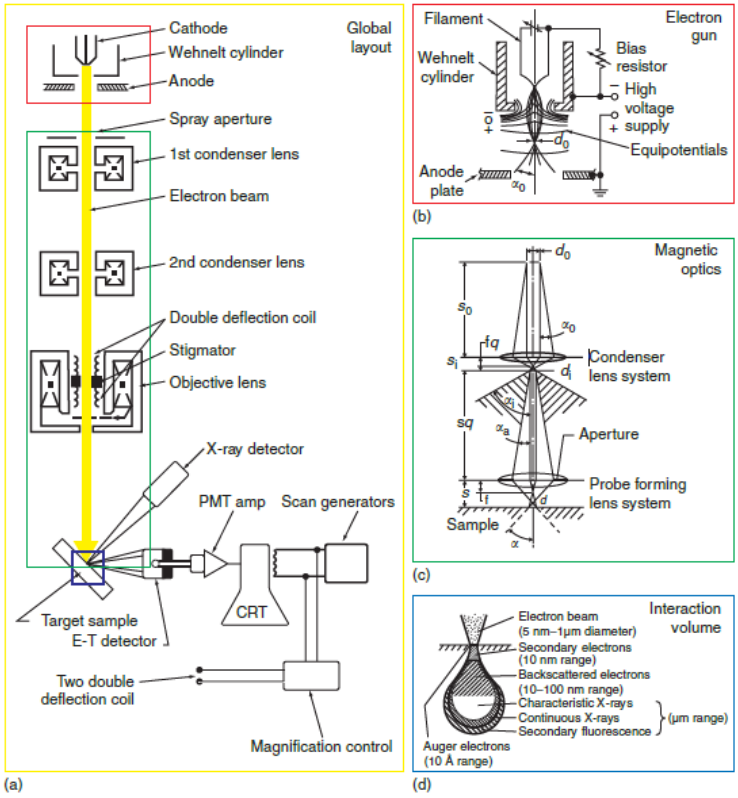

Figure22: a) Global layout b) Electron gun c) Magnetic optics d) Interaction Volume of SEM;

3.2 Electrochemical Characterization

3.2.1 Cyclic Voltammetry (CV)

Cyclic voltammetry (CV) is an electroanalytical technique used to characterize an electrochemical system. It is a potentiodynamic electrochemical measurement in which a potential ramp is applied to the working electrode to gradually change potential and then reverses the scan, returning to the initial potential. ***Figure 23*** shows a typical reduction occurring from point (a) to (d) and an oxidation from (d) to (g). The potential first scans negatively, starting from a higher potential (a) and ending at a lower potential (d), that is the switching potential: the point where the voltage is sufficient enough to have caused an oxidation or reduction of the electroactive species. The reverse scan occurs from (d) to (g), and is where the potential scans positively. It is important to note that some analytes undergo oxidation first, in which case the potential would first scan positively. The scan rate, that controls how fast the applied potential is scanned, is an important parameter and can be varied. Fundamental it is to not apply relatively fast scan rates since they lead to a decrease in the size of the diffusion layer that reflects in high currents [43].

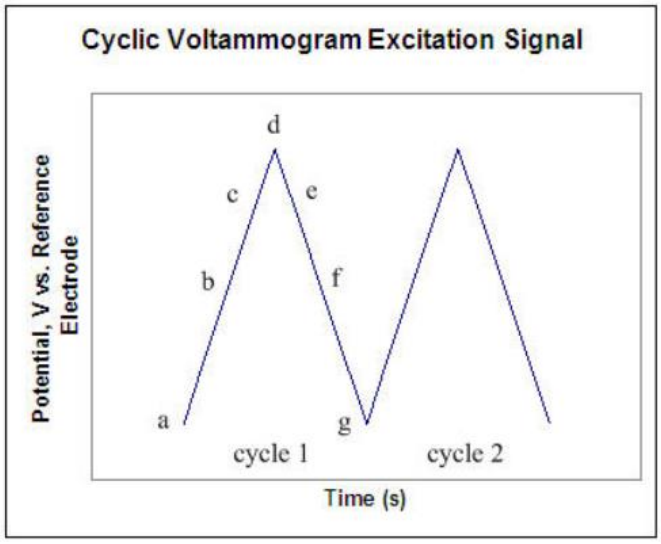

Figure 23: CV excitation signal;

During the potential sweep, the potentiostat measures the current resulting from the applied potential. These values are then used to plot the CV graph of current versus the applied potential. The ***Figure 24*** shows a theoretical cyclic voltammogram for a reversible case [44], where I_{pc} and I_{pa} are, respectively, the cathodic and anodic peak heights, E_{pc} and E_{pa} the cathodic and anodic peak potential:

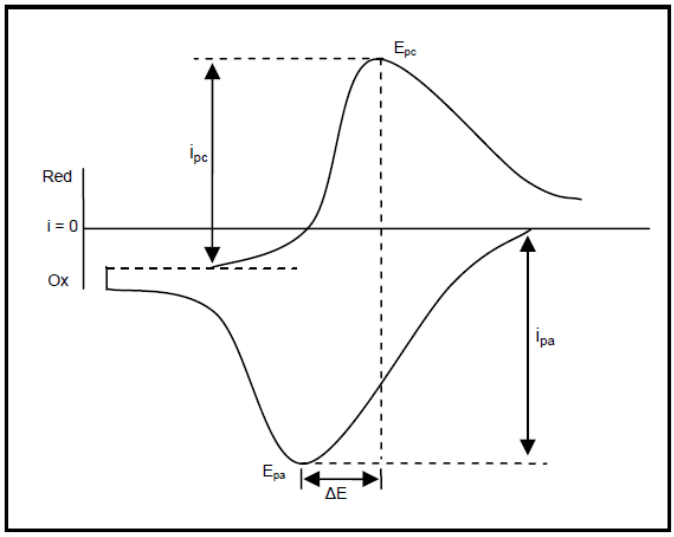

Figure 24: Theoretical cyclic voltammogram for a reversible case;

A single CV cycle is not very useful since it refers only to the events that occur during the electrochemical reaction. It can be used for determining whether or not a species is electroactive and the number of electrons transferred in a reaction. On the contrary, multiple CV experiments (also run in different conditions) can be used for a variety of applications, including:

- the determination of the reversibility of the electrochemical reaction;
- rate constants of charge transfers;
- formation constants;
- reaction mechanisms;
- diffusion coefficients of species;

3.2.2 Galvanostatic Cycling with Potential Limitation (GCPL)

Galvanostatic Cycling with Potential Limitation (sometimes alternatively known as chronopotentiometry) is a potentiometric electrochemical technique that can be used to obtain information about the electrochemical and thermodynamic processes involved.
In this technique, a constant and controlled current is applied between a working electrode and an auxiliary electrode, while monitoring the potential of the working electrode versus a reference electrode during time. The applied current will produce the reduction/oxidation of the electroactive species at the working electrode and thus the potential will move towards the characteristic potential of the redox couple involved in the process. Moreover, the potential will change with time accordingly to changes in the concentration of the reduced and oxidized forms of the electroactive species, following the ***Nernst's equation***:

$$E = E° + RT\ ln\frac{[ox]}{[red]} \qquad (eq.5)$$

As the voltage changes with electrode composition, the galvanostatic profile reflects the phase diagram of the system. Generally, a continuous variation of the electrode potential with time (and thus composition) is ascribed to a solid solution behaviour involving a single-phase reaction. On the contrary, the presence of a potential plateau means a two-phase system, and therefore an important thermodynamic information.
Moreover, it is possible to measure the quantity of charge Q associated with a redox process. The ratio between the charge involved in reduction reaction and the corresponding oxidation is the Coulombic Efficiency that indicates the degree of reversibility of the redox process. The determination of the amount of charge integrated over time and divided by the mass of the electroactive species give the specific capacity of an intercalation electrode material per weight (mAh/g), expressed by the following equation:

$$Q = \frac{(nF)}{(3600 * M)} \qquad (eq. 6)$$

Where n is the number of electrons transferred per mole of reaction, F is the Faraday's constant and M is the molecular weight of the active specie in kg/mol.
By measuring the evolution of the specific capacity value during repeated cycling it is possible to evaluate the cycling life of a given electrode. Usually the rate at which the battery can be charged or discharged is defined by the C rate where 1C corresponds to a complete discharge/charge in one hour.
In ***Figure 25*** the different types of chronopotentiometric techniques are depicted:

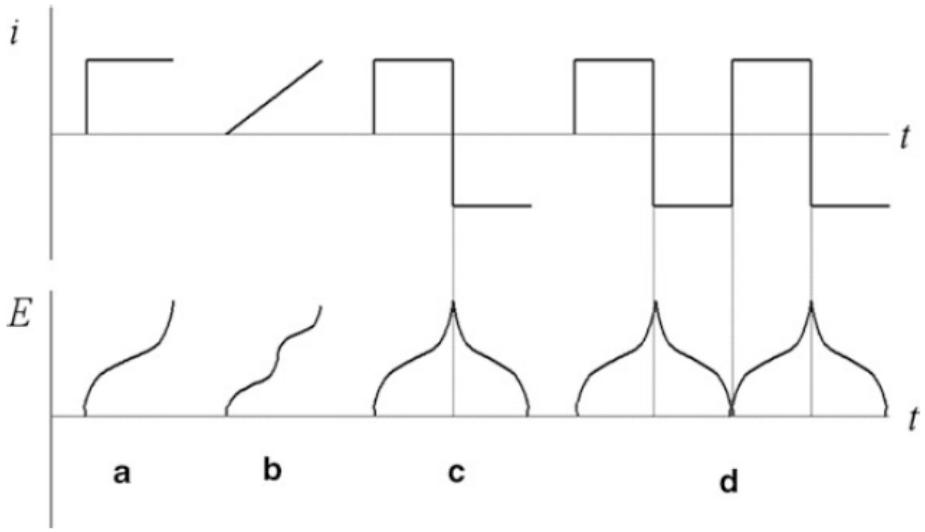

Figure 25: Different types of chronopotentiometries(a) Constant current chronopotentiometry; (b) Chronopotentiometry with linearly rising current; (c) Current reversal chronopotentiometry; (d) Cyclic chronopotentiometry;

In constant current chronopotentiometry, a constant current is applied to the electrode, causing a constant rate oxidation/reduction of the electroactive species. The electrode potential accordingly varies with time as the concentration ratio of reactant to product changes at the electrode surface.

After the concentration of the reactant drops to zero at the electrode surface, the reactant might be insufficiently supplied to the surface to accept all of the electrons being forced by the application of a constant current. The electrode potential will then sharply change to more anodic/cathodic values. The applied current can be varied with time: the current can be linearly increased or decreased (chronopotentiometry with linearly rising current) and can be reversed after some time (current reversal chronopotentiometry). On the other hand, the current is repeatedly reversed in cyclic chronopotentiometry [45].

The ***Differential Analysis of cycles*** allows to observe in detail all the processes occurring during cycling. The resulting profiles exhibit a shape similar to that of CV, but with a lower bias by diffusion limitations. Each peak has a specific shape, position and intensity, indicating a specific process that occurred on the electrode.
The analysis is done by elaborating the data coming from GCPL: the data are used to plot Q vs E for the selected half cycles of charge and discharge, the curves are then interpolated and then differentiated over E to obtain a dQ/De vs E plot.

4. EXPERIMENTAL PART: SYNTHESIS OF BIOMASS-DERIVED HARD CARBONs

4.1 Introduction

The aim of this work is the development of Biomass- derived Hard Carbons as anode materials for LIBs and NIBs batteries.

The biomasses used as raw materials have been chosen because they are very abundant agricultural by-products in Italy. They are:

- Olive leaves;
- Cherry stones;
- Orange peel;
- Olive stones;

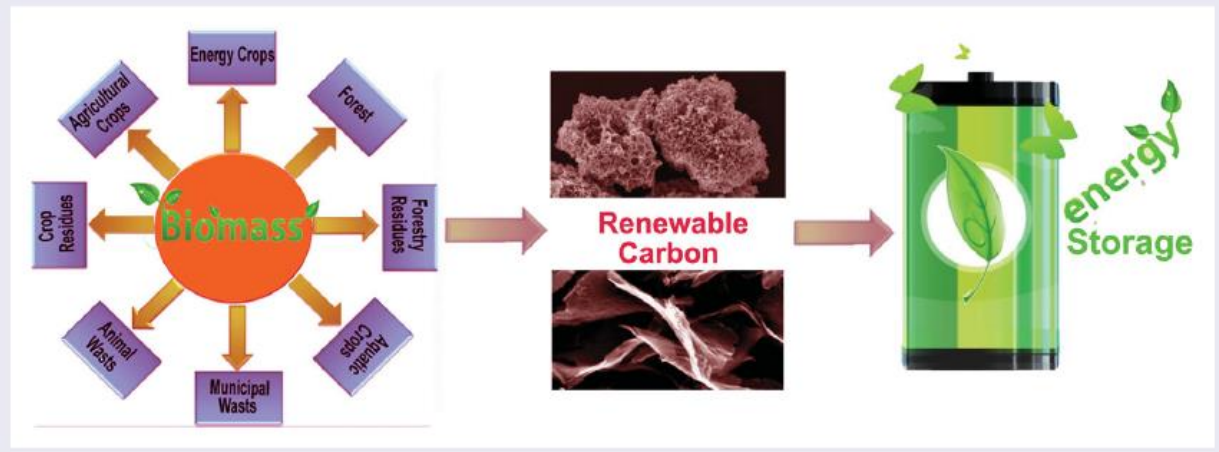

Figure 26: Schematic representation of the main steps of the research;

Each precursor has been submitted to different synthesis procedures, however, all synthesis can be divided into three main parts: pre-treatment, activation and annealing. The pre-treatment has been the same for all samples, except for cherry stones (See Section 4.1.2): crushing and oven-drying at 80°C overnight. The activation has been done by impregnation of the raw materials with chemical agents, such as HCl, KOH and $ZnCl_2$, which can increase the porosity and surface area of lignocellulosic precursor [46] and thus improve the insertion/de-insertion processes in HCs. Finally, the annealing (dry pyrolysis) processes have been performed between 900° and 1000° C, trying to reducing the time at the maximum temperature without producing considerable structural changes on HCs.

4.1.1 Olive Leaves Hard Carbon Synthesis (HCL4)

This synthesis represents a continuation of a work done before and reported in other thesis and focused on the development of olive leaves HC with electrochemical desired properties.

- ***Activation***

3M aqueous solution of HCl have been brought into contact with the dry olive leaves for 2 days. After that, the olive leaves have been filtered and washed with deionized water until neutral pH and then oven-dried at 120° C overnight;

- ***Annealing***

The pyrolysis processes have been carried out in a horizontal cylindrical furnace, using a ceramic container. The system was heated at 10°C/min to a final temperature of 1000°C, under Argon atmosphere, flowing as slowly as possible. In fact, slow flow rates don't allow flushing away the released gas (mostly CO_2) which would react with carbon creating porosity and enhancing the surface area. The isothermal time at maximum temperature has been 6 hours. The sample has been cooled down inside the furnace, under Argon flow as well.

4.1.2 Cherry Stones Hard Carbon Synthesis (HCC)

This synthesis has been developed basing the procedure on M.O Marìn et al. [47] using $ZnCl_2$ as chemical activating agent.

- ***Pre-treatment***

Cherry stones (CS) have been crushed and contacted with dilute H_2SO_4 solution for 1 day (10% v/v in H_2O), in order to dry, hydrolyse the lignocellulose and remove the inorganic components of lignocellulosic materials. After that, the solution has been washed until pH of 6/7 with pure water, filtered and oven-dried at 80° C overnight;

- ***Activation***

100ml of aqueous solution of $ZnCl_2$ (CS:$ZnCl_2$ ratio was 1:4, by weight) has been brought into contact with 25 gr of pre-treated cherry stones under mechanical agitation, at 80°C for 2h. After the impregnation treatment, the solids have been washed and filtered until no Zn^{2+} and Cl^- could not detected. These solids have been oven-dried at 80°C overnight;

- ***Annealing***

The pyrolysis has been carried out heating the system 10°C/min to the final temperature of 900°C, under nitrogen atmosphere. The isothermal time at maximum temperature has been 6 hours. The sample has been cooled down inside the furnace, under nitrogen flow as well;

4.1.3 Orange Peel Hard Carbon Synthesis (HCO)

- ***Activation***

Three methods have been carried out:

1) No activation;

2) Acid activation with a 3M solution of HCl for 1 day (as olive leaves);

3) Alkali activation with a 7% (v/v) aqueous solution of KOH for 1 day;

The samples 2 and 3 have been filtered and washed with deionized water until neutral pH;

- ***Annealing***

Each sample was heated at 10°C/min to a final temperature of 900°C, under Argon atmosphere, flowing as slowly as possible. The isothermal time at maximum temperature was 6 hours. The samples were cooled down inside the furnace, under Argon flow as well;

4.1.4 Olive Stones Hard Carbon Synthesis (HCJ)

- ***Activation***

As orange peel, three methods have been used with the same conditions (See Section 4.1.3);

- ***Annealing***

Each sample was heated at 10°C/min to a final temperature of 900°C, under Argon atmosphere, flowing as slowly as possible. The isothermal time at maximum temperature has been 2 hours. The samples were cooled down inside the furnace, under Argon flow as well;

Table 4 depicts the main differences between the synthesis and the samples names:

Table 4: Schematic overview of synthesis procedures

Precursor	Activation	Annealing	Sample Name
Olive Leaves	HCl	10° C/min to 1000° C for 6h in Ar atmosphere	HCL4
Cherry Stones	$ZnCl_2$	10° C/min to 900° C for 6h in N_2 atmosphere	HCC
Orange Peels	No activation	10° C/min to 900° C for 6h in Ar atmosphere	HCO1
	KOH		HCO2
	HCl		HCO3
Olive Stones	No activation	10° C/min to 900° C for 2h in Ar atmosphere	HCJ1
	KOH		HCJ2
	HCl		HCJ3

5.EXPERIMENTAL PART: RESULTS AND DISCUSSION

5.1 Structural and Morphological Characterization

Morphological, structural and chemical characterization by TGA, Raman Spectroscopy, XRD and SEM have been done on the pristine powders obtained.

5.1.1 Thermogravimetric Analysis

In this work the TGA has been used to examine the physicochemical processes occurring in the HC's precursors, in order to understand the kinetic of the decomposition process of the samples and exploit it to set the most appropriate experimental parameters for the pyrolysis of the raw materials. TGA analysis have been done with NETZSCH STA 2500 Regulus thermogravimetric balance on each raw material in the same experimental conditions:

- Maximum temperature: 1100 °C;
- Ramp of temperature: 10 °C/min;
- Atmosphere: Inert (N_2);

Figure 27 shows the result obtained:

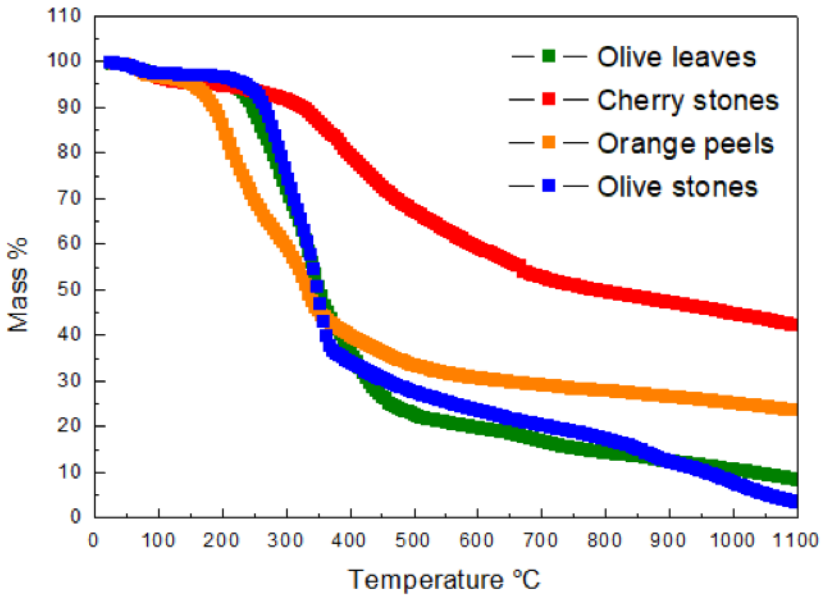

Figure 27: TGA spectra of Olive leaves (green line); Cherry stones (red line); Orange peels (orange line); Olive stones (blue line);

Reaction mechanisms occurring during the pyrolysis are still controversial due to the complexity of the raw materials and number of possible reactions. However, bond cleavage, manifold intramolecular reactions, decarboxylation, decarbonylation, dehydration, demethoxylation, condensation and aromatization are some of characteristics mechanisms [48]. The maximum temperature reached during the pyrolytic processes has a critical influence on the reactions occurring and on the properties of the product [49]. Instead, the heating rate influences the product distribution: slower processes lead to high yields of solids and gases products, faster processes mainly lead to liquid products.

The TGA analyses show three distinct zones of weight loss for each precursor, meaning that decomposition processes are occurring. The first zone, between 65 °C and 130 °C, is due to the evaporation of moisture. The weight losses are small (see ***Table 5***) because the samples have been oven-dried before the analysis. In second zone, between 180 °C and 500 °C, there are the main weight losses probably due to the gradual decomposition of lignocellulosic materials: hemicellulose mainly decomposes 200 and 400 °C, while cellulose decomposes at higher temperatures (300-400 °C); by contrast, lignin is the most stable component since it decomposes gradually between 180-600 °C [50]. The small weight loss of cherry stones, compared to the other ones, is probably due to the presence of $ZnCl_2$ residuals in the sample. The zone 3 (550-1100 °C) corresponds to the complete volatilization of biomasses, especially the lignin: in fact, the higher weight losses are for cherry and olive stones which have high content of lignin (30.7% [51] and 40% [52], respectively), and in the case of cherry stones, also to the volatilization of $ZnCl_2$ (b.p.=732 °C).

Table 5 depicts the weight losses in the different zones for each precursor:

Table 5: Weight losses percentage for each precursor;

Precursor	Weight loss Zone 1 (60-130 °C)	Weight loss Zone 2 (180-500 °C)	Weight loss Zone 3 (550-1100 °C)
Olive Leaves	2.17 %	73.27 %	12.63 %
Cherry Stones	3.38 %	27.75 %	20.80 %
Orange Peels	2.86 %	58.02 %	8.19 %
Olive Pits	0.89 %	69.31 %	21.83 %

5.1.2 Raman Spectroscopy Characterization

The structure of HCs has been investigated by Raman Spectroscopy, since it is a standard tool for the characterization of amorphous carbons.

The Raman spectra of disordered carbons show two quite sharp modes, the ***G peak*** around 1580-1600 cm^{-1} and the ***D peak*** around 1350 cm^{-1}, with different intensities, position and width. The G mode has E_{2G} symmetry and its eigenvector shown in ***Figure 28a*** involves the in-plane bond-stretching motion of pairs of C sp^2 atoms. It is important to note that this mode does not require the presence of six-fold rings, but it occurs at all sp^2 sites. The D peak is a breathing mode of A_{1g} symmetry shown in ***Figure 28b*** and it is forbidden in perfect graphite and only because active in the presence of disorder. Moreover, amorphous carbons show a small modulated bump from ~ 2400 to 3100 cm^{-1} [53].

Concerning the interpretation of spectra, very important is the ***I(D)/I(G) ratio*** (where I is the intensity of the peak) that decreases with increasing amorphization. Furthermore, high intensity of D peak means ordering, instead G peak retains the same intensity of graphite since it is related to the stretching of sp^2 carbons [53].

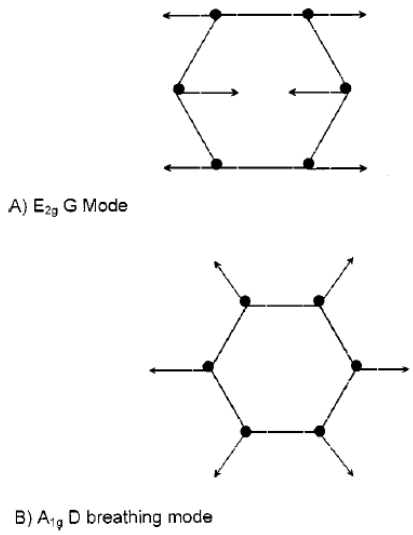

Figure 28: Carbon motions in the (a) G and (b) D modes;

Raman spectra have been recorded using HORIBA IHR 320 spectrometer with the following experimental settings:

- Laser's wavelength: 532 nm;
- Range: 10-3600 cm^{-1};
- Acquisition time: 30s;

Figure 29a-b-c-d shows the Raman spectra of HCs and in ***Table 6*** are listed the I(D)/I(G) ratios and the position of the D and G peaks:

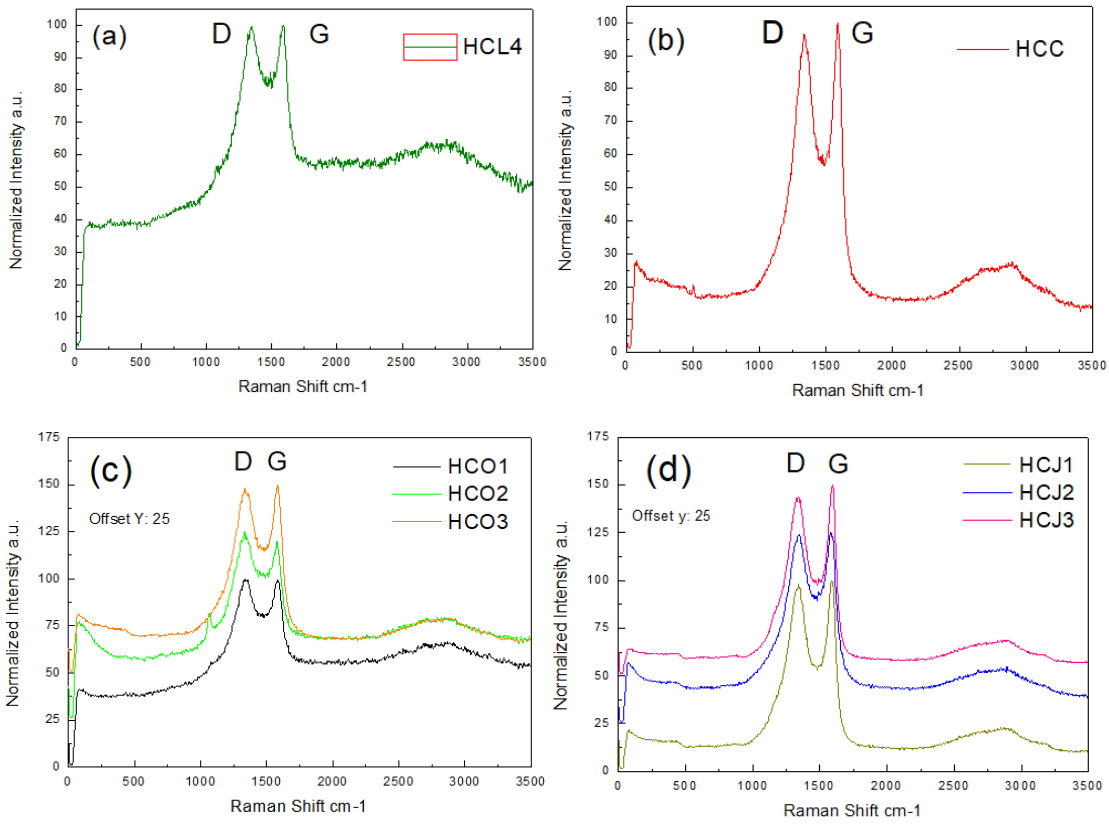

Figure 29: Raman spectra of (a) HCL4; (b) HCC; (c) HCO1-2-3; (d) HCJ1-2-3;

Table 6: I(D)/I(G) ratios and positions of D and G peaks for each sample;

Sample Name	Position of D peak cm^{-1}	Position of G peak cm^{-1}	I(D)/I(G)
HCL4	1350.28	1593.39	0.996738
HCC	1334.93	1589.63	0.966282
HCO1	1337.13	1580.52	1.004488
HCO2	1329.40	1573.03	1.055015
HCO3	1333.27	1584.27	0.981397
HCJ1	1341.03	1588.04	0.980737
HCJ2	1348.74	1576.81	0.987611
HCJ3	1337.16	1595.52	0.938456

The I(D)/I(G) ratios are close to 1 and slightly exceed it in the case of HCO1 and HCO2, meaning a little greater number of defects in these two samples. HCJ3 has the lowest I(D)/I(G) ratio and seems to be the most amorphous carbon. The position of D peaks (~1340 cm^{-1}) and G peaks (~1580 cm^{-1}) of all samples are similar to the ones reported in other studies [52,54] and confirms the disordered morphology and low graphitization degree of the HCs.

5.1.3 X-Ray Diffraction Characterization

Further structural characterizations have been done using X-ray diffraction. HCs usually exhibit two broad diffraction peaks at ~24° and ~43° corresponding to (002) and (100) reflections, that are characteristics of low degree of graphitization [52].

XRD spectra have been recorded with Philips PW 1730/10 the following experimental settings:

- 2θ range of analysis: 3-70°;
- Acquisition 2θ range: 0.020°;

Figure 30a-b-c-d-e-f-g-h shows the XRD spectra of HCs: all the samples show the characteristic peaks of amorphous carbons, except for HCL4 and HCO2, meaning that the pyrolysis had occurred. In particular, HCL4 presents the reflexions (001), (100), (101), (102), (110), (111) and (201) which are ascribed to $Ca(OH)_2$, instead the other peaks may be related to $Mg_2PO_4(OH)*3H_20$. However, the ratio between amorphous and crystalline phase is uncertain. As well as HCL4, HCO2 presents two phases, one more crystalline and the other one more amorphous: the crystalline phase can be related to iron and manganese hydroxide phosphate, instead the other phase is uncertain. Thus, due to the high number of unknown peaks, HCO2 requires a preliminary EPMA analysis.

Finally, all the samples except HCJ1 and HCJ2 show the characteristics peaks of brass, with which is made the sample holder, since HC have low density a therefore the X-rays pass through the sample, hitting the sample holder.

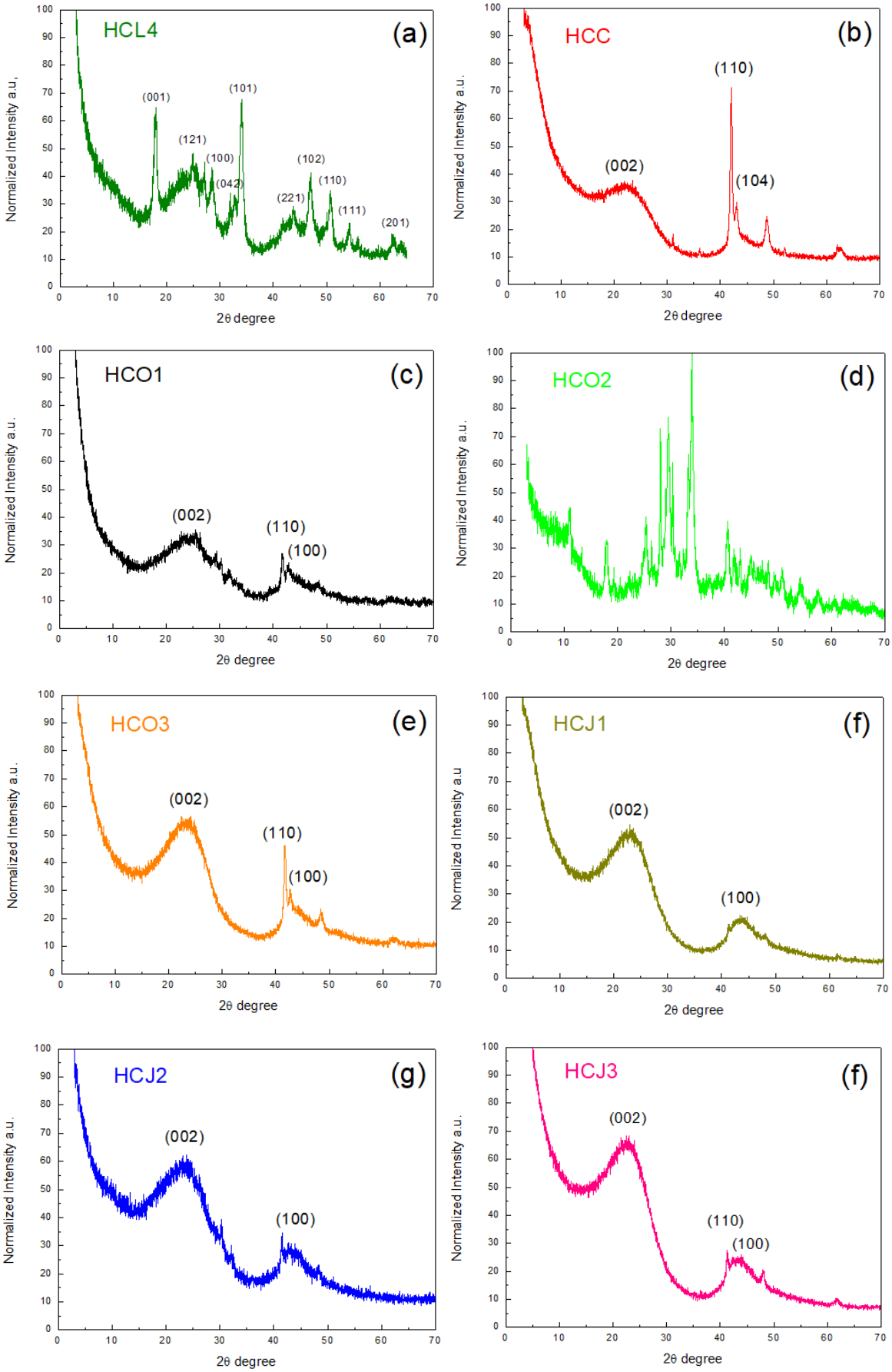

Figure 30: (a) HCL4; (b) HCC; (c) HCO1; (d) HCO2; (e) HCO3; (f) HCJ1; (g) HCJ2; (h) HCJ3 XRD spectra;

5.1.4 Scanning Electron Microscopy Characterization

SEM has been used in imaging mode to characterize the morphological behaviours of HCs and try to correlate them to the electrochemical performances provided, and in EPMA mode to find which elements are present in the final HCs. However, the most promising samples as anodes for sodium batteries underwent SEM analysis.

It is worth to noting that the surface of hard carbons typically contains numerous chemical complexes, formed during the pyrolysis process (typically chemisorbed oxygen containing species) which exhibit different thermal stabilities and are desorbed at different temperatures. Carbon-hydrogen bonds can also be present, especially if pyrolyzed at temperatures below 1000°C [58]. Surface oxide groups on carbon play a major role in its surface properties, including wettability, which is the reason why the physical-chemical properties of carbonaceous materials can be tuned by post-synthesis treatments.

SEM analysis have been done using SEM Zeiss Sigma 300 as instrument with the following experimental settings:

- Electron High Tension: 10-15 kV;
- Magnification: 10000x;
- Width Distance: 8.0 mm;
- Scale: 10 µm;

Figure 31a-b shows the surface images of HCC and HCO3, respectively.

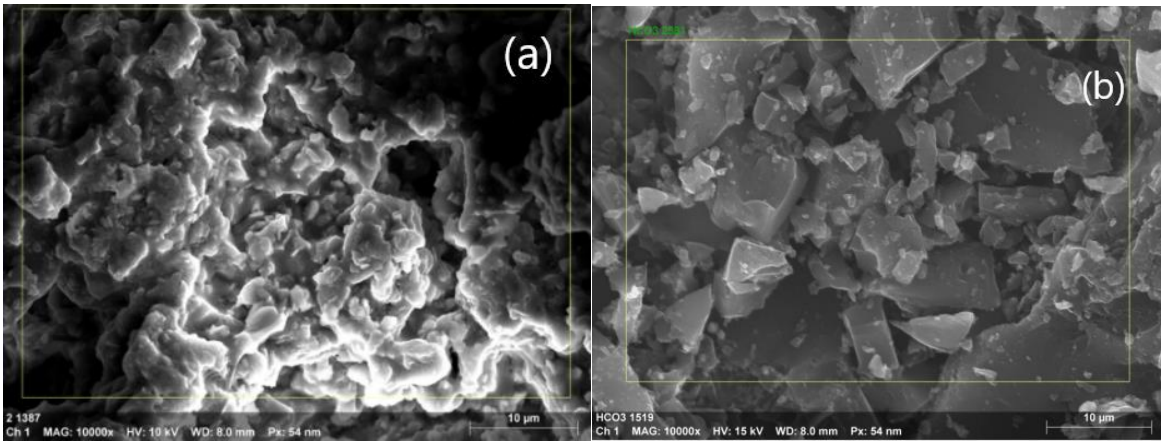

Figure 31: SEM images of (a) HCC; (b) HCO3;

Instead, ***Table 7*** shows the results of EPMA analysis of HCO3:

Table 7: Elemental composition of HCO3

Element	At. No.	Netto	Mass [%]	Mass Norm. [%]	Atom [%]	abs. error [%] (1 sigma)	rel. error [%] (1 sigma)
Carbon	6	302526	96.53	96.53	97.37	10.38	10.75
Oxygen	8	2698	3.47	3.47	2.63	0.64	18.42
		Sum	**100.00**	**100.00**	**100.00**		

Both size and distribution of pores determine the electrochemical properties of Hard Carbons, especially in NIBs. Impregnation with $ZnCl_2$, in the case of cherry stones, causes degradation of the cellulosic material and, during annealing, dehydration. These processes result in pyrolysis and aromatization of the carbon skeleton and creation of pore structure [47]. Instead impregnation with HCl, in the case of orange peels, accelerate the cleavage of bonds between biopolymers (principally cellulose and lignin) facilitating the amorphization of raw material during pyrolysis and the formation of cavities.

The SEM images show that HCC is more homogeneous respect to HCO3. Anyway, this can be attributed to a bad milling of HCO3's powder. Nevertheless, HCO3 exhibit a flake morphology. By other hand, the elemental composition on HCO3 shows that no trace of HCl have been found in the final product. Instead, the EPMA of HCC have not been performed since preliminary qualitative analysis of Zn^{2+} and Cl^- in the samples had negative result. However, qualitative analysis is not reliable and therefore the main problem of use $ZnCl_2$ as chemical activating agents may be the possible contamination of the sample with zinc compounds since zinc is probably still present in the obtained Hard Carbon.

5.2 Electrochemical Characterization

Electrochemical characterization of all materials by CV and GCPL have been done on Hard Carbon-based electrodes prepared with different binders, PVdF and Na-CMC, to test as anodes in LIBs and NIBs.

5.2.1 Electrode Preparation and Cell Assembly

Tables 8a-b shows the composition of electrodes prepared for the electrochemical characterization:

Table 8: Electrode formulation with (a) Na-CMC and (b) PVdF as binder

Electrode Composition	Percentage Formulation
Active Material	85
Super C65	10
Binder (Na-CMC)	5

Electrode Composition	Percentage Formulation
Active Material	80
Super C65	10
Binder (PVdF)	10

Hard Carbons have been used as active material, Carbon Super C65 as conductive agent and two different binders, Na-CMC and PVdF, with different formulation since the CMC is a stronger binder than PVdF.

About the preparation, it has been performed in the same way except for the solvent used to dissolve the binder: Na-CMC has been dissolved in ultrapure water, instead PVdF in N-methyl-Pyrrolidone. The

binder has been left dissolving by magnetic stirring and in the meanwhile the conductive agent and the active material has been mixed and grinded until a homogeneous powder was obtained. Then the powder has been slowly added to the binder solution and let stirring at least 6 hours in order to obtain a uniform slurry. After the stirring, the slurry has been casted with Doctor Blade technique with a thickness of 150 µm on a copper foil for LIBs and aluminium foil for NIBs, respectively. It has been dried at room temperature overnight, pressed with a roll press to uniform the thickness and enhance the adhesion of the slurry to the foil. Finally, 9mm circular electrodes have been cut, weighted and dried overnight at 120°C under vacuum in order to remove water and oxygen trace.
For the electrochemical characterization three electrodes cells T-shaped have been used. They are made of polypropylene and they are equipped with stainless steel current collectors.

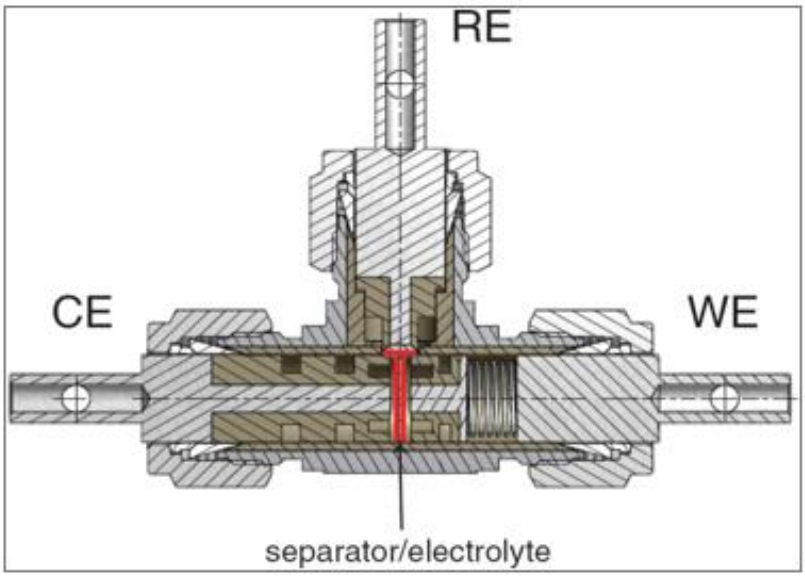

Figure 32: T-shaped cell section;

The cell, as shown in ***Figure 32***, is composed by a Reference Electrode (RE) and a Counter Electrode (CE) both made of metallic lithium, and the Working Electrode (WE) that is the one under examination. The potential is measured between the Reference and the Working Electrodes, instead the current is applied between the Counter and the Working Electrodes. A circular Whatman GF/A fiberglass disks has been used as separator in order to prevent the contact between the electrodes but it is permeable to the electrolyte.
The electrolytes used are different for LIBs and NIBs batteries and they are, respectively:

- $LiPF_6$ in EC:DMC 1:1 (w/w) for lithium;
- $NaClO_4$ in EC:PC 1:1 (w/w) for sodium;

The cells have been assembled in argon atmosphere in the glove box. The electrochemical measurements have been carried out using a galvanostat/potentiostat VMP2/Z Bio-Logic.

5.2.2 Cyclic Voltammetry

A CV protocol was performed for each sample in both lithium and sodium cells to characterize and compare the redox processes occurring during cycling. The scan rate used has been 0. 1 mV/s and the potential range was between 0.02 < E_{we} < 3.00 vs Li and Na respectively. CV scans have been done with a galvanostat/potentiostat VMP2/Z Bio-Logic.

- **Li-Ion Cells**

Figure 33a-b-c-d-e-f-g-h shows cyclic voltammograms of lithium-ion cells. Large irreversible capacity losses are observed between the CV scans of first and second cycles, which can be mostly related to the SEI formation. In the first cycle, a small reduction peak around 1.0V can be related to the irreversible reaction between the electrolyte and the hard carbon surface functional groups [55]. Instead, the plateau at around 0.5V is mostly due to the formation of SEI. Moreover, two additional steps have been found in CV scans: sloping potential region extending to ~0.2V and a low potential plateau. The first has been assigned to the insertion of Li^+ ions between the layers, with the turbostratic disorder producing sites with a distribution of chemical environments which results in a sloping profile while the second is related to the adsorption of ions in the micropores.

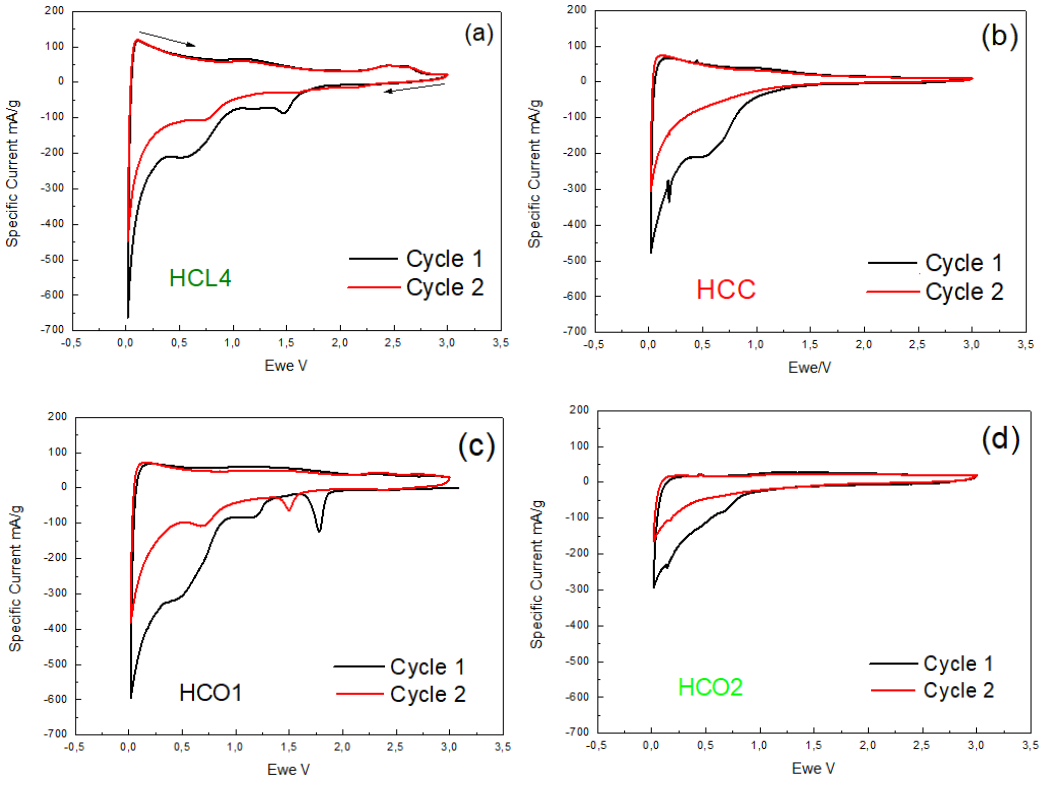

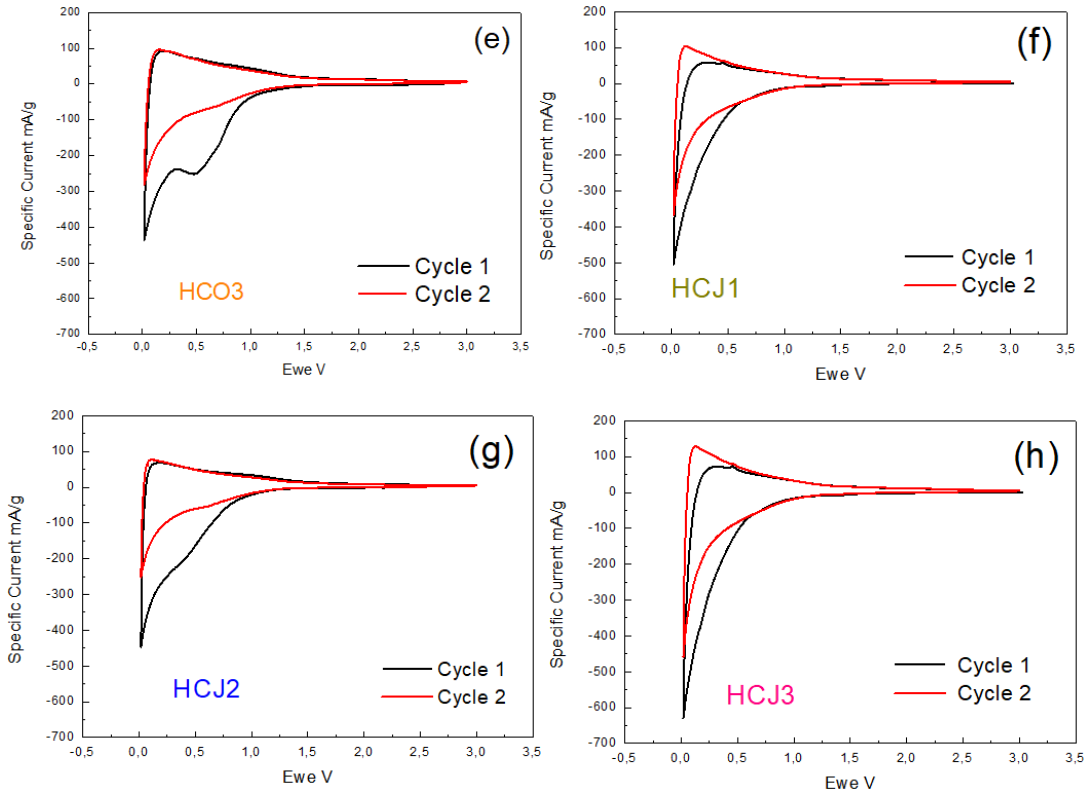

Figure 33: (a) HCL4; (b) HCC; (c) HCO1; (d) HCO2; (e) HCO3; (f) HCJ; (g) HCJ2 and (h) HCJ3 CV scans vs Li^+/Li;

- **Na-Ion Cells**

The mechanisms for lithium and sodium insertion have been found to be similar [56,57]. Therefore, CV scans (***Figure 34a-b-c-d-e-f-g-h***) on sodium cells shows a considerable decrease of capacity between first and second cycle due to the formation of the passivation layer, occurring between 1.0 and 0.5V, since the plateau disappear in the second cycle. As well as lithium, the sloping region below 0.5V corresponds to the insertion of sodium into graphene sheets, instead the low potential plateau close to 0.02V corresponds to the insertion of the Na^+ into the nanopores of HCs. However, the low potential plateau is not very clear as in S. Komaba et al. [37] studies, since the scan rate used is too fast to see the detailed processes and the peaks appear overlapped. Instead, the abrupt oxidation peak at around 0.2V, probably means that the HCs underwent reversible de-insertion of sodium, confirmed by the continuously loss of capacities during discharge-charge cycling of cells.

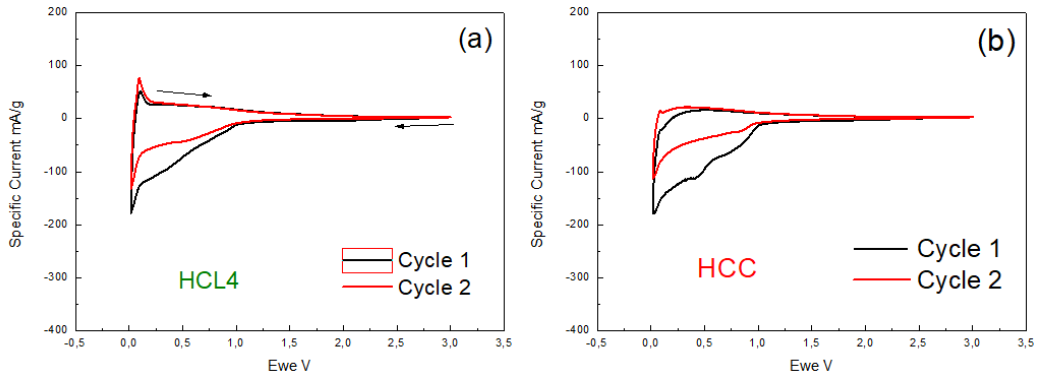

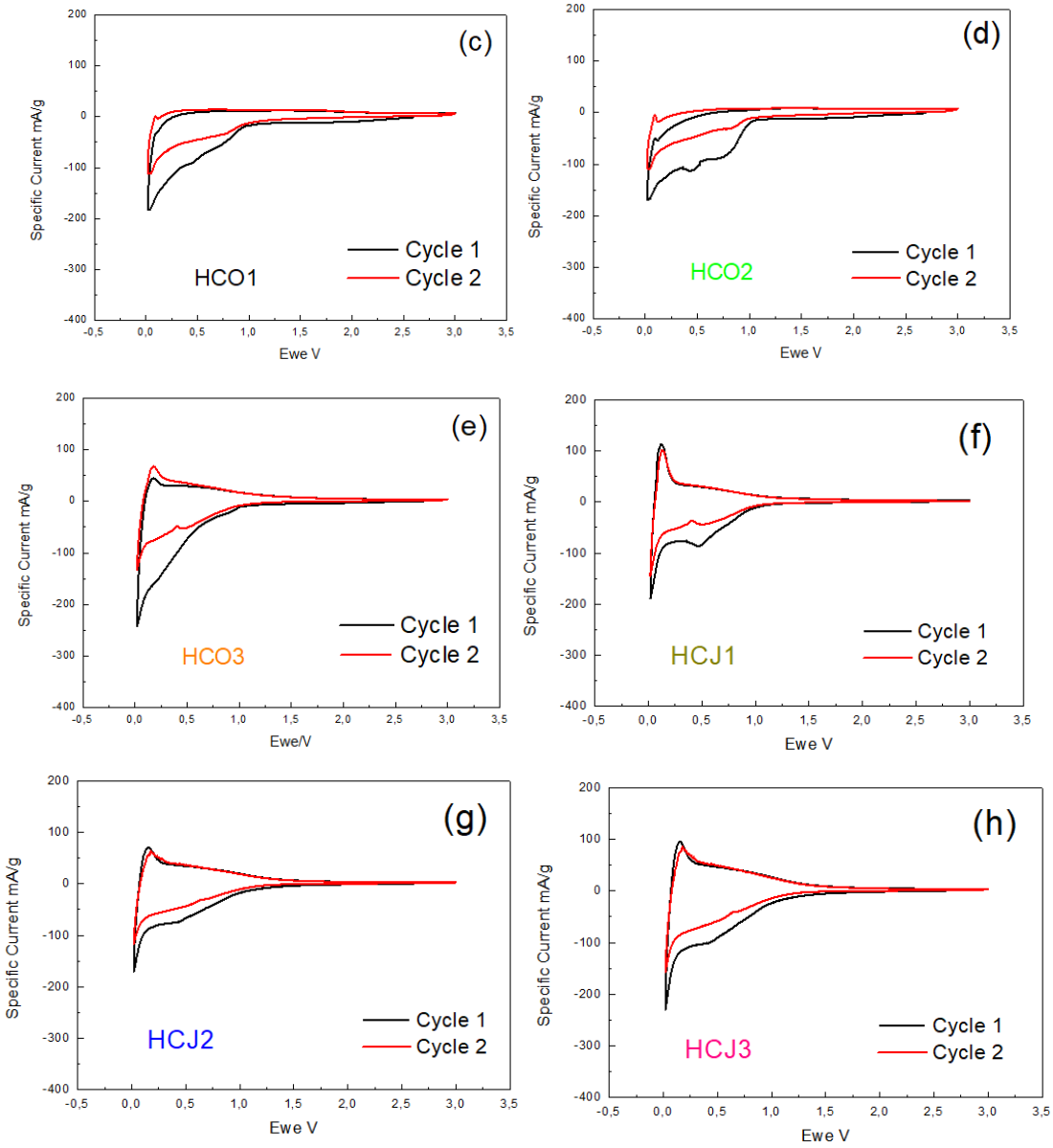

Figure 34: (a) HCL4; (b) HCC; (c) HCO1; (d) HCO2; (e) HCO3; (f) HCJ1; (g) HCJ2; (h) HCJ3 CV scans vs Na^+/Na;

5.2.2 Galvanostatic Cycling with Potential Limitation (GCPL)

Long-term galvanostatic cycling experiments were carried out with a galvanostat/potentiostat VMP2/Z Bio-Logic in order to evaluate the specific capacity, stability and efficiency of the materials as anodes in sodium and lithium cells. The theoretical capacity was arbitrarily set as 300 mAh/g and normalized according to the weight of the electrode active material.

Cycling studies at two different potential ranges (0.02< Ewe < 2.00 V and 0.02< Ewe < 3.00 V) and with different binders (PVdF and CMC) have been performed in order to try to optimize the performance and cycle life of the cells.

- **HCL4**

The HCL4 electrodes have been prepared using only CMC as binder, since previous experiments exhibited better electrochemical performances than with PVdF.

- **Li-Ion Cells**

Sample Name	Total Weight mg	Net Weight mg	Active Material mg	Loading mg/cm^2	Potential Range V
HCL4_CMC_Cu#2	7.01	1.57	1.33	2.09	0.02<Ewe<3.00
HCL4_CMC_Cu#10	6.48	0.84	0.71	1.12	0.02<Ewe<3.00
HCL4_CMC_Cu#1	7.21	1.37	1.16	1.82	0.02<Ewe<2.00

Figure 35a-b-c shows considerable irreversible 1st-cycle capacities (242,368 and 317 mAh/g, respectively) due to the formation of SEI on electrode surface. Nevertheless, the specific capacities are quite high (around 200 and 300 mAh/g) for more than 350 cycles, as well as coulombic efficiency, meaning a high degree of reversibility of lithium insertion/de-insertion process.

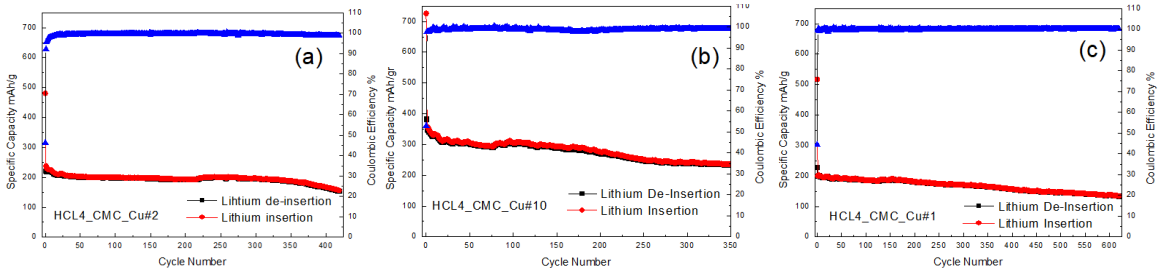

Figure 35a-b-c: Li/HCL4 cells electrochemical performances;

The impact of different potential range toward cycling abilities in LIBs is shown in ***Figure 36***: the greater potential window allows to higher capacity, instead the smaller potential range corresponds to a smaller specific capacity. However, smaller potential window corresponds to an increase of cycling stability due to the reduced polarization of the electrode that may destroy the passivation layer.

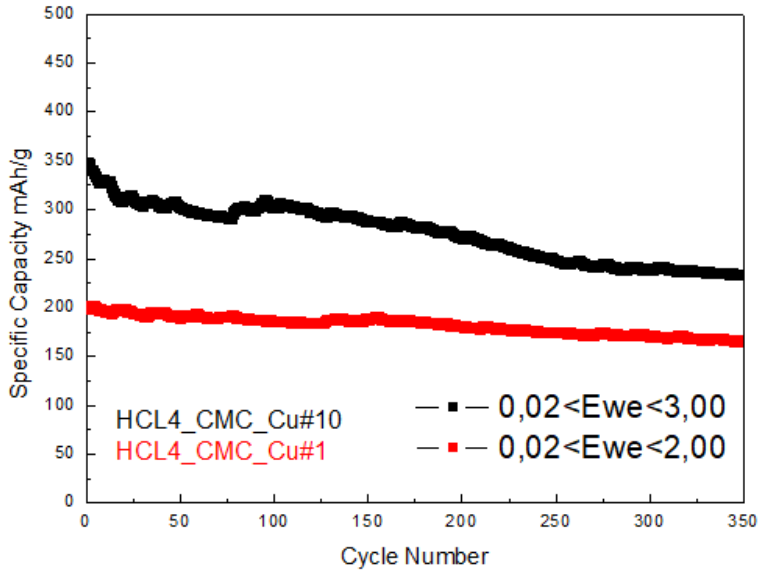

Figure 36: Potential window comparison in HCL4-Li cells;

- **Na-Ion Cells**

Sample Name	Total Weight mg	Net Weight mg	Active Material mg	Loading mg/cm^2	Potential Range V
HCL4_CMC_Al#1	5.31	1.71	1.45	2.27	0.02<Ewe<3.00
HCL4_CMC_Al#4	5.69	1.77	1.50	2.35	0.02<Ewe<2.00

As well as lithium cells, sodium cells (***Figure 37a-b***) show a significative amount of irreversible capacity (113 mAh/g and 56 mAh/g) mostly related to the formation of the SEI though the possibility of some ions being trapped in the material cannot be disregarded [58]. In the subsequent cycles, the large irreversible capacity losses disappear quickly and the coulombic efficiencies increase fast to ~99% for more than 500 cycles.

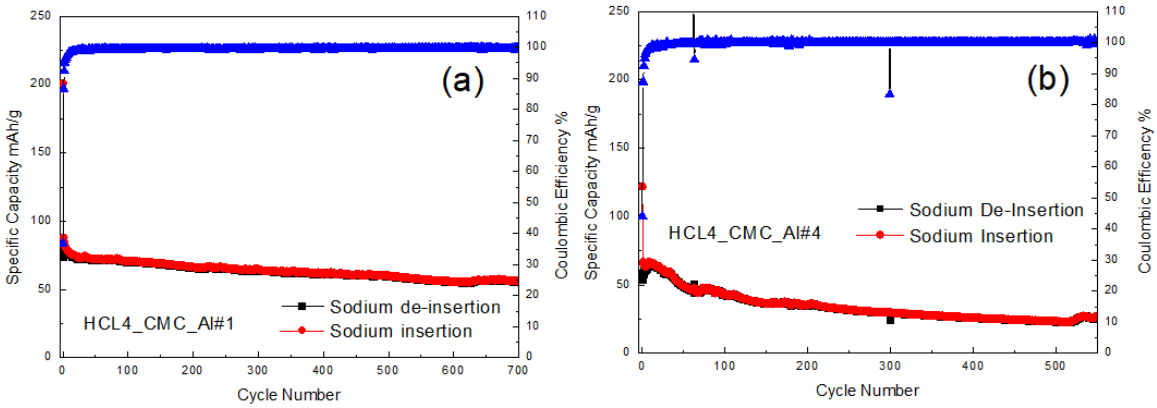

Figure 37a-b: Na-cell irreversible capacity loss in the first cycle;

The potential window has been evaluated also in sodium cell (***Figure 38***). The situation is slightly different from lithium: the higher potential range provides both higher charge specific capacity and higher stability.

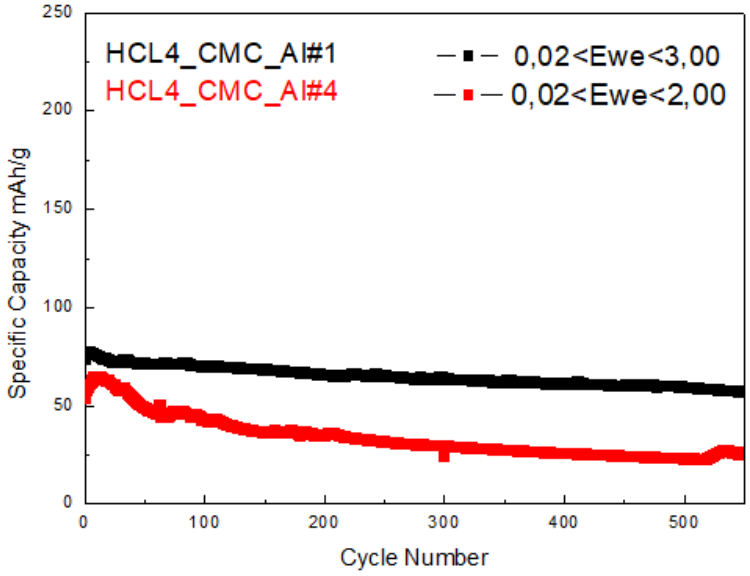

Figure 38: Comparison of potential ranges in Na-cells;

- **HCC**

HCC electrodes have been prepared with both binder and tested in both potential ranges.

- **Li-Ion Cells**

Sample Name	Total Weight mg	Net Weight mg	Active Material mg	Loading mg/cm^2	Potential Range V
HCC_PVdF_Cu#3	6.42	0.94	0.72	1.13	0.02<Ewe<2.00
HCC_PVdF_Cu#4	6.79	1.31	1.05	1.65	0.02<Ewe<3.00
HCC_PVdF_Cu#7	6.69	1.21	0.97	1.52	0.02<Ewe<3.00
HCC_PVdF_Cu#8	6.73	1.25	1.00	1.57	0.02<Ewe<2.00
HCC_CMC_Cu#3	7.60	1.89	1.60	2.52	0.02<Ewe<3.00

Although the small specific capacities of HCC-Li cells, HCC shows long-cycling behaviours with good stability and coulombic efficiency (***Figure 39a-b***).

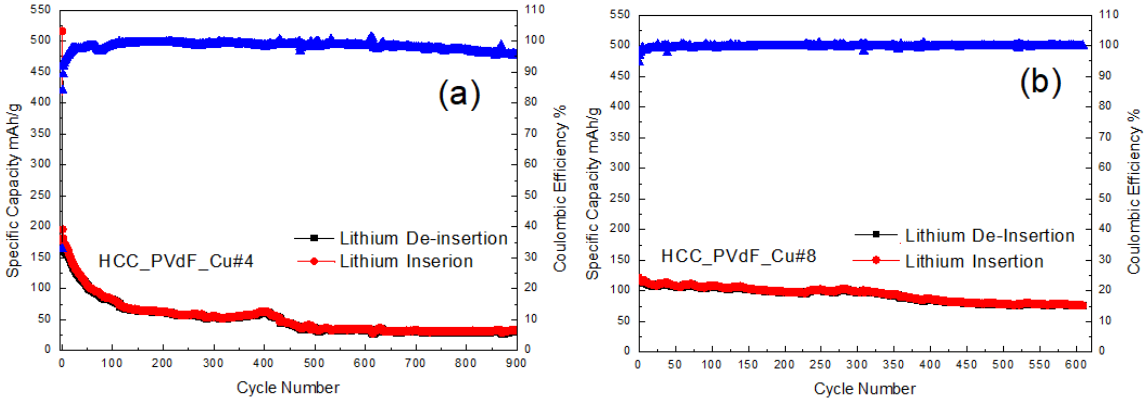

Figure 39a-b: HCC performance in Li-cells;

As well as in HCL4, higher potential window confirms to be better than 0.02<Ewe<2.00 (***Figure 40***). Therefore, the subsequent experiments have been run only between 0.02<E_{we}<3.00 to reduce the number of variables.

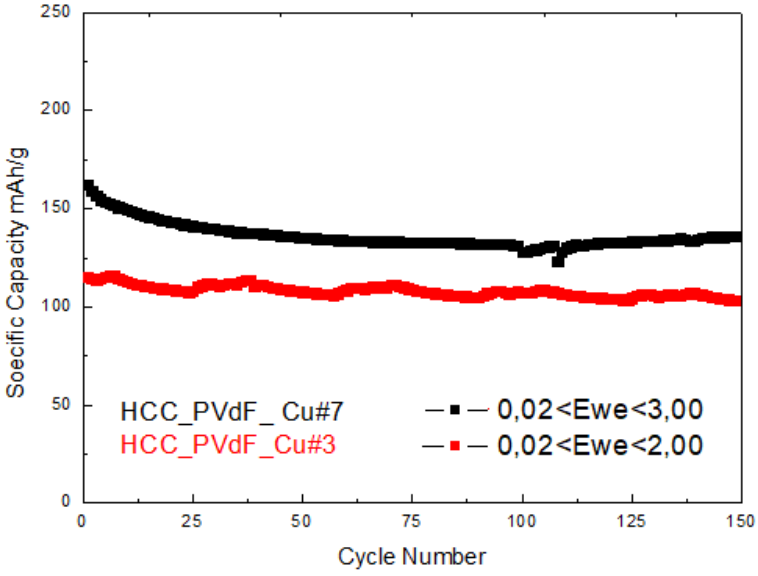

Figure 40: Comparison of potential window in HCC samples;

Figure 41 shows the comparison between CMC- and PVdF- based electrodes: the first provides higher specific capacity than PVdF, however it had a short circuit after 50 cycles. Further evaluation should be done.

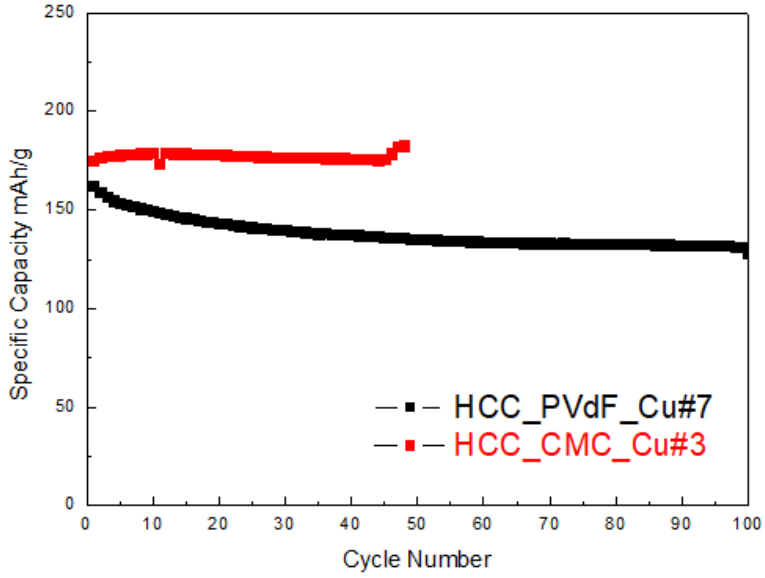

Figure 41: Binder comparison in HCC;

- **Na-Ion Cells**

Sample Name	Total Weight mg	Net Weight mg	Active Material mg	Loading mg/cm^2	Potential Range V
HCC_PVdF_Al#4	5.34	1.74	1.39	2.18	0.02<Ewe<3.00
HCC_CMC_Al#3	5.78	2.18	1.85	2.90	0.02<Ewe<3.00

Figure 42a-b shows higher irreversible capacities (203 and 161 mAh/g, respectively) and better specific capacities during cycling respect to HCL4. PVdF-based electrode exhibit now similar performance compared to CMC-based one (***Figure 43***).

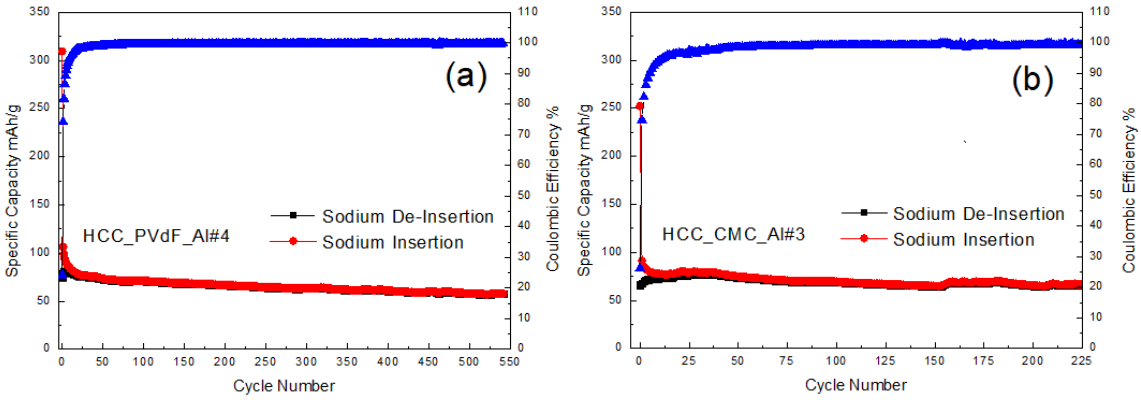

Figure 42a-b: Electrochemical performances of HCC;

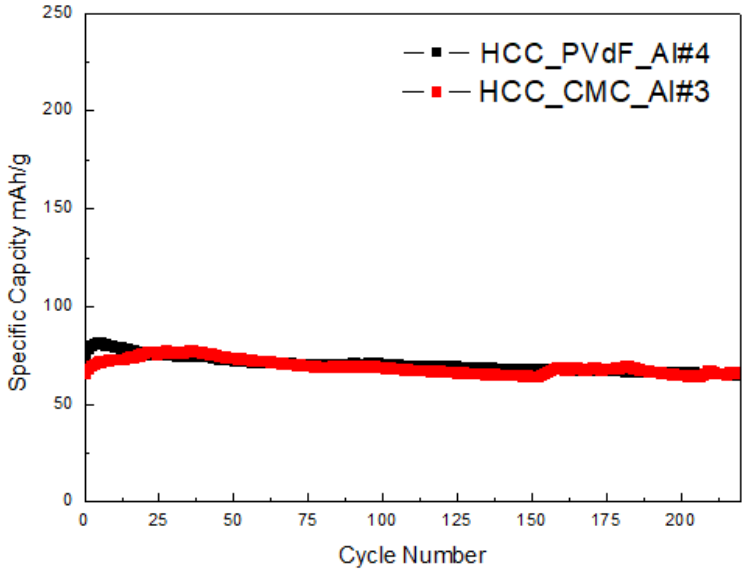

Figure 43: Binder comparison in HCC/Na-cells;

- **HCO1**

Orange peels Hard Carbon (HCO1, HCO2 and HCO3) have been tested only in the optimized potential window ($0.02<E_{we}<3.00$) both with PVdF and CMC binders.

- **Li-Ion Cells**

Sample Name	Total Weight mg	Net Weight mg	Active Material mg	Loading mg/cm^2	Potential Range V
HCO1_PVdF_Cu#8	7.28	1.53	1.22	1.91	0.02<Ewe<3.00
HCO1_CMC_Cu#2	7.95	2.27	1.92	3.02	0.02<Ewe<3.00

The irreversible capacities in HCO1 samples are very high compared to the other HC (~408 mAh/g for CMC and ~ 644 mAh/g for PVdF). Early results correlate this trend also to a poor electrode surface area accessible for the electrolyte [59]. Nevertheless, the specific capacities are between 150 and 200 mAh/g with high coulombic efficiency for more than 250 cycles for both binders (***Figure 44a-b-c***).

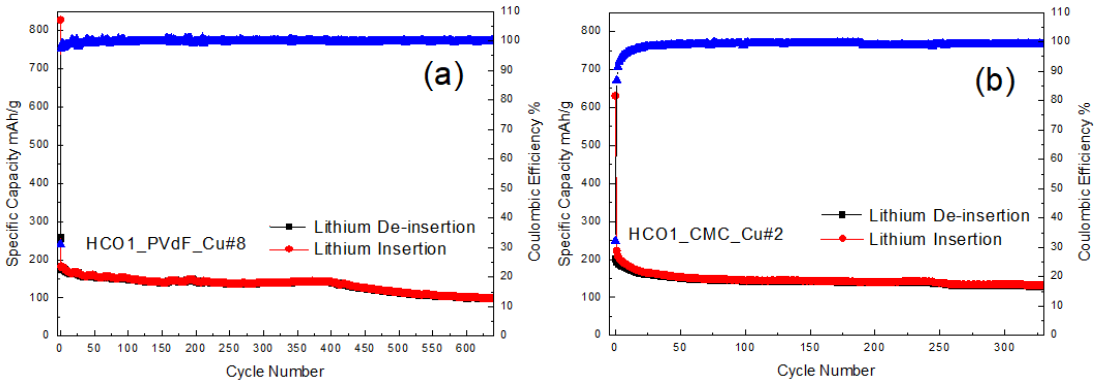

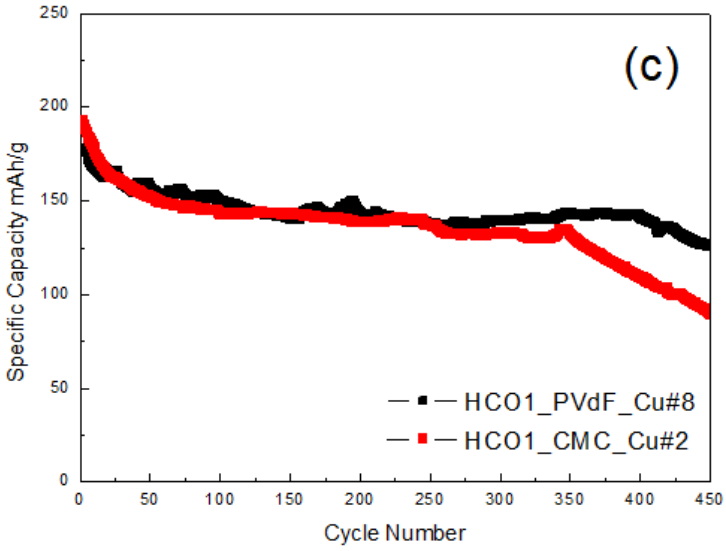

Figure 44a-b-c: (a-b) Electrochemical performances and (c) binders comparison in HCO1/Li-cell;

- **Na-Ion Cells**

Sample Name	Total Weight mg	Net Weight mg	Active Material mg	Loading mg/cm^2	Potential Range V
HCO1_PVdF_Al#2	4.93	1.33	1.06	1.66	0.02<Ewe<3.00
HCO1_CMC_Al#4	7.81	4.21	3.58	3.04	0.02<Ewe<3.00

Also, in sodium cells the irreversible capacities are high and PVdF-based electrode shows slight better electrochemical performances (***Figure 45a-b-c***) than CMC-base one. However, in both cases the specific capacity is low compared to other HC. These performances reflect the poor amorphous phase of HCO1 visible in its XRD spectrum.

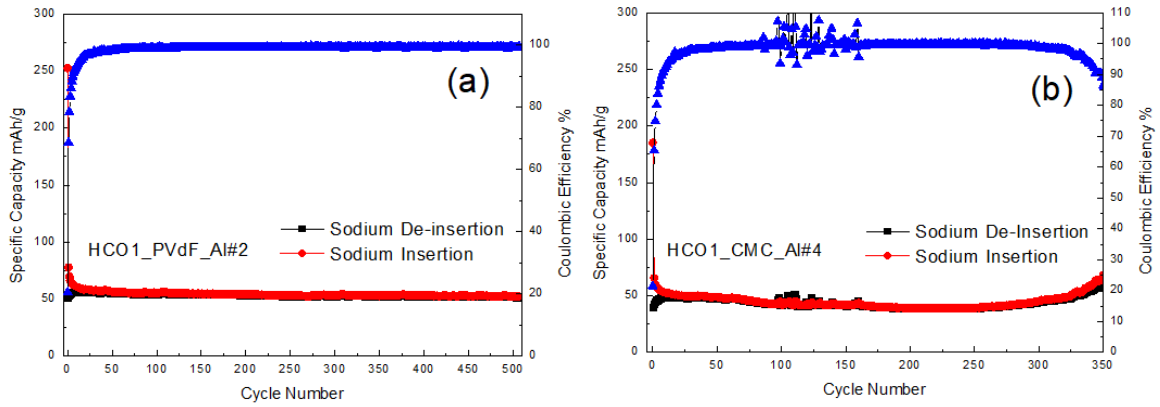

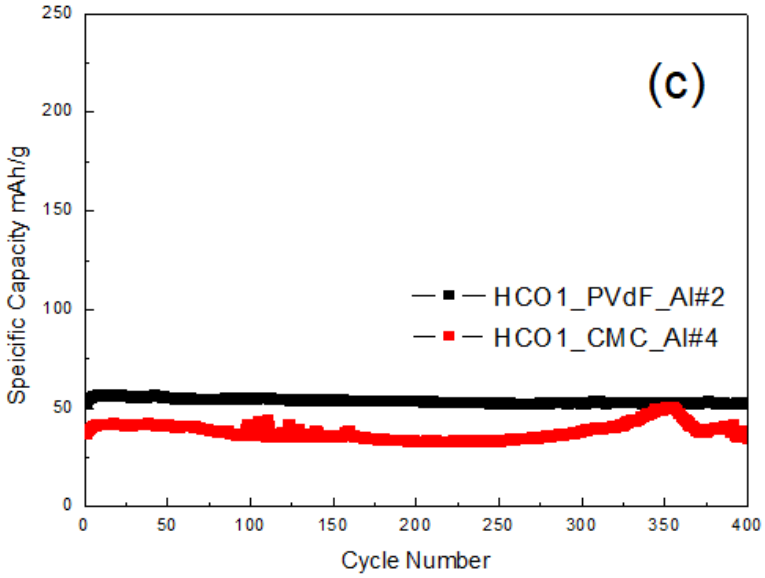

Figure 45: (a-b) Electrochemical performances and (c) binder comparison in HCO1/Na-cell;

- **HCO2**
- **Li-Ion Cells**

Sample Name	Total Weight mg	Net Weight mg	Active Material mg	Loading mg/cm^2	Potential Range V
HCO2_PVdF_Cu#4	8.31	2.67	2.13	3.34	0.02<Ewe<3.00
HCO2_CMC_Cu#10	7.60	1.96	1.67	2.62	0.02<Ewe<3.00

From structural characterizations, HCO2 seems to be the less promising HC as anode materials. GCPL confirms this preliminary evaluation since the specific capacities are around 100 mAh/g for PVdF based electrode and between 150 and 100 mAh/g for CMC-based one (***Figure 46a-b-c***).

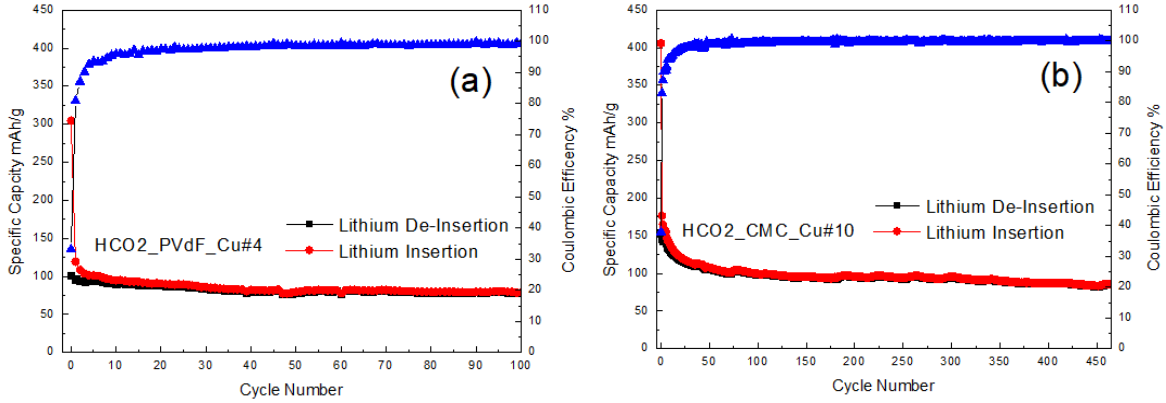

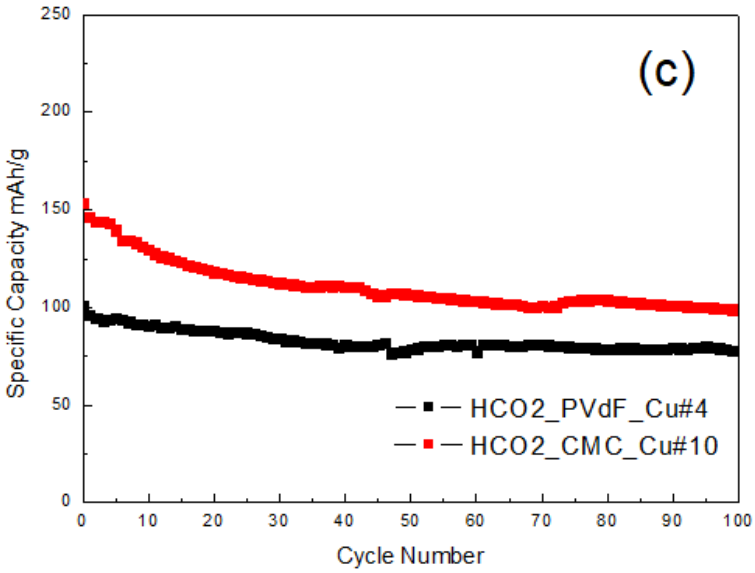

Figure 46: (a-b) HCO2 GCPL and (c) binder comparison in Li-cells;

- **Na-Ion Cells**

Sample Name	Total Weight mg	Net Weight mg	Active Material mg	Loading mg/cm²	Potential Range V
HCO2_PVdF_Al#7	4.70	1.10	0.88	1.38	0.02<Ewe<3.00
HCO2_CMC_Al#10	5.67	1.97	1.67	2.62	0.02<Ewe<3.00

Also, in sodium cells HCO2 performances are not great, both in PVdF and CMC (***Figure 47a-b-c***). Even if KOH is one of the most popular activating agents due to its lower activation temperature and high yield, it requires temperatures of at least 450° C to increase the specific surface area and obtain a well-defined pore size distribution [2]: in this case, the activation has been developed at room temperature and therefore KOH had not affected the properties of HCO2.

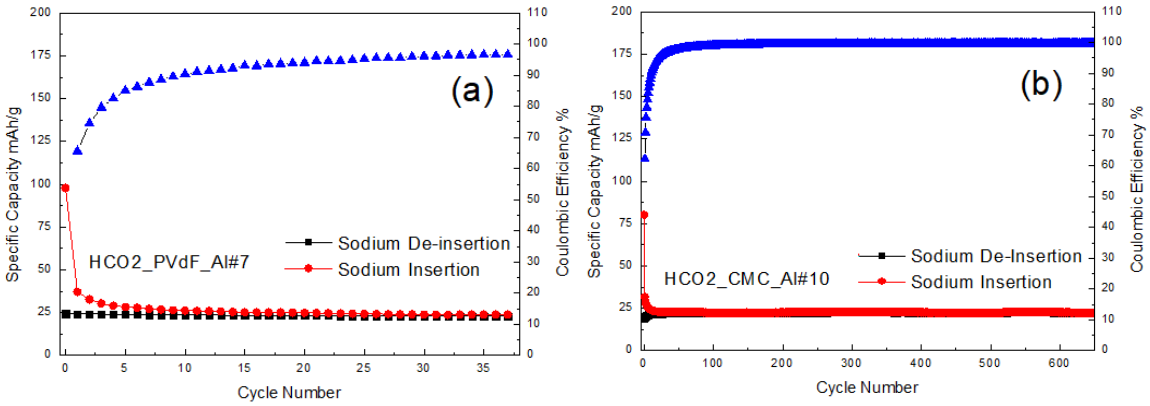

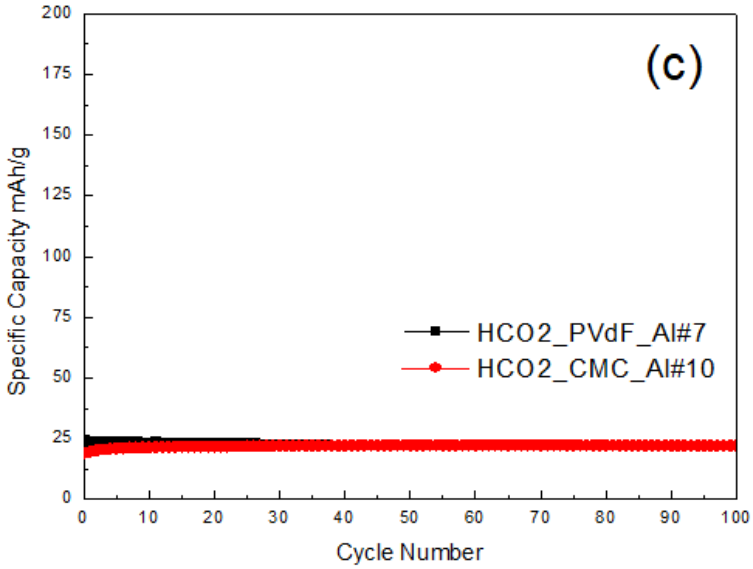

Figure 47a-b-c: HCO2/Na cells;

- **HCO3**
- **Li-Ion Cells**

Sample Name	Total Weight mg	Net Weight mg	Active Material mg	Loading mg/cm^2	Potential Range V
HCO3_PVdF_Cu#10	8.98	3.38	2.70	4.24	0.02<Ewe<3.00
HCO3_CMC_Cu#11	7.35	1.62	1.37	2.15	0.02<Ewe<3.00

As shown in ***Figure 48a-b-c***, HCO3 is one of the most promising HC: the specific capacities and the long-term cyclability are very good. The coulombic efficiencies of both cells are stable and close to 100%. However, the ICs, as well as HCL4, are very high. Also in this case, the CMC electrode exhibit better performances than the PVdF one.

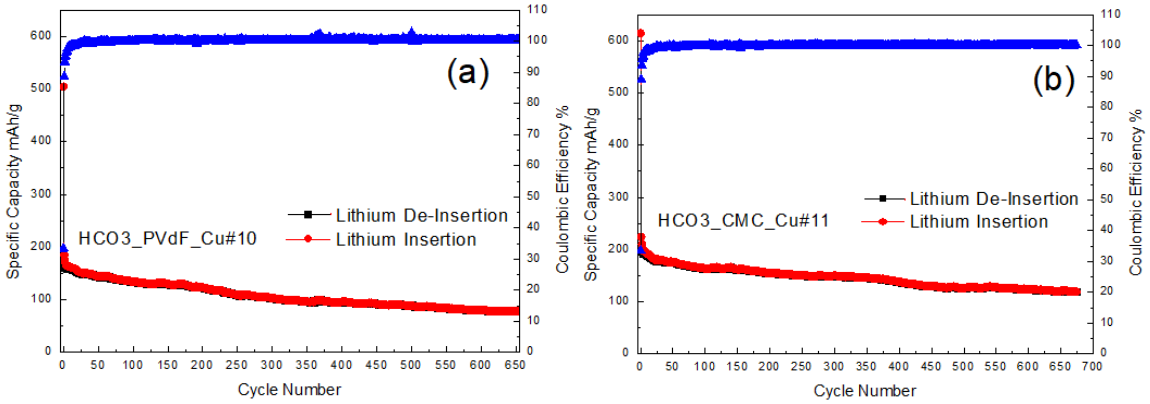

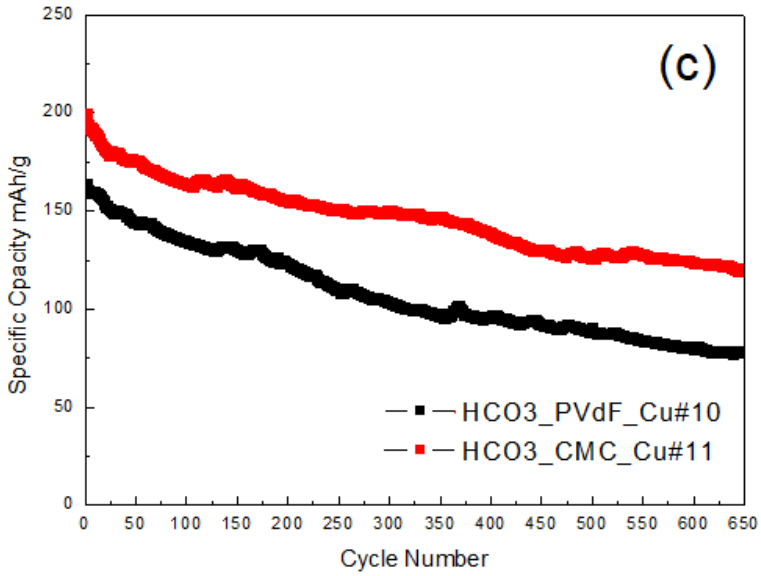

Figure 48a-b-c: HCO3 electrochemical performances in Li-cells;

- **Na-Ion Cells**

Sample Name	Total Weight mg	Net Weight mg	Active Material mg	Loading mg/cm^2	Potential Range V
HCO3_PVdF_Al#10	5.22	1.62	1.29	2.02	0.02<Ewe<3.00
HCO3_CMC_Al#5	7.45	3.85	3.27	5.14	0.02<Ewe<3.00
HCO3_CMC_Al#8	6.71	3.11	2.64	4.15	0.02<Ewe<3.00

HCO3 in sodium cells shows performances comparable to those of HCC (***Figure 49a-b-c-d***): the specific capacities exceed 100 mAh/g for PVdF-based electrode. The cycling stability is good up to 600 cycles as well as coulombic efficiency. Considerable losses of capacities have been found in the first 50 cycles, reflecting a non-completely reversible insertion/de-insertion of sodium that can modify the structure of HC.

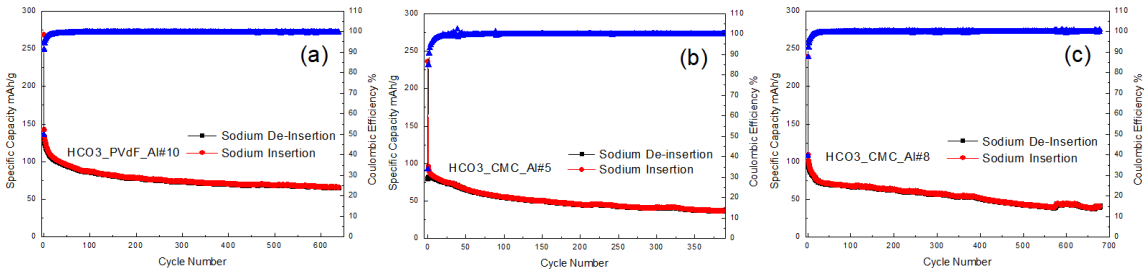

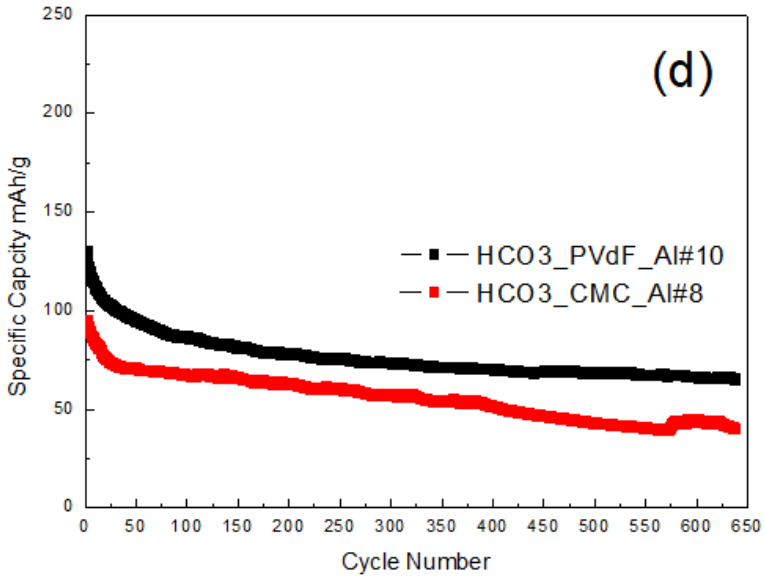

Figure 49a-b-c-d: HCO3/Na cells electrochemical performances and comparison;

- **HCJ1**

- **Li-Ion Cells**

Sample Name	Total Weight mg	Net Weight mg	Active Material mg	Loading mg/cm^2	Potential Range V
HCJ1_PVdF_Cu#1	8.78	3.34	2.83	4.45	0.02<Ewe<3.00
HCJ1_CMC_Cu#5	10.91	5.41	4.59	7.21	0.02<Ewe<3.00

Figure 50a-b-c shows the good performances of HCJ1 with both binders in Li-cells. The irreversible capacities are still high (in the order of 250 mAh/g). About the cycling stability, CMC-based one is quite unstable after 300 cycles and gradually goes down below 100 mAh/g. Considering 130 cyles, PVDF-based one reaches higher specific capacities than CMC-based one.

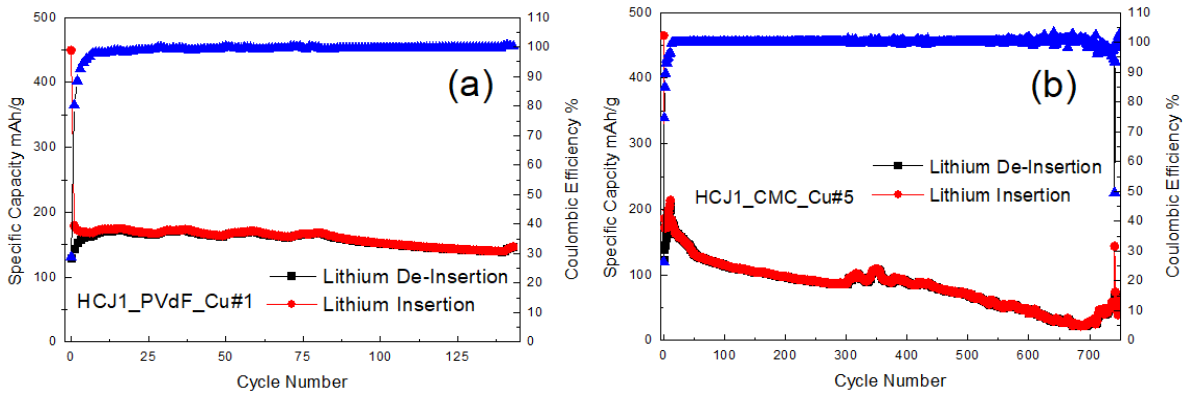

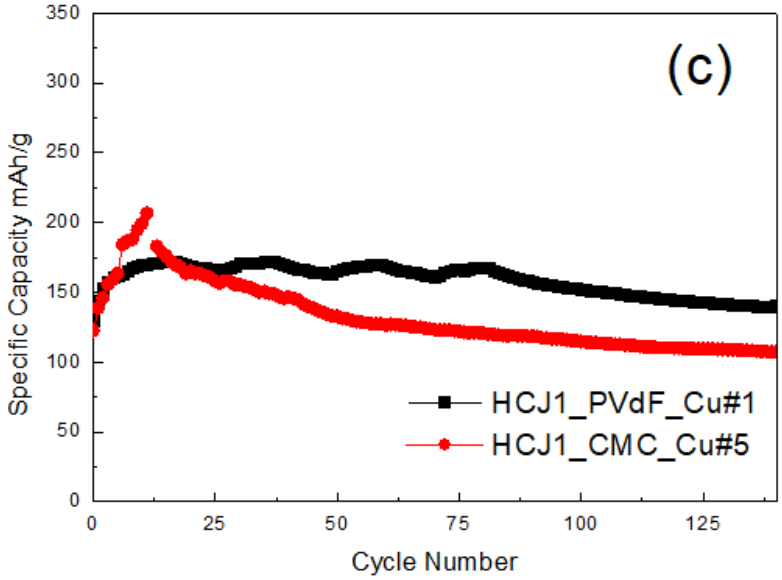

Figure 50a-b-c: Electrochemical performances of HCJ1 vs Li^+;

- **Na-Ion Cells**

Sample Name	Total Weight mg	Net Weight mg	Active Material mg	Loading mg/cm²	Potential Range V
HCJ1_PVdF_Al#5	5.13	1.53	1.22	1.91	0.02<Ewe<3.00
HCJ1_CMC_Al#1	6.53	2.93	2.49	3.91	0.02<Ewe<3.00

In sodium cells (***Figure 51a-b-c***), HCJ1 with PVdF-based electrode shows excellent specific capacity (around 150 mAh/g), reaching the highest values between all the HCs. However, the CMC-based analogue shows lower specific capacity (around 70 mAh/g).

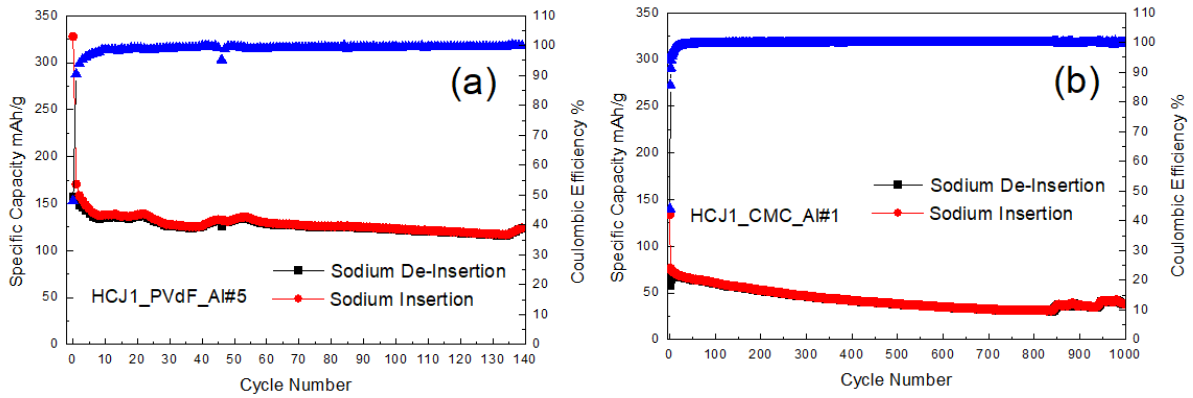

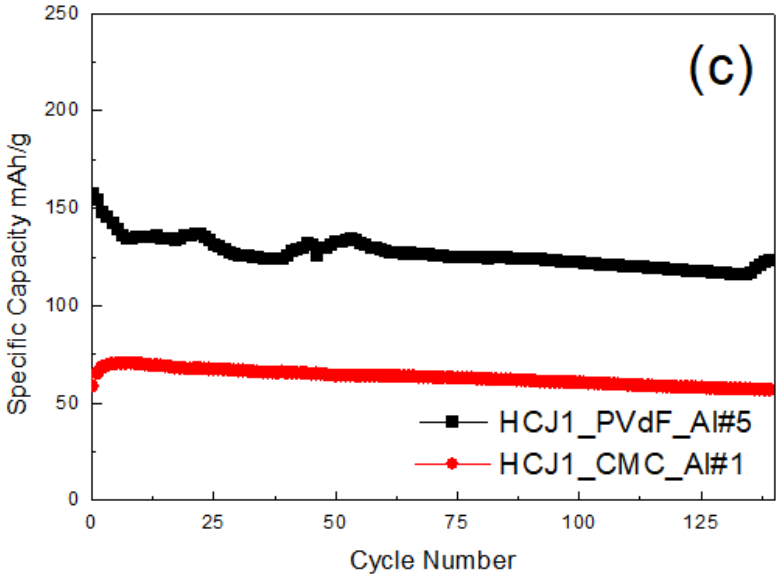

Figure 51a-b-c: HCJ1 electrochemical performances in Na-Ion cells;

- **HCJ2**
  - **Li-Ion Cells**

Sample Name	Total Weight mg	Net Weight mg	Active Material mg	Loading mg/cm^2	Potential Range V
HCJ2_PVdF_Cu#1	9.75	4.17	3.33	5.23	0.02<Ewe<3.00
HCJ2_CMC_Cu#2	8.03	2.45	2.08	1.76	0.02<Ewe<3.00

HCJ2 has appreciable performances, with specific capacity up to 200 mAh/g for CMC-electrode and stable to 150 mAh/g for PVdF-one (***Figure 52a-b-c***).

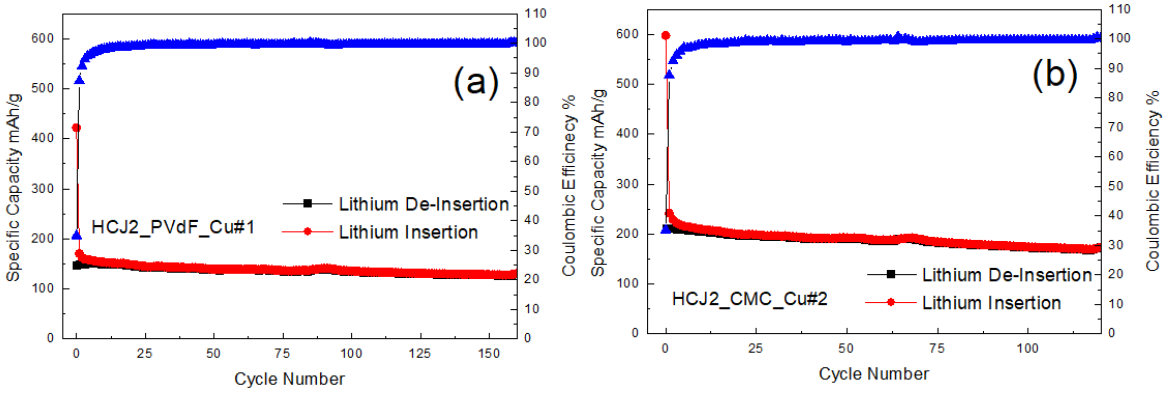

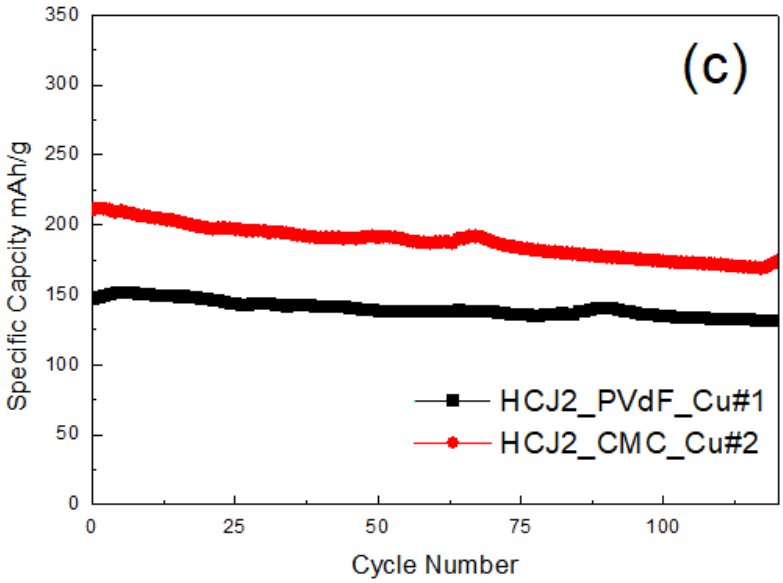

Figure 52a-b-c: HCJ2 performances in Li-Ion cells;

- **Na-Ion Cells**

Sample Name	Total Weight mg	Net Weight mg	Active Material mg	Loading mg/cm^2	Potential Range V
HCJ2_PVdF_Al#1	7.23	3.63	2.88	4.52	0.02<Ewe<3.00
HCJ2_CMC_Al#4	8.94	5.34	4.53	7.12	0.02<Ewe<3.00

On Na-ion cells, HCJ2 exhibit appreciable performances (~70 mAh/g) only with PVdF as binder (***Figure 53a-b-c*****).** However, the cell stops after 120 cycles. By other hand, HCJ2_CMC shows better cycling stability and efficiency but with very low specific capacities.

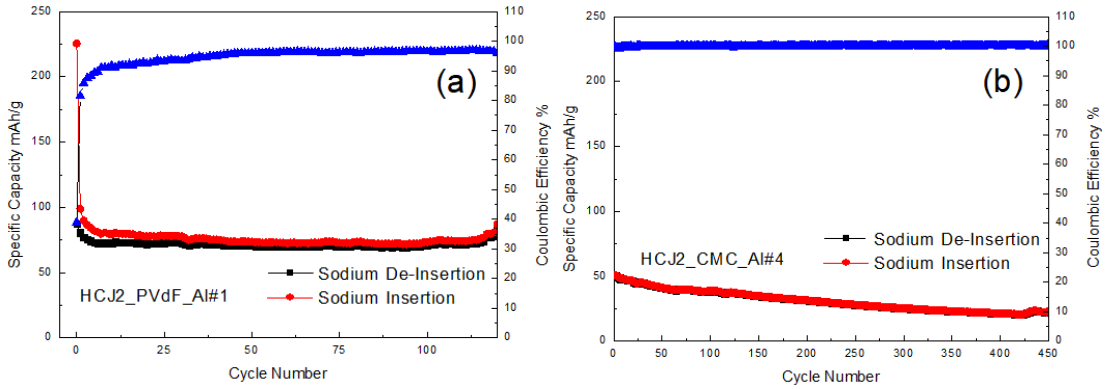

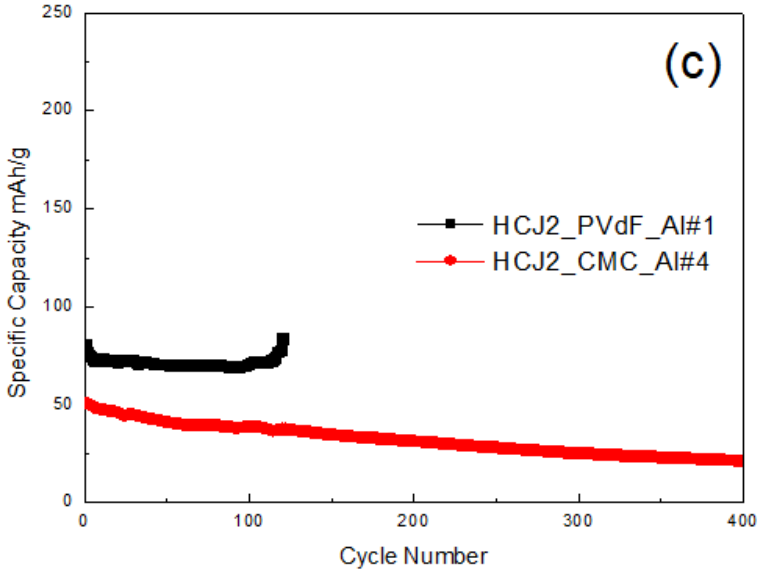

Figure 53: Electrochemical perfromances of HCJ2 vs Na;

- **HCJ3**

- **Li-Ion Cells**

Sample Name	Total Weight mg	Net Weight mg	Active Material mg	Loading mg/cm^2	Potential Range V
HCJ3_PVdF_Cu#1	10.01	4.41	3.52	5.53	0.02<Ewe<3.00
HCJ3_CMC_Cu#1	7.59	2.05	1.74	2.73	0.02<Ewe<3.00

HCJ3 exhibit similar capacities to those of HCJ1 in Li-ion cells and therefore in this case the acid activation doesn't affect the electrochemical performances of the samples. CMC continues to be better than PVdF both in terms of stability and specific capacity (***Figure 54a-b-c***).

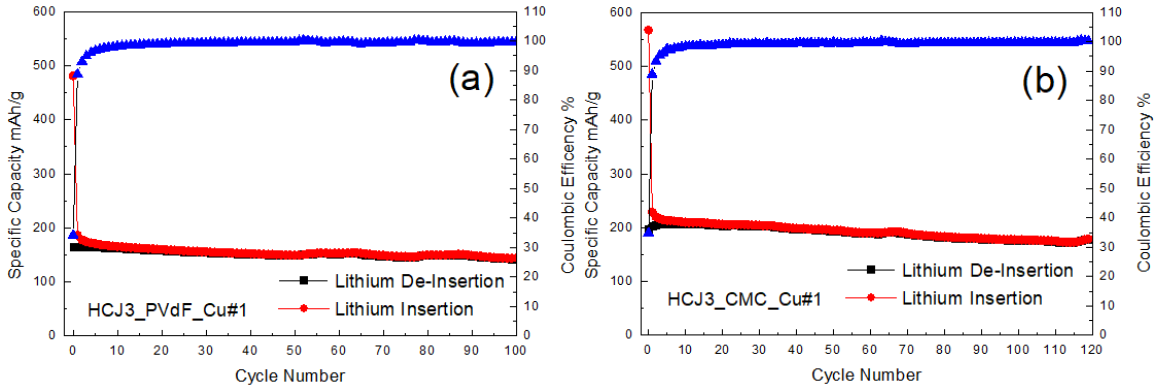

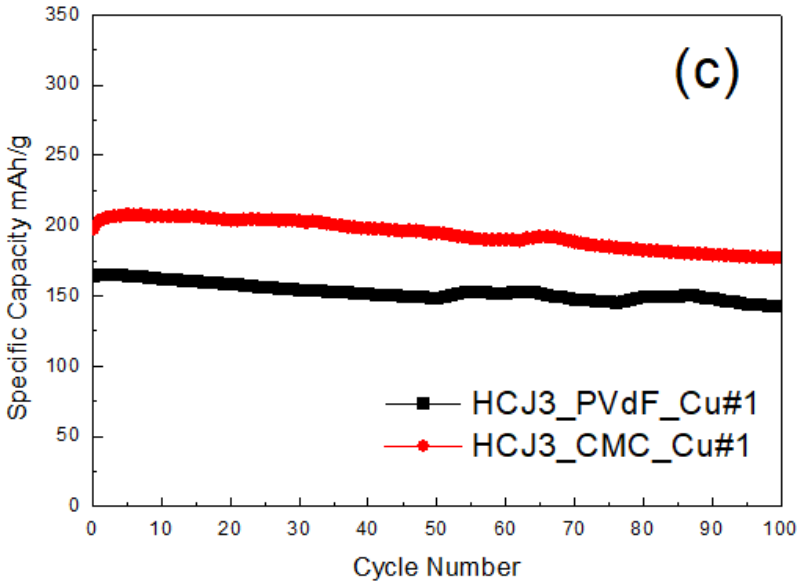

Figure 54: Electrochemical performances of HCJ3 vs Li;

- **Na-Ion Cells**

Sample Name	Total Weight mg	Net Weight mg	Active Material mg	Loading mg/cm^2	Potential Range V
HCJ3_PVdF_Al#7	4.91	1.31	1.04	1.63	0.02<Ewe<3.00
HCJ3_CMC_Al#3	5.81	2.21	1.87	2.94	0.02<Ewe<3.00

Figure 55a-b-c shows the appreciable performances of HCJ3 in sodium cells: the specific capacities are close to 100 mAh/g for 100 cycles. The stability and the coulombic efficiencies are good in both binders.

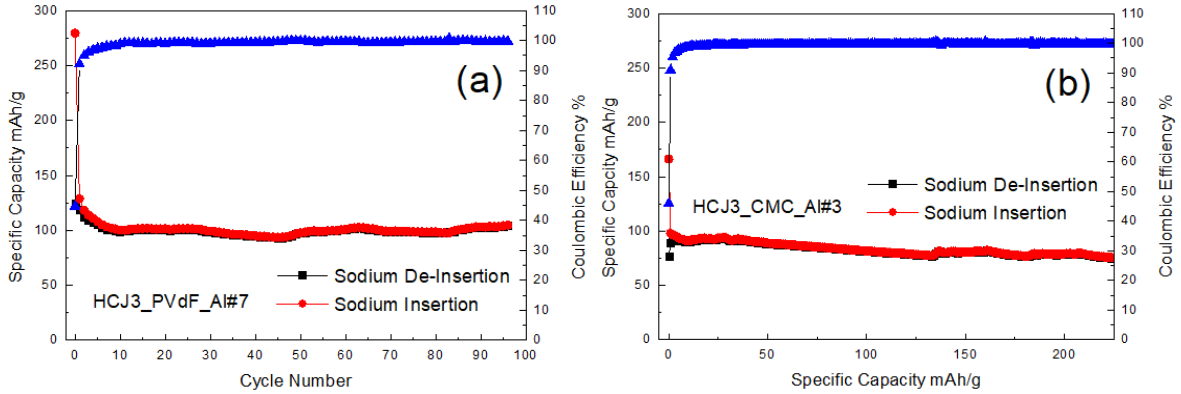

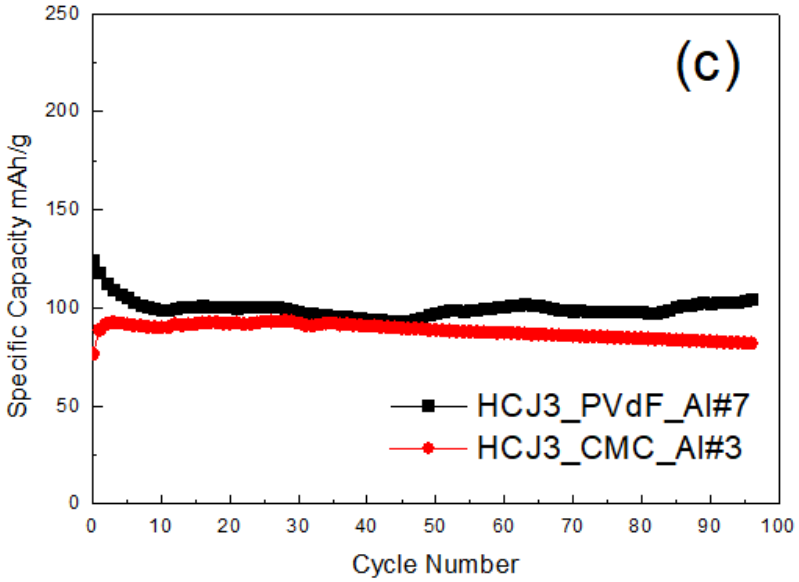

Figure 55a-b-c: Performances of HCJ3 vs Na;

5.2.4 Differential Analysis of Cycles

The first two cycles of each HC in both lithium and sodium cells have been studied by differential analysis in order to characterize the electrochemical processes occurring during cycling.

- **Li-Ion Cells**

In the first cathodic scan (***Figure 56***) of HCs/Li-ion cells, no electrochemical reactions occur until ~1.0V. The plateau between 0.7 and 0.4V indicates the decomposition of the electrolyte and the SEI formation. Further evidences of this plateau association are the lack of the same plateau in other cycles, indicating that the plateau is associated with an irreversible process, and the same position plateau in previous CV scans. HCL4 and HCO2 don't show this plateau markedly, probably confirming the non-completely amorphous phase of these HCs.

Going forward, the sloping region is due to the insertion of Li^+ ions between graphene layers, while the low potential peak (close to 0.1 and 0.2V) can be ascribed with the filling of HC's micropores.

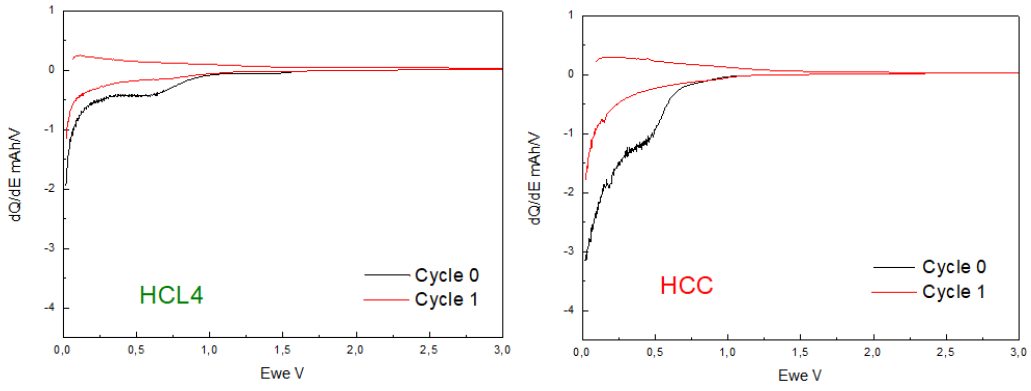

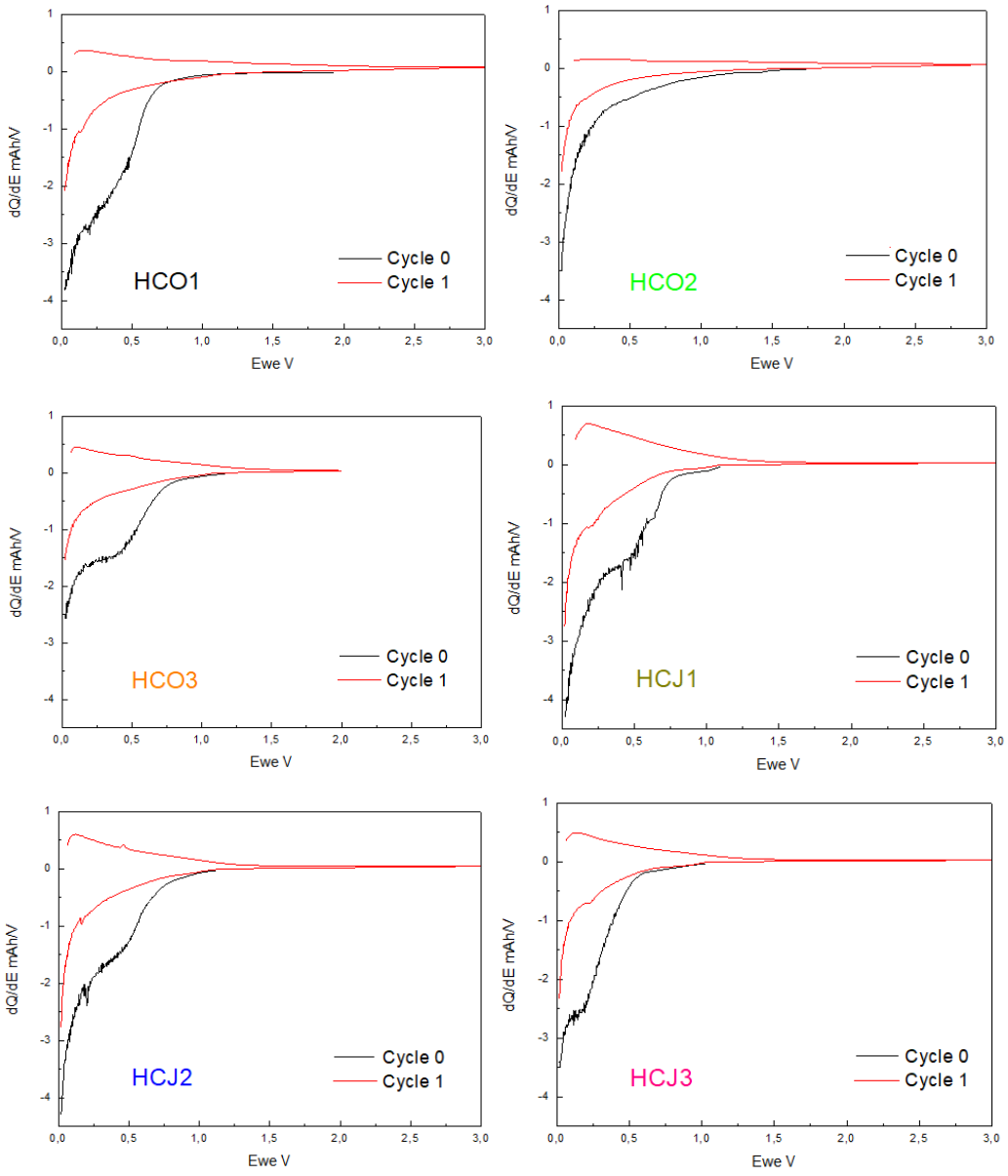

Figure 56: Differential analysis of cycles for each HC in Li-ion cells;

- **Na-Ion Cells**

As in the case of Li-ion cells, formation of the passivation layer occurs at around 0.5V. However, in sodium cells the peak related to SEI formation is still present in subsequent cycles, meaning a low degree of SEI stability. The other two steps of insertion between layers and micropores filling are less visible than Li-ion cells but in any case, they are present (***Figure 57***).

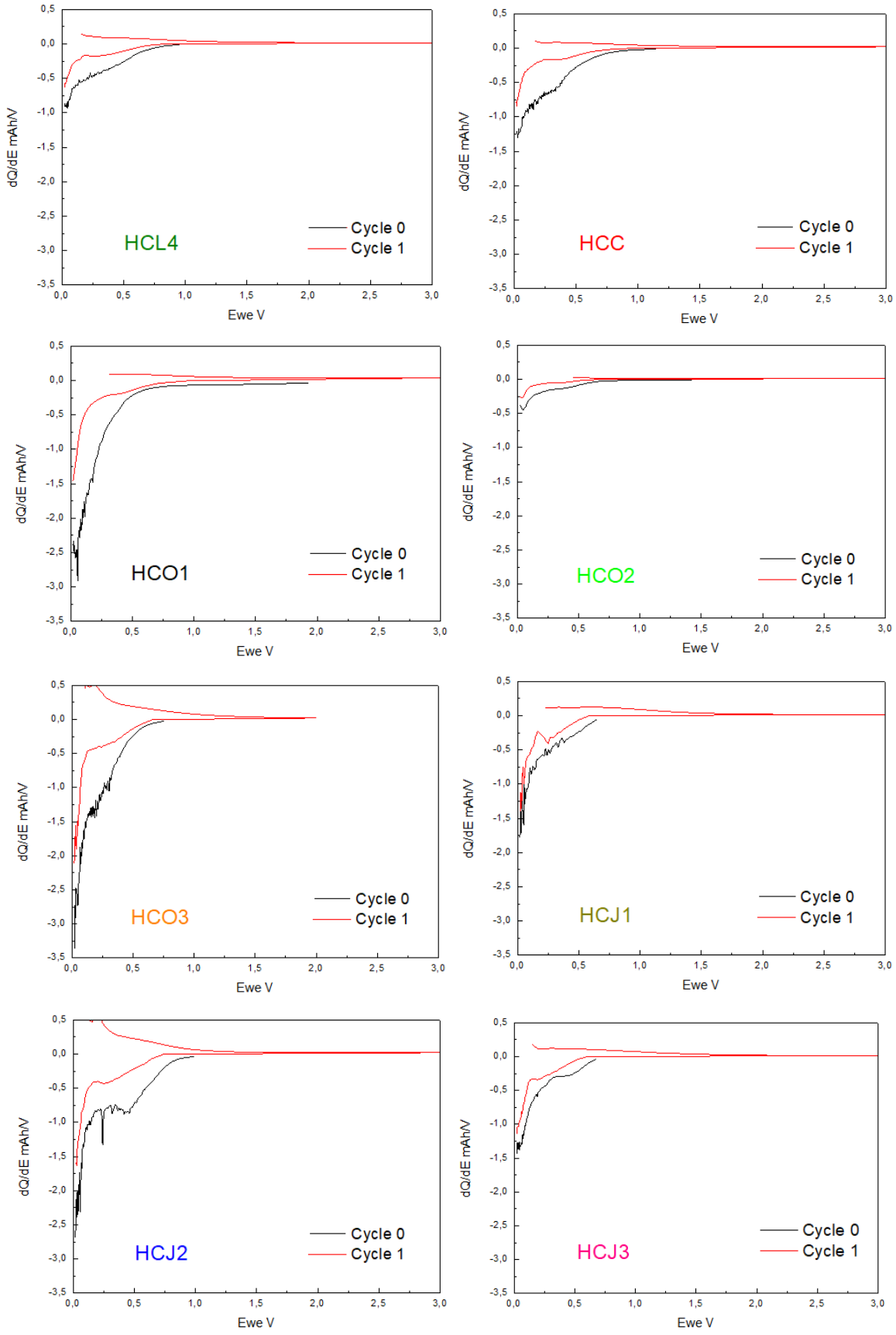

Figure 57: Differential analysis comparison in Na-ion cells;

6.CONCLUSIONS

The specific capacities of all HCs in LIBs are shown in ***Figure 58***. Acid activated olive leaves derived Hard Carbon exhibits the best performances, reaching capacity up to 300 mAh/g for more than 100 cycles. All of olive stones derived Hard Carbons exhibit stable specific capacities around 200 mAh/g for CMC-based electrodes, showing that the different synthesis procedures have not considerable effects on the Hard Carbons' electrochemical performance. However, acid activated orange peels derived Hard Carbon shows better performances (around 180 mAh/g) respect to its analogues with no activation and alkali activation.

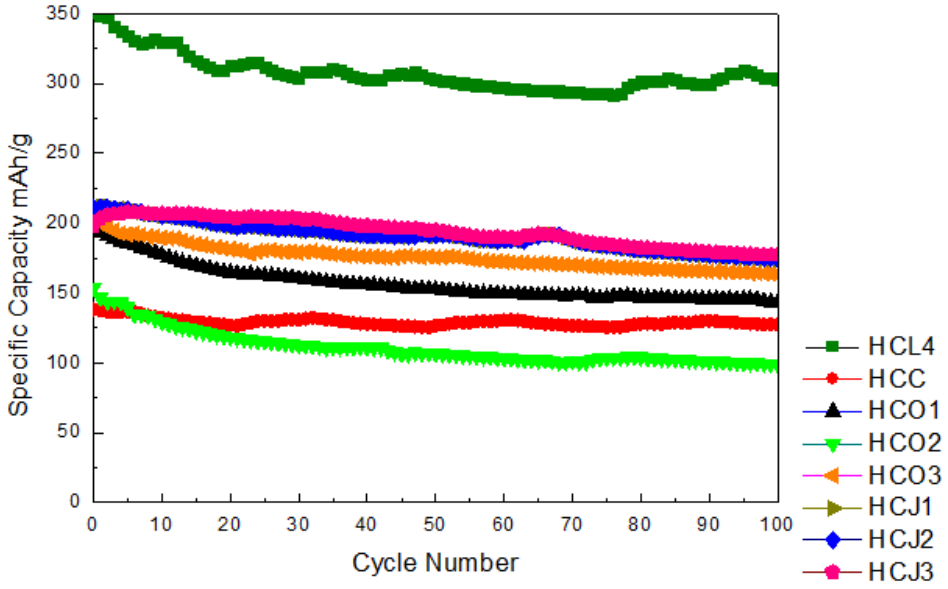

Figure 58: Hard Carbon's specific capacities comparison;

In NIBs (***Figure 59***), no activated olive stones derived Hard Carbon is the most promising anode material (150 mAh/g), although the acid activated one is good as well, maintaining capacities up to 100 mAh/g for more than 100 cycles. The other HCs show specific capacities ranging between 50 and 100 mAh/g except for alkali activated orange peels Hard Carbon, which shows bad performances, probably reflecting its low degree of amorphization. The results obtained in sodium cells confirms the quality of HCl as activating agents, which is able to facilitate the cleavage of bonds between biopolymers (primarily cellulose and lignin) and thus obtain high degree of amorphization.

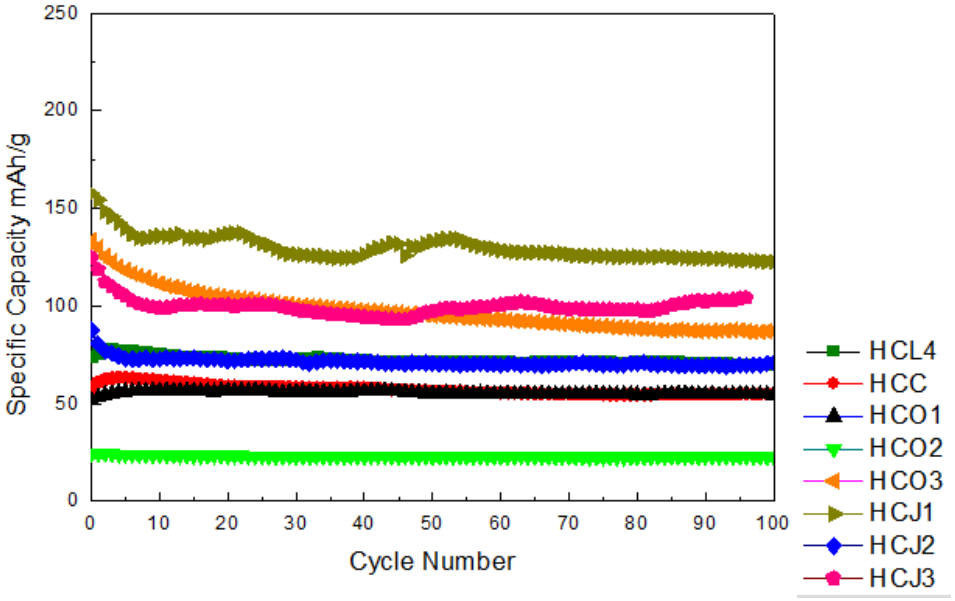

Figure 59: Hard Carbons's specific capacities comparison in NIBs;

Cyclic Voltammetry scans and differential analysis clarify the electrochemical processes involved during cycling: the large irreversible capacity losses can be mostly related to the formation of Solid Electrolyte Interphase, which seems to be more stable in LIBs respect to NIBs. Two additional steps have been recognized: the insertion of Li^+/Na^+ ions between the layers, while the second is related to the adsorption of ions in the micropores.

Although the performances of hard carbons are good, they share a common defect: a significant irreversible capacity. The origin of irreversible capacity is still unclear even if is mostly ascribed to the formation of the Solid Electrolyte Interphase, which is very relevant due to the very large surface area exposed to the electrolyte by the amorphous carbons; nevertheless, the possible entrapment of some ions, and a concentration of surface functional groups that can react with lithium atoms cannot be excluded. This large irreversible capacity for the negative electrode material represents a severe penalty in energy density in batteries for practical applications, especially for NIBs development, since the graphite in LIBs exhibits much lower irreversible capacity. The practical implications arise from the fact that full cells would most likely have to be built with an excess of anode material to avoid sodium deposition and thus safety hazards at low temperature operation or upon overcharge. However, the "cyclable" sodium is provided by the positive electrode. The irreversible capacity translates in loss of such "cyclable" sodium and thus in a lower total battery capacity hence penalizing the maximum achievable energy density.

The preliminary tests used to select the optimal potential range show that the best potential window is $0.02<E_{we}<3.00$, in which hard carbons provide considerable higher specific capacity to the detriment of cycling stability. This can be related to the higher polarization of the electrode that can destroy the passivation layer on the electrode surface. However, the slight loss of cycling stability is irrelevant respect to the gain of specific capacity or, not least, the higher electrochemical window of operation.

The Sodium salt of the Carboxymethyl Cellulose confirms to be a promising alternative to the commercial binder Polyvinyilidene Fluoride: in addition to the numerous advantages in terms of non-toxicity and environmentally friendly, it shows excellent cyclability and in most cases is better than commercial Polyvinyilidene Fluoride.

Chemical activation is a good method to improve the electrochemical performances of HCs, in particular, acid activation is the most promising, especially in sodium battery. However, washing procedure before pyrolysis should be optimized to prevent a huge amount of waste that has to be managed, reducing the eco-sustainability of the synthesis.

Structural and morphological characterizations show that lower times of pyrolysis do not corresponds to lower degrees of amorphization. In addition, the time at the maximum temperature of pyrolysis has no considerable effects on the electrochemical performances of samples. In fact, the performances of olive stones derived Hard Carbons (pyrolyzed at 900°C for 2h) are comparable and in some cases better to those of other Hard Carbons pyrolyzed at 900°C for 6h. Therefore, reducing the pyrolysis time means lower costs of production without reducing electrochemical performances of the final HCs.

Further development may be focused on the optimization of Hard Carbons synthesis, since the structure and therefore the quality of the final HCs are affected by several parameters, such as temperature of pyrolysis, heating rate, chemical activating agents, activation time and impregnation rate of the chemical agents.

In conclusion, biomass-derived Hard Carbons are good candidate as anode materials, especially considering the environmental impact arising from the graphite extraction, which poses a huge problem in regions such as China. In addition, the recent grow in the production of electrified vehicles and the consequent ever-increasing demand of lithium-ion batteries can drive the industries to focus their attention on sustainable electrode materials like Hard Carbons.

7.REFERENCES

[1] V. Marchal, R. Dellink, D. Van Vuuren, C. Clapp, J. Château, E. Lanzi, B. Magné, J. Van Vliet, *OECD Environment Outlook to 2050* (2011);

[2] Z. Gao, Y. Zhang, N. Song, X. Li, *Biomass-derived renewable carbon materials for electrochemical energy storage, Materials Research Letters (2017),* 69-88;

[3] U.S. Energy Information Administration, *International Energy Outlook 2016* (2016);

[4] U.S. Energy Information Administration, *Analysis of the Impacts of the Clean Power Plan* (2015);

[5] R.M. Dell, D.A.J. Rand, *Energy Storage – a key technology for global energy sustainability*, *Journal of Power Sources* (2001), 2-17;

[6] D. Linden, T.B. Reddy, *Handbook of Batteries*, *McGraw-Hill Edition* (1995), 1.3-1.5;

[7] P. Adelhelm, P. Hartmann, C. L. Bender, M. Busche, C. Eufinger, J. Janek, *From lithium to sodium: cell chemistry of room temperature sodium–air and sodium–sulfur batteries*, *Beilstein Journal of Nanotechnology* (2015), 6, 1016-1055;

[8] D. Lin, Y. Liu, Y. Cui, *Reviving the lithium metal anode for high-energy batteries*, *Nature Nanotechnology (2017),* 12*;*

[9] W. Van Schalkwijk, B. Scrosati, *Advances in Lithium-ion Batteries*, *Kluwer Academic/Plenum* (2004);

[10] D. Aurbach, O. Chusid, *Secondary Battery – Lithium Rechargeable Systems – Electrolyte, Additives* (2009), 92-110;

[11] M. Winter, J.O. Besenhard, M.E. Spahr, P. Novàk, *Advanced Materials 10* (1998), 725-763;

[12] W. Ebner, D. Fouchard, L. Xie, *Solid State Ionics* (1994)*,* 69, 238-256;

[13] Tao Zheng, J.R. Dahn, *Synthetic Metals* (1995), 73, 1-7;

[14] Y. Liu, J.S. Xue, T. Zheng, J.R. Dahn., *Carbon* (1996), 34(2), 193-200;

[15] E. Buiel, *Lithium Insertion in Hard Carbon Anode Materials For Li-ion Batteries* (1998);

[16] N. Loeffler, D. Bresser, S. Passerini, *Secondary Lithium-Ion Battery Anodes: From First Commercial Batteries to Recent Research Activities, Johnson Matthey Technology Review* (2015), 59, 34-44;

[17] J.R. Dahn, T. Zheng, Y.H. Liu, J.S. Xue, *Science* (1995)*, 270;*

[18] D. Billaud, E. McRae, A. Horold, *Materials Research Bullettin* (1979), 857;

[19] X.Y. Song, K. Kinoshita, T.D. Tran, *Journal Electrochemical Society* (1996),143;

[20] A. Wang, S. Kadam, H. Li, S. Shi, Y. Qi, *Review on modelling of the anode solid electrolyte interphase (SEI) for lithium-ion batteries, Computational Materials* (2018), 4, 15;

[21] A. Chagnes, J. Swiatowska, *Electrolyte and Solid-Electrolyte Interphase Layer in Lithium-Ion Batteries* (2012);

[22] Y. Ein-Eli, B. Markovsky, D. Aurbach, Y. Carmeli, H. Yamin, S. Luski, *Electrochim. Acta* (1994), 39, 2559;

[23] D. Aurbach, E. Zinigrad, Y. Cohen, H. Teller, *Solid State Ionics* (2002), 148, 405-416;

[24] X. Zhang, P.N. Ross, R. Kostecki, F. Kong, S. Sloop, J.B. Kerr, K. Striebel, E.J. Cairns, F. McLarnor, *Journal Electrochemical Society* (2001), 148, A463;

[25] J.H. Lee, S. Lee, U. Paik, Y.M. Choi, *Journal of Power Sources* (2005), 147, 249-255;

[26] A. M. Skundina, T. L. Kulovaa, A. B. Yaroslavtsevb, *Sodium-Ion Batteries, Russian Journal of Electrochemistry* (2018), 54;
[27] J.W. Choi, D. Aurbach, *Promise and reality of post lithium-ion batteries with high energy densities*, *Nature* (2016), 1, 1-16;
[28] N. Yabuuchi, K. Kubota, M. Dahbi, S. Komaba, *Research development on sodium-ion batteries*, *Chemical Reviews* (2014), 114, 11636-11682;
[29] C. Delmas, C. Fouassier, P. Hagenmuller, *Physic*a B (1980), 99, 81;
[30] N. Yabuuchi, M. Kajiyama, J. Iwatate, H. Nishikawa, S. Hitomi, R. Okuyama, R. Usui, Y. Yamada, S. Komaba, *P2-type $Na_x[Fe_{1/2}Mn_{1/2}]O_2$ made from earth-abundant elements for rechargeable Na batteries*, *Nature Materials* (2012), 11, 512-517;
[31] K. Kubota, S. Komaba, *Review-practical issues and future perspective for Na-ion batteries*, *Journal Electrochemical Society* (2015), 162, A2538-A2550;
[32] V. Palomares, M. Casas-Cabanas, E. Catillo-Martìnez, M.H. Han, T. Rojo, *Update on Na-based battery materials. A growing research path*, *Energy Environmental Science* (2013), 6, 2312-2337;
[33] D. Kundu, E. Talaie, V. Duffort, L. F. Nazar, *The Emerging Chemistry of Sodium Ion Batteries for Electrochemical Energy Storage*, *Angewandte Chemie International Edition* (2015), 54, 3431-3448;
[34] A. Bhide, J. Hofmann, A.K. Durr, J. Janek, P. Adelhelm, *Physical Chemistry Chemical Physics* (2014), 16, 1987 – 1998;
[35] A. Ponrouch, E. Marchante, M. Courty, J.M. Tarascon, M. R. Palacin, *Energy Environmental Science* (2012), 5, 8572 – 8583;
[36] T. Ohzuku, Y. Iwakoshi, K. Sawai, *Journal Electrochemical Society* (1993),140, 2490;
[37] S. Komaba, W. Murata, T. Ishikawa, N. Yabuuchi, T. Ozeki, T. Nakayama, A. Ogata, K. Gotoh, K. Fujiwara, *Electrochemical Na Insertion and Solid Electrolyte Interphase for Hard-Carbon Electrodes and Application to Na-Ion Batteries*, *Advanced Functional Materials (2011)*, 21, 3859-3867;
[38] M.M. Doeff, J. Cabana, M. Shirpour, *Titanate anodes for sodium ion batteries*, *Journal of Inorganic and Organometallic Polymers* (2014), 24, 5-14;
[39] V. Eshkenazi, E. Peled, L. Burstein, D. Golodnitsky, *Solid State Ionics* (2004), 170, 83-91;
[40] G.S. Bumbrah, R.M. Sharma, *Raman spectroscopy - Basic principle, instrumentation and selected applications for the characterization of drugs of abuse*, *Egyptian Journal of Forensic Sciences* (2016), 6, 209-215;
[41] D.A. Skoog, F.J Holler, S.R. Crouch, *Principles of instrumental analysis. 6th ed.* (2006);
[42] R. Marassi, F. Nobili, *Structural and Chemical Properties: Scanning Electron Microscopy*, *Encyclopedia of Electrochemical Power Sources* (2009), 3, 758-768;
[43] N. Elgrishi, K.J. Rountree, B.D. McCarthy, E.S. Rountree, T. T. Eisenhart, J.L. Dempsey, *A Practical Beginner's Guide to Cyclic Voltammetry*, *Journal of Chemical Education* (2018), 95, 197-206;
[44] Princeton Applied Research, *A Review of Techniques for Electrochemical Analysis*;
[45] S.I. Pyun, H.C Shin, J.W. Lee, J.Y. Go, *Electrochemistry of Insertion Materials for Hydrogen and Lithium, Springer* (2012), 2;

[46] M. Molina-Sabio, F. Rodrìguez-Reinoso, *Role of chemical activation in the development of carbon porosity*, *Colloids and Surfaces A* (2004), 241, 15-25;
[47] M. Olivares-Marìn, C. Fernàndez-Gonzàlez, A. Macìas-Garcìa, V. Gòmez-Serrano, *Preparation of activated carbon from cherry stones by chemical activation with $ZnCl_2$*, *Applied Surface Science* (2006), 252, 5967-5971;
[48] H. Hofbauer, M. Kaltschmitt, T. Nussbaumer, *Energie aus Biomasse –Grundlagen, Techniken, Verfahren* (2009), 375-406;
[49] A. Downie, A. Crosky, P. Munroe, *Physical properties of biochar*, *Biochar for environmental management - science and technology* (2009), 13-32;
[50] M.G. Groenli, G. Varhegyi, C. Di Blasi, *Thermogravimetric analysis and devolatilization kinetics of wood*, *Industrial and Engineering Chemical Research* (2002), 41, 4201-4208;
[51] J.F. Gonzàlez, J.M. Encinar, J.L. Canito, E. Sabio, M. Chacòn, *Pyrolysis of cherry stones: energy uses of the different fractions and kinetic study*, *Journal of Analytical and Applied Pyrolysis* (2003), 67, 165-190;
[52] J. Ajuria, E. Redondo, M. Arnaiz, R. Mysyk, T. Rojo, E. Goikolea, *Lithium and sodium ion capacitors with high energy and power densities on carbons from recycled olive pits*, *Journal of Power Sources* (2017), 359, 17-26;
[53] A.C. Ferrari, J. Robertson, *Interpretation of Raman spectra of disordered and amorphous carbon*, *Physical Review B* (2000), 61;
[54] C. Portet, G. Yushin, Y. Gogotsi, *Electrochemical performance of carbon onions, nanodiamonds, carbon black and multiwalled nanotubes in electrical double layer capacitors*, *Carbon* (2007), 45, 2511-2518
[55] K. Hong, L. Qie, R. Zeng, Z. Yi, W. Zhang, D. Wang, W. Yin, Chao Wu, Q. Fan, W. Zhang, Y. Huang, *Biomass derived hard carbon used as a high-performance anode material for sodium ion batteries*, *Journal of Materials Chemistry* (2014), A2, 12733;
[56] D.A. Stevens, J. R. Dahn, *Journal of Electrochemical Society* (2001), 148, A803;
[57] K. Gotoh, T. Ishikawa, S. Shimadzu, N. Yabuuchi, S. Komaba, K. Takeda, A. Goto, K. Deguchi, S. Ohki, K. Hashi, T. Shimizu, H. Ishida, *Journal of Power Sources* (2013), 225, 137;
[58] M. Winter, J.O. Besenhard, *Handbook of Battery Materials* (2011), 15;
[59] E. Irisarri, A. Ponrouch, M.R. Palacin, *Review—Hard Carbon Negative Electrode Materials for Sodium-Ion Batteries*, *Journal of The Electrochemical Society* (2015), 114A, 2476-2482;